JOY OF CEX: SHARPENING THE (t,^{3}He) PROBE AT 345 MeV FOR THE CHARGE-EXCHANGE KNIFE DRAWER

DISSERTATION

Presented in Partial Fulfillment of the Requirements for

the Degree Doctor of Philosophy in the

Graduate School of The Ohio State University

By

Meredith E. Howard, B.S., M.S.

* * * * *

The Ohio State University

2008

Dissertation Committee:

Dr. Evan R. Sugarbaker, Adviser

Dr. Thomas Humanic

Dr. Terrence Walker

Dr. Linn Van Woerkom

Approved by

Adviser

Graduate Program in Physics

ABSTRACT

This data set represents the first step in a campaign of (t,^{3}He) charge-exchange experiments at the National Superconducting Cyclotron Laboratory designed explicitly to measure Gamow-Teller strength distributions in the electron capture direction for stable medium-heavy atomic nuclei, with particular interest in reaching the nuclei in the pf-shell or masses up to A=112. The 115 MeV/nucleon secondary triton beam with an average intensity of 4×10^6 pps on 10 mg/cm^2 thick target foils produces ^{3}He that are measured in the focal plane detectors of the S800 magnetic spectrometer. From these data, the scattering angle of the tritons is reconstructed to within 7 mrad and the energy of the recoil nucleus is reconstructed to better then 250 keV. Since there is no comprehensive study of the (t,^{3}He) probe for triton energies of 100-400 MeV/nucleon, this data is the first step in evaluating the advantages of extracting B(GT) from the (t,^{3}He) probe over other hadronic probes.

The first target is a CD_2 target used for calibrating cross section. This is the third measurement for the (t,^{3}He) probe on ^{12}C above 100 MeV/nucleon. The present ^{12}C(t,^{3}He) cross section for the ^{12}B ground state ($J^\pi = 1^+$) is lower than a previous measurement at the NSCL by more than one standard deviation in uncertainty but agrees with ^{12}C(^{3}He,t)^{12}N.

This (t,^{3}He) measurement for ^{24}Mg, the second target, is the first above 100 MeV/nucleon. The B(GT) distribution for ^{24}Na is extracted from differential cross sections as a function of residual nucleus excitation energy up to 7 MeV. For each peak in excitation energy, the differential cross section as a function of reconstructed scattering angle is extrapolated to zero degrees using angular distrubutions calculated with the distorted wave calculations from the code FOLD and transformed to $q = 0$ zero momentum transfer. Uncertainties in the B(GT) include a calculation of interference to $J^\pi=1^+$ expected from ΔL=2, ΔS=1 reactions.

Comparisons of B(GT) distributions of ^{24}Na with that of modern calculations using an improved interaction for the *sd*-shell space are discussed. In particular, a recently improved hamiltonian for the *sd*-shell model space is compared with the quarter-century-old USD interaction. The experimental measurements, both the present data and those of the competing charge-exchange probe (d,^{2}He), are in good agreement with theoretical calculations.

As a result of this work, the NSCL has dramatically improved the availability of the secondary triton beam and the resolution for charge-exchange experiments and completed experiments for (t,^{3}He) on several nuclei above $A = 45$.

To Barbara, who loves physicists saying her name.

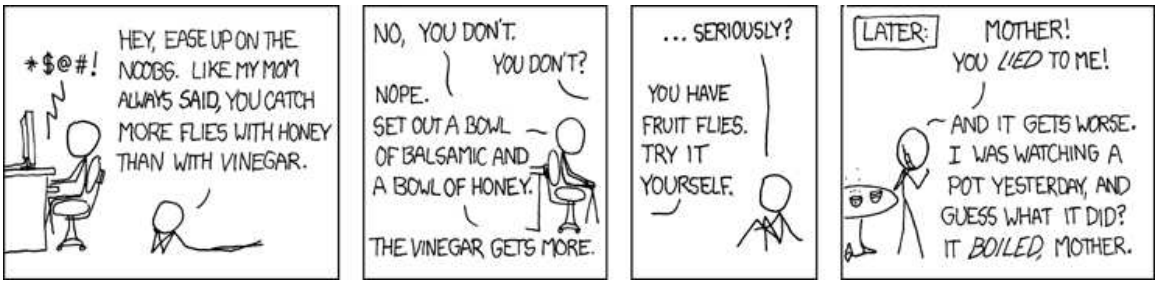

Figure 0.1: Flies: www.xkcd.com/357/ by Randall Munroe, with permission under a Creative Commons Attribution-NonCommercial 2.5 License [61].

ACKNOWLEDGMENTS

This work and the rest of my graduate school career is the product of my interaction with so many people in so many capacities, that the only logical plan of attack is to address people geographically in turn, starting north in East Lansing, MI and heading south to Columbus, OH and then on towards New Orleans.

I have enjoyed hospitality and collaboration with the fine members of the National Superconducting Cyclotron Laboratory in East Lansing, Michigan. The many enthusiastic faces made my many stays in Michigan an adventure and a welcoming environment. I thank the Charge Exchange group for their help and support. In particular, S. Austin, D. Bazin, D. Galaviz, G. W. Hitt, A. Stolz and R.G.T. Zegers made this work both possible and fun. Getting a high intensity triton beam is no trivial feat. The staff at the Coupled Cyclotron Facility worked hard to work through issues with the beam we required, and they met bewildering challenges with grace, elbow grease, humor and highly entertaining frustration.

This work involved lots of travel over several years, especially countless mileage on US-23 between the Michigan and Ohio capitals. Mary Smith (OSU- retired) and Raman Anantraraman (NSCL) were quite valuable and always friendly in handling the many administrative issues.

Of course there are many people to thank at the Department of Physics at The Ohio State University. The professionalism, courtesy and unintrusive hard work of the

guys and gals in the Computer Department has been a luxury every physicist should know. Whatever the platform, whatever the software need, whatever the hardware issue, they always reponded without complaint, sometimes in the middle of the night, "we will do our best to get you what you need." When an immediate solution either wasn't available, the staff was always mindful of providing alternatives to tide their users over until the fix is in. I can't say enough. How fitting that my first pleasant interaction on moving to Columbus, Ohio was J.D. Wear telling me where to find the good food and the good coffee. Cheers. Within the Dick Boyd OSU nucastro group, Arthur L. Cole, Edward E. Smith, Michael Famiano, Alex St.J. Murphy, and the elusive Juergen Zach were my early day-to-day Ohio group mates. During my adviser's time with the NSF, Arthur and Ed played special roles as commiserates, friends, and allies, especially at the NSCL. I appreciate your time, patience, humor and help, guys.

Between OSU and the NSCL, my official and unofficial bosses have been Richard N. Boyd, Remco G. T. Zegers, and Evan Sugarbaker. Before jumping ship for a 4 year stint at the National Science Foundation as a project manager, Dick was friendly, approachable and ever happy to share the advice he'd wished someone had shared with him. Remco was the day-to-day supervisor for my experiment and core research. I was fortunate enough to be quickly folded into his group when he was hired at the NSCL and be part of every stage of this project. In particular, the central benefit of working with a new assistant professor has been the unfettered access to him for discussion and help (including help with the minutia and small details) and the enthusiasm for getting his hands dirty. I appreciate his time above all, which has been important for working on an experiment where my access to the S800 detectors and

DAQ has been so limited. I am only sorry that East Lansing isn't closer to Columbus. Finally, Evan Sugarbaker, has served as a fill-in for the now academically retired Dick Boyd. Evan is a very busy man, especially as he was taking on the construction of the new physics building at OSU. Even so, he has always made time for Ed Smith and for me. His friendly demeanor, genuine concern and the experience he shared were a comfort. Thank you. Many of these above people will fade in my mind to pleasant memories, and I am glad to have had them at all.

Reaching deep south, I would like to acknowledge my family, all now transplanted to Houston, Texas. For superlatives, I have to reach for biggest (in number, size, and ego) and for most entertaining. My mother Barbara gave me my balls, my father Don gave me my ego, and my siblings IBS. Their love and support has been bizarre, comforting, distressing, and a reason to rack up frequent flier miles. I am looking forward to boosting four little guys, Hasan, Josiah, Paolo and Alim, higher up in the rotation.

Finally, this work was supported financially by the National Science Foundation under grants PHY0140255, PHY0216783 (JINA), PHY0606007, and PHY0758099.

VITA

Julian Day 2442819	Born - New Orleans, Louisiana, USA
1999	B.S. Physics, Louisiana State University A & M
2003	M.S. Physics, The Ohio State University
1999-2002	William Fowler Fellow
2002-present	Graduate Teaching and Research Associate, The Ohio State University.

PUBLICATIONS

Research Publications

N. Özkan, A. StJ. Murphy, R.N. Boyd, A.L. Cole, R. deHaan, M. Famiano, J. Görres, R.T. Güray, M. Howard, L. Şahin, M.C. Wiescher. "Proton radiative capture cross sections on ^{102}Pd at energies of astrophysical interest." *Nuclear Physics A*, **688** (2001) 459c-461c.

N. Özkan, A. St.J Murphy, R.N. Boyd, A.L. Cole, M. Famiano, R.T. Güray, M. Howard, L. Şahin, J.J. Zach, R. deHaan, J. Görres, M. C. Wiescher, M.S. Islam and T. Rauscher. "Cross section measurements of the ^{102}Pd(p,γ), ^{103}Ag^{116}Sn(p,γ)^{117}Sb, and ^{112}Sn(α,γ)^{116}Te reactions relevant to the astrophysical *rp*- and γ-processes." *Nuclear Physics A*, **710** (2002) 469-485.

A. Gade, D. Bazin, A. Becerril, C. M. Campbell, J. M. Cook, D. J. Dean, D.-C. Dinca, T. Glasmacher, G. W. Hitt, M. E. Howard, W. F. Mueller, H. Olliver, J. R. Terry, and K. Yoneda. "Quadrapole deformation of the self-conjugate nucleus ^{72}Kr." *Physical Review Letters* **95**, 022502 (2005).

R.G.T. Zegers, A.L. Cole, H. Akimune, S.M. Austin, D. Bazin, A.M. van den Berg, G.P.A. Berg, J. Brown, I. Daito, Y, Fujita, M. Fujiwara, K. Hara, M.N. Harakeh, G.W. Hitt, M.E. Howard, J. Jänecke, T. Kawabata, T. Nakamura, H. Ueno, H. Schatz, B.M. Sherrill, M. Steiner. "Weak interaction strengths for supernovae calculations via the (t,^{3}He) reaction on medium-heavy nuclei." *Nuclear Physics A* **758** (2005) 67c-70c.

R.G.T. Zegers, H. Akimune, S.M. Austin, D. Bazin, A.M. van den Berg, G.P.A. Berg, B.A. Brown, J. Brown, A.L. Cole, I. Daito, Y. Fujita, M. Fujiwara, S. Galès, M.N. Harakeh, H. Hashimoto, R. Hayami, G.W. Hitt, M.E. Howard, M. Itoh, J. Jänecke, T. Kawabata, K. Kawase, M. Kinoshita, T. Nakamura, K. Nakanishi, S. Nakayama, S. Okamura, W.A. Richter, D.A. Roberts, B.M. Sherrill, Y. Shimbara, M. Steiner, M. Uchida, H. Ueno, T. Yamagata, and M. Yosoi. "The (t,^{3}He) and (^{3}He,t) reactions as probes of Gamow-Teller strength." *Physical Review C* **74**, 024309 (2006).

G.W. Hitt, Sam. M. Austin, D. Bazin, A.L. Cole, J. Dietrich, A. Gade, M.E. Howard, S.D. Reitzner, B.M. Sherrill, C. Simenel, E.E. Smith, J. Stetson, A. Stolz, R.G.T. Zegers. "Development of a secondary triton beam from primary ^{16,18}O beams for (t,^{3}He) experiments at intermediate energies." *Nuclear Instruments and Methods in Physics Research A* Vol. 56 (2006) 264-269.

R.G.T. Zegers, T. Adachi, H. Akimune, S.M. Austin, A.M. van den Berg, B.A. Brown, Y. Fujita, M. Fujiwara, S. Galès, C.J. Guess, M.N. Harakeh, H. Hashimoto, K. Hatanaka, R. Hayami, G.W. Hitt, M.E. Howard, M. Itoh, T. Kawabata, K. Kawase, M. Kinoshita, M. Matsubara, K. Nakanishi, S. Nakayama, S. Okumura, T. Ohta, Y. Sakemi, Y. Shimbara, Y. Shimizu, C. Scholl, C. Simenel, Y. Tameshige, A. Tamii, M. Uchida, T. Yamagata, and M. Yosoi. "On the extraction of weak transition strength via the (^{3}He,t) reaction at 420 MeV." *Physical Review Letters* **99**, 202501 (2007).

R.G.T. Zegers, R. Merharchand, T. Adachi, S.M. Austin, B.A. Brown, Y. Fujita, M. Fujiwara, C.J. Guess, H. Hashimoto, K. Hatanaka, M.E. Howard, M. Matsubara, K. Nakanishi, T. Ohta, Y. Sakemi, Y. Shimbara, Y. Shimizu, C. Scholl, A. Signoracci, Y. Tameshige, A. Tamii, and M. Yosoi. "Spectroscopy of ^{24}Al and extraction of Gamow-Teller strengths with the ^{24}Mg(^{3}He,t) reaction at 420 MeV." *Physical Review C* **78**, 014314 (2008).

FIELDS OF STUDY

Major Field: Physics

TABLE OF CONTENTS

Page

LIST OF TABLES

Table **Page**

LIST OF FIGURES

Figure **Page**

CHAPTER 1

INTRODUCTION

> One of the main nuclear features which led to the development of the shell structure is the existence of what are usually called the magic numbers. That such numbers exist was first remarked by Elsasser in 1933 [30].... When Teller and I worked on a paper on the origin of the elements, I stumbled over the magic number. We found that there were a few nuclei which have a greater isotopic, as well as cosmic, abundance than our theory, or any other reasonable continuum theory, could possibly explain. Then I found that those nuclei had something in common: they either had 82 neutrons, whatever the associated proton number, or 50 neutrons. Eighty-two and fifty are magic numbers. That nuclei of this type are unusually abundant indicates that the excess stability must have played a part in the process of the creation of the elements. [41]
> -Maria Goeppert-Mayer

Clues to the structure of atomic nuclei are often found in astrophysics. The correlation between astrophysical phenomena and nuclear structure are so close that in 1953 astrophysicist Sir Fred Hoyle predicted a previously unknown excited state in ^{12}C [27] based on two simple assumptions- that the anticipated helium burning stage in stars would proceed as a rapid fusing of three helium nuclei, and that the production of carbon (in stars) is predicated on the success of this so called triple-α process.

Starting at the turn of the century, calculations of the structure in medium-heavy nuclei are getting a closer examination by both the theoretical and experimental

communities in nuclear physics. The present work serves to broaden the experimental tools available for testing the theoretical advances.

1.1 Introduction

The second most important question addressed by nuclear physics is that of the origin of the isotopic abundances in our solar system and in our galaxy. Untangling the many competing processes in the many astrophysical environments that manufacture these isotopes and describing each process with enough accuracy to reproduce known observables are complicated and open tasks that cross many fields in physics. Supernovae (SNe), astronomical explosions at the retirement stage of the stellar life cycle, are the proposed hosts to several such processes in this problem. For type II and type Ia Supernova models, one of the most solveable sources of uncertainty is that of weak reaction rates both before and during the supernova explosion.

The present work is the first in a series of steps to reduce the uncertainties in weak-reaction rate tabulations for supernova models, by providing experimental data against which the some-what newly improved theoretical calculations can be tested. Chapter 1 describes the motivation from astrophysics for understanding weak nuclear reactions, problems in astrophysical modelling and projects the payoff for measuring charge-exchange reactions in nuclei.

1.2 Supernovae: Observations and Models

Though there are records of naked-eye observation of supernovae going back centuries, detailed data on supernovae are both relatively new and incomplete. As of 2006, there are no observations of gravity waves. (Terrestrial gravity wave detectors

at the time of SN1987a were all off in coordinated maintenance, and so missed the best chance to date of observing gravity waves.) Supernova neutrino data, though well studied, is scarce and will remain so until the next local supernova[1]. On the other hand, optical data is much richer by comparison, so much so that type I SNe are standard candles in astronomy and solid players in the Hubble-expansion puzzle. With so much data on the light emitted from supernovae at various times in the supernova explosion, for example, study of the dust ejected around supernovae is an active and fruitful field. Even supernova ejecta dust grains settled on Earth's surface are studied in the geological archives of ice cores and ocean sediment [29, 67]. (these geological archives, however, are severely limited and difficult to interpret.)

Even with these blind spots, there is little controversy or dissent in the broad-brush standard picture of the causes and general timeline in the dynamics of supernovae. At the onset of core-collapse SNe in massive mature stars, what is called the electron degeneracy pressure gives way to the gravitational burden of the outer layers. This rare occurence of the weak force being taken over by the (even weaker) gravitational force sets off a chain of electron captures onto the Fe group nuclei[2] in the core. Electrons convert to relatively inert neutrinos, nuclear abundances change, and the outer layers of the star go into free fall until the strong force halts the infalling matter to send it back out in a spectacular "bounce."

This outgoing shockfront stalls in computer models described in the literature, and there is some open debate as to how the shock front is restarted. General theories as to how the stalled shock front restarts can be loosely divided into two cliques. The

[1]Supernovae in this Galaxy or any of the Milky Way's parasite galaxies, such as the Large Magellanic Cloud, are consider "local."

[2]The silicon burning ashes, which include Fe, Ti, V, Cr, Mn, Co and Ni, are generally (and confusingly) catagorized as "iron group nuclei." The core is not, in fact, all iron.

longer held and more popular theory is the neutrino-heating mechanism, whereby the stalled explosion is jump-started by energy transferred to the infalling matter through neutrino interactions. This scenario is a complicated dance heavily reliant on convection, instabilities and careful timing to achieve efficient heating of the infalling matter. Furthermore, this scenario will only be successful if the explosion can be restarted in a few hundred milliseconds, lest the massive star be condemned to total collapse without a supernova explosion. For this reason, the timing for supernova simulations is on the order of several hundred milliseconds. One recent and perhaps more interesting theory is the so-called acoustic mechanism [18]. Burrows et al proposed in 2005 that the energy lost in the stalling is stored in mechanical sound waves, which rock in and out unstably, until finally breaking free approximately 600 ms after the shock front stalls. The simulations of Burrows et al. are 2-D dimensional calculations made with the supernova code VULCAN/2D. This group boldly predicts that the breaking of spherical symmetry will be held up in the future as a crucial key to understanding and to modelling supernovae. If true, this specific prediction foretells a discontinuous advancement in SN computer models once computational constraints are loosened[3].

This second scenario is not necessarily a competitor to the neutrino-heating mechanism, but perhaps a fail-safe, making core collpase supernovae more robust against varying initial conditions. Indeed, that current supernova models are so difficult to explode despite the ease with which Nature ignites them is a curious point. (There is still speculation as to whether failed supernova explosions are as common as the successful.)

[3]To date, almost all computer simulations require spherical symmetry to greatly simplify the calculation. Clearly, this geometry does not conserve energy or momentum since the center of mass is externally *forced* to remain at the origin.

Excellent reviews of the standard model of supernovae, the nuclear physics needed for supernovae and recent progress can be found in Refs. [57], [9]and [85].

Section 1.3 describes the role of electron capture in both the white dwarf type Ia SNe and the core collapse type II SNe.

1.3 Role of Electron Captures in Supernovae

Type Ia supernovae[4] are thermonuclear explosions of a white dwarf in a binary system, accreting hydrogen or helium from the companion star. Such explosions are thought to contribute at least 55% of the Fe group nuclei in the Milky Way Galaxy and do not leave remnant bodies such as neutron stars or black holes [54]. The electron degeneracy pressure in the inner layers of accreting, contracting white dwarfs is independent of temperature. During contraction, as the white dwarf's size approaches the Chandrasekhar mass, carbon fusion ignites. Without expansion, the fusion runs away and the burning front propagates through the whole star unabated, ultimately ejecting the entire mass of the star into the interstellar medium. The isotopic abundances of this ejected matter depends chiefly on the proton -to -nucleon ratio Y_e. In particular, uncertainties in the astrophysical modelling (e.g. central ignition densities and shock wave speeds) can only be clarified with significantly improved nuclear physics input [80].

Type II supernovae are explosions following the core collapse of massive stars [10]. Electron capture on medium-heavy and heavy nuclei in the dense, collapsing core are important both at early onset and in later phases during neutronization. The weak

[4]The classification scheme for supernovae is based on astronomical observations and not directly on the supernova explosion mechanism or the supernova progenitor. Type I SNe have no hydrogen spectral lines, whereas type II have strong hydrogen lines. The *a* in Ia SNe denotes the presence of a certain Si II spectral line.

reaction rates control both isotopic abundances in the ejecta and the dynamics of the collapse and explosion [52, 51].

1.4 Calculations and Measurements of EC Rates Circa 1980

Electron captures (EC) can be either Fermi ($\Delta L = \Delta S = 0$) or Gamow-Teller ($\Delta L = 0, \Delta S = 1$) transitions. Inclusion of Fermi transitions is a trivial addition[5] in the calculation of total electron capture rates. Gamow-Teller transitions, on the other hand, are far more complicated to calculate and so are extensively studied both theoretically and experimentally. The rest of this work, therefore, focuses exclusively on the Gamow-Teller transitions.

1.4.1 Problems with the FFN (and Other) Libraries of Weak Rates

Reaction rates for β capture and β decay at temperatures and densities of astrophysical interest are largely taken from the Fuller, Fowler and Newman (hereafter, FFN) catalog of 1982 [36, 37, 38]. This catalog does not include A$\geq$60 and some isotopes for A$\leq$60. Furthermore, these FFN rates are based on the Independent Particle Model, which was later shown to systematically overestimate EC, in some cases by as much as two orders of magnitude. Recent reviews (e.g. Langanke, et al [57]) outline the need for and consequences of a new and improved library of weak rates. The results are summarized here.

First, more modern calculations show that EC on nuclei with masses as high as A=65 play a non-trivial role in type I SNe. For type II SNe, masses as high as A=112 should be included in astrophysical models. While no single nucleus controls the

[5]The simplicity of the Fermi transition calculation is rooted in the fact that the transition only involves the isospin operator.

macroscopic SN dynamics or isotopic abundances, "Top 5" lists of nuclei for various progenitor masses are published in Heger et al [47]. The lists vary with progenitor mass, usually tabulated for 10, 15, 20, and 40 solar masses. Changes in EC rates for any one nucleus do not necessarily make a clear, direct change in SN dynamics. The complex relationships between the many macroscopic and microscopic variables requires that the library of weak interaction rates as a whole be reliable without systematic or significant deviations from the actual EC rates for stellar environs. Since most weak interaction rates are based entirely on theoretical calculations of Gamow-Teller strength distribution where there is no corresponding data, the theoretical calculations and the assumptions or theoretical methods must be checked where possible by the experimental nuclear physics community. Charge-exchange (CEX) data are the best consistency check available.

The present data represent the pilot experiment in a (t,^{3}He) campaign at the National Superconducting Cyclotron Laboratory to both study linearity breaking in the (t,^{3}He) probe of Gamow-Teller strength distributions and to study the reliability of different theoretical calculations of B(GT) in the different nuclear shells of interest, which also address nuclear structure issues.

1.5 Translating Nuclear Physics to Astrophysics

The measurements and calculations of weak transition strengths at zero temperature lie entirely with the nuclear physics community. Implementation of weak rates at finite temperatures in models of SNe lies entirely with the astrophysics community. However, the conversion of Fermi and Gamow-Teller strength distributions into electron capture rates historically is done by a handful of niche intermediary theorists

with a nuclear physics pedigree and a toe in the astrophysics camp. Experimental measurements appear in the literature either as cross sections or as B(GT) distrubutions and are thus unusable in SN models. With reliable weak transition strengths in hand, calculating finite temperature weak reaction rates is fairly straightforward. Understanding the foundation of these measurements and calculations and the related baggage, however, is not straightforward.

Either for computational simplicity or for an unwillingness by the astrophysics community to depart from tradition, information on weak reaction rates are stored only for a specific set of temperatures and stellar densities as chosen arbitrarily in Refs. [36, 37, 38, 39]. As a consequence of manpower issues and the nuclear physics culture, nuclear experimental data of the last two decades were not incorporated either directly or indirectly in most reaction rate libraries used in SN models until very recently. Additionally, nuclear data of the last two decades is also not included in most nuclear interactions produced by theorists, interactions which are basic inputs for theoretical strength calculations by Langanke, et al, for example. There are some reasons for this omission, partly involving manpower and motivation and partly involving an aesthetic interest in avoiding the mixing of systematic errors in the relative reaction rates.

Some long-used interactions, such as USD for the *sd*-shell [83], have been updated to include more modern measurements [12, 13]. Updated interactions, however, are typically not updated for charge-exchange reactions in particular, and so are not necessarily the optimal interaction to use in DWBA and Shell Model codes. *Updated interactions appropriate for charge exchange purposes are highly desired (both*

by experimentalists and the theorists who calculate modern weak interaction libraries), especially in the pf-shell mass region.

1.6 Historical Context: An Editorial

Every physics thesis has to satisfy several criteria and face two important questions. 1) Is this thesis interesting? 2) And why is it interesting *now*?

Are Gamow-Teller strengths interesting? In the context of understanding nuclear structure, the answer is yes. In the context of supernova dynamics peri-collapse, most definitely yes. This question is answered in Chapters 1 and 2.

Why go CEX crazy now? Now is an exciting time in nuclear astrophysics in general. Several factors are coming together, especially since 1995, to generate increasing interest in nuclear astrophysics as a whole- an era that started in the 1980s and continues today with considerable momentum both in the physics and astronomy communities, with support from the general public.

Now is also an exciting time specifically for the study of supernovae. Supernovae, very complex phenomena, combine scales separated by several tens of orders of magnitude, combine both the weakest of all the fundamental forces, gravity, and the much stronger nuclear forces on equal footing. Perhaps more than any other, this field is highly multi-disciplinary; models are at once heavily dependent on good nuclear reaction rate libraries with reasonable nuclear structure; astronomical observation of light, neutrinos and the so far ellusive gravity waves; good models for macroscopic dynamics such as those for stellar convection; and the availability of unreasonable computational speed and efficient algorithms to make calculations tractable. The fact that all facets of this field have made substantial improvements since its start

in the 1940s and many have *recently* made interesting advances is what makes the potential for a discontinuous jump in understanding supernovae real and the interest now so palpable. In particular, constraints discussed in section 2.2 make this hadronic probe an important tool to develop now.

One particular problem plaguing the nuclear (astrophysics) community is its poor communication between the producers and users of nuclear data. Since nuclear science is used by a variety of fields, nuclear energy producers being another such user, the data bases are usually not tailored for a particular use. Though the communication is still not seemless, there have been significant strides near the turn of the century to establish stronger links between the demand and supply sides of the nuclear data market. An example of advancement in establishing academic cross-pollenation is JINA- The Joint Institute for Nuclear Astrophysics- a relatively new entity designed to improve communication and facilitate collaboration between the nuclear physics and astrophyics groups. This organization channels funds to support individual collaborations, specific experimental projects to address crucial data needs, workshops to bring the larger community together to address specific topics in nuclear astrophysics, and outreach projects to raise public awareness and interest. JINA's calling card (and part of its power) is its trendy image- flat-screen Mac toting young scientists with a laid back attitude and a penchant for thinking outside the box. Aside from direct success, JINA serves to encourage other groups to invest in smarter organization and more transparent communication across fields.

The general public asks savvy questions about the origin of elements, our understanding of stellar and cosmic structure and evolution, owing more to popular culture than to improved general science education. Popular television shows, like CSI and

NCIS that give sex appeal to forensic scientists and glorify detailed new visualizations of everyday processes, serve to educate the public and fuel a demand for more answers to previously sterile questions. The very culture of how scientists ask questions and their rules of engagement for addressing these questions is taking on a new flavor in the public eye. Physicists often mistakenly assume the general public's interest is inversely related to the complexity of a given science: this is patently false. Such topics as relativity and string theory enjoy tremendous public appeal not despite the complexity, but because of the same richness that attracts the scientists. Albert Einstein and Brian Green are important to the physics community both for their research and for their success in generating public interest.

The public interest serves two ends. First, public support of projects like Hubble influence funding levels and the sustainability of programs. Funding for the $1B new Rare Isotope Accelerator is impossible to find now, but over night tens of billions are suddenly on the budgetary table for a totally unnecessary NASA program to research the improbable colonization of Mars. Second, the public perception of science as a whole influences the attraction of science majors and ultimately the pool of scientists available to growing subfields. Manpower is a critical issue in nuclear physics now, and the future of the field is heavily dependent on the next 15 years.

CHAPTER 2

INTRODUCTION TO THE NUCLEAR PHYSICS: CHARGE-EXCHANGE REACTIONS, AND MOTIVATING HADRONIC PROBES OF WEAK REACTION RATES

> ... spontaneous disintegration of ling-lived, naturally occurring isotopes provides one source of information on nuclei. However, only a limited number of nuclei are accessible for study on this natural process and then only under a narrow range of circumstances. On the other hand, nuclear reactions can be induced in the myriad of pairwise combinations provided by stable or long-lived nuclei and over the wide range of energies provided by the accelerators in the physics laboratories of the world. Reactions therefore provide the greatest volume and widest range of nuclear data. The energy loss of a beam particle can be directly interpreted as an excitation energy in the target nucleus. Usually, however, the data acquire meaning for the structure of nuclei only after they have been interpreted through a reaction theory. The synthesis of such accumulated information into a coherent theory of the nucleus is the main subject of nuclear physics. [40]
> - Norman K. Glendenning

Because of the β-decay reaction limitations and the fundamental difficulty in measuring neutrinos, Gamow-Teller strength distributions (for electron capture in nuclei) are most actively studied with purely hadronic probes.

Chapter 2 presents the nuclear physics of charge-exchange reactions, the basis for using such probes, the framework of nuclear calculations employed in the analyses of Chapters 4 and 5, and the advantages of the present $(t,{}^3\mathrm{He})$ reaction in particular.

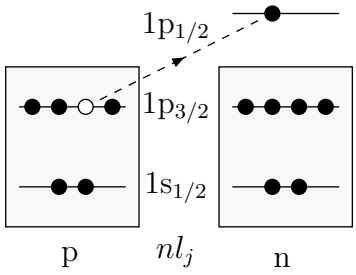

Figure 2.1: ^{12}C to ^{12}B GT transition particle-hole (solid-empty circles) excitation configuration. Proton (p) states are on the left and neutron (n) states are on the right. States are identified by the principle quantum number n, orbital angular momentum l, and total angular momentum j.

2.1 Charge Exchange: The Birds and the B(GT)'s

Charge-exchange probes[6] are used to study many aspects of nuclear structure. Gamow-Teller (GT) transitions are the spin-isospin flip reactions for which $\Delta L = 0$ and $\Delta S = 1$. The GT strength is defined by

$$B(GT^{\pm}) = \sum_{j=1}^{3} \left| \langle f || \sum_{k=1}^{A} \sigma_j(k) \tau_{\pm}(k) || i \rangle \right|^2 . \tag{2.1}$$

Figure 2.1 shows the single particle-hole[7] configuration for a GT transition from ^{12}C to ^{12}B. In addition to the $1p_{3/2} \rightarrow 1p_{1/2}$ isospin-flip transition drawn in Fig. 2.1, the $1p_{1/2} \rightarrow 1p_{1/2}$, $1p_{1/2} \rightarrow 1p_{3/2}$, and $1p_{3/2} \rightarrow 1p_{3/2}$ transistions also contribute to the low-lying $\Delta L = 0$ strength in the energy spectrum. Likewise, Fig. 2.2 shows two typical low-lying GT transitions from ^{24}Mg(t,^{3}He)^{24}Na. For the case of ^{12}C, the

[6] A glossary of common nuclear terms in this text is in Appendix C for the nuclear illiterati.

[7] Proton holes are sometimes called π-holes, not to be confused with pie-holes.

structure of the occupied and unoccupied single particle states makes for a simple response at low excitation energy.

It is important to note that while all GT transitions are interesting, not all transitions can be easily measured. For example, excitation energy regions where the high energy-level density challenges the experimental resolution carry higher uncertainty in the B(GT) extraction and often harbor hiding places for highly fragmented strength. For the purpose of calculating electron capture in SNe, however, the total integrated strength S^+ is not as important as the magnitude and location of low-lying strength [71, 72]. Consequently, experimental data providing even incomplete information on the structure of medium-mass nuclei, for example, is highly valueable for improving weak reaction libraries for SN modellers[8].

2.2 Supernovae and B(GT) Distributions

In supernova model reaction networks, the rate of electron captures λ on a nucleus of mass A and charge Z is

$$\lambda = \frac{ln(2)}{K} \sum_i \left(\frac{(2J_i + 1)e^{-E_i/(k_B T)}}{G(Z, A, T)} \sum_j B_{ij}(GT)\Phi_{ij} \right), \tag{2.2}$$

where i (j) is the initial (final) nucleus state in the electron capture, k is a kinematical factor, T is the temperature, and Φ_{ij} is a phase space factor. In this equation, experimental nuclear physics aims to determine the distribution of Gamow-Teller strength (B(GT)) as measured in the lab for comparison with the theoretical values calculated with the various interactions for each of the different nuclear shells.

[8]The low-lying strength distribution certainly is not the only ingredient in SN modelling. For example, high energy neutrinos can stimulate transitions at much higher energies at later stages in SN evolution. So far, that sector of the weak reaction rate libraries is largely filled by theory where experiment is in the dark.

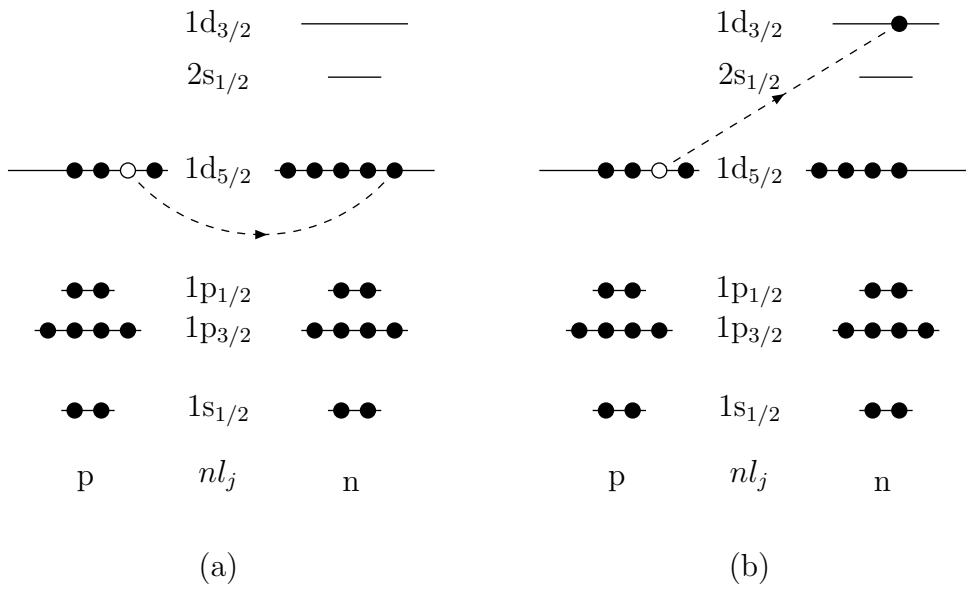

Figure 2.2: Two possible particle-hole excitation configurations for GT transitions from ^{24}Mg to ^{24}Na. In each, proton (p) states are on the left and neutron (n) states are on the right. States are identified by the principle quantum number n, orbital angular momentum l, and total angular momentum j.

These reaction rates, or λ's, are not calculated for every temperature during SN explosions. Until the late twentieth century, the rates were calculated for a grid of discrete values of mass density ρ and temperature (from 0.01 to 100 billion Kelvin) as prescribed by Fuller, Fowler and Newman in the early to mid-1980s [36, 37, 38, 39].

2.3 Linking hadronic probe cross sections and extraction of B(GT)

Measuring Gamow-Teller strength through β decay and capture alone is insufficient for the purposes of astrophysical modeling. Ignoring technical feasibility in

performing such measurements, β decay is energetically constrained and such experiments often extract strength for only the first few MeV in excitation of the final state for some nuclei. These measurements clearly omit most of the first 10 MeV in excitation energy, which is essential both for astrophysical applications and for the broader field of nuclear structure. For the early stagest of type II SNe, the energy regions of interest are temperature dependent and most sensitive to the lowest lying states. Even so, having distributions for the first MeV is not sufficient for SN modelling, especially at higher temperatures (i.e. later SN stages). For nuclear structure, individual states of equal J^π can be separated on the scale of MeV or smaller and energetically bound by up to several tens of MeV along the valley of stability.

The modus operandi for the last 20 years in the nuclear physics community has been to use hadronic charge-exchange experiments to measure B(GT), taking advantage of the common reduced matrix elements present in both the strong and weak forces. Since nuclear physicists do not measure electron-capture reaction rates but the structure of weak strength distributions, the hadronic probe reaction energy of interest, instead, is that for which the $\sigma\tau$ component in the effective interaction dominates and the non-spin flip component is small compared to the spin-flip component [58, 34]. Though the lower bound is somewhat debated, the reaction energy of interest for measuring this structure is a window of 100 to 400 MeV/nucleon[9].

The extraction of weak transition strength from nuclear CEX data is based on a proportionality between the weak transition strength and the CEX differential cross section at zero momentum transfer ($\frac{\mathrm{d}\sigma}{\mathrm{d}\Omega}(q=0)$ derived in Eikonal approximation [78].

[9]By comparison, the triton bombarding kinetic energy is two orders of magnitude higher than that of typical electron kinetic energy in capture during SNe.

For Gamow-Teller transitions:

$$\frac{d\sigma}{d\Omega}(q=0) = KN_{\sigma\tau}|J_{\sigma\tau}|^2 B(GT) = \hat{\sigma}_{GT} B(GT). \tag{2.3}$$

Here, K is a kinematical factor $K = \frac{E_i E_f}{(\hbar^2 c^2 \pi)^2}$ (where $E_{i(f)}$ is the reduced energy in the incoming (outgoing) channel), $N_{\sigma\tau}$ a distortion factor defined by the ratio of distorted-wave to plane-wave cross sections, and $|J_{\sigma\tau}|$ is the volume-integral of the central $\sigma\tau$ interaction. The factor $KN_{\sigma\tau}|J_{\sigma\tau}|^2$ is often referred to as the GT unit cross section, $\hat{\sigma}_{GT}$.

The cross section for momentum transfer $q = 0$, requiring both the Q-value of the transition and the scattering angle to be zero, is obtained by extrapolating the data using:

$$\frac{d\sigma}{d\Omega}(q=0) = \left[\frac{\frac{d\sigma}{d\Omega}(q=0)}{\frac{d\sigma}{d\Omega}(Q,0^\circ)}\right]_{\text{DWBA}} \times \left[\frac{d\sigma}{d\Omega}(Q,0^\circ)\right]_{\text{exp}}. \tag{2.4}$$

In this equation, 'DWBA' refers to calculated values in the Distorted-Wave Born Approximation using FOLD as described later in section 2.6. The experimental cross section at $\theta = 0^\circ$ is obtained by fitting the calculated Gamow-Teller angular distribution in DWBA to the measured angular distribution.

With the experimental differential cross section extrapolated to zero degrees, the B(GT) can then be extracted as

$$B(GT) = \frac{1}{\hat{\sigma}_{GT}} \left[\frac{\frac{d\sigma}{d\Omega}(q=0)}{\frac{d\sigma}{d\Omega}(Q,0^\circ)}\right]_{\text{DWBA}} \times \left[\frac{d\sigma}{d\Omega}(Q,0^\circ)\right]_{\text{exp}}. \tag{2.5}$$

For tests of theoretically predicted Gamow-Teller strength distributions of importance for stellar evolution, data with resolution better than the 0.5 MeV or so of the (n,p) probe are important since the electron-capture rates in the stellar environment are sensitive to the details of the low-lying transitions [44].

2.4 Available Charge-Exchange Probes

The $(t,^3\mathrm{He})$ probe as developed here is one in a series of hadronic probes used in the last quarter of a century. These probes have inherent advantages and disadvantages, some of which compliment each other. For overviews of medium-energy hadronic probes and their connection to β decay, see Refs. [45, 65, 70]. This family tree of probes in both the electron capture and decay directions are briefly described here.

2.4.1 (n,p) and (p,n)

The most basic of the hadronic probes are the (n,p) and (p,n) reactions[10], which have a rich history as tools for measuring the isospin-flip response of nuclei. Reference [78] of 1987, for example, details the correspondence between (p,n) reaction zero-degree cross sections at proton energies of $E = 50-200$ MeV and both the Fermi and Gamow-Teller strengths for eight different nuclei with masses of $A = 7-208$ using the single-step direct-reaction distorted-waves impulse approximation model. Here, gains in energy resolutions easily follow with improvements of the time of flight measurements for the neutron, which easily best 200 keV. In the opposite direction, (n,p) reactions above 100 MeV suffer comparatively with a poorer energy resolution, often of 1 MeV or worse, owing to the neutron production mechanism and the fact that such neutral particles cannot be separated by energy in magnetic spectrometers as charged particles can, such as in Refs. [55, 28]. The experimental (n,p) energy resolutions is the single largest drawback for this probe.

[10]The electron-capture direction is often called the (n,p) direction, and the electron-decay or β^+-capture direction is often called the (p,n) direction. The light $(\pi^{\pm},\pi^0)$ reactions also induce isospin flips, but are not relevant here since pions are scalar mesons, which cannot induce spin flips.

2.4.2 (d,^{2}He)

One alternative to the (n,p) reaction is the (d,^{2}He) probe. Experiments have been performed at RIKEN [64], Texas A&M [86] and at KVI [69] where the best resolutions have been achieved (∼130 keV at E_d=85 MeV/A). By selecting small relative energies of the outgoing protons in the unbound ^{2}He system, selectivity for spin-transfer transitions is enhanced [17, 63]. Gamow-Teller distributions have been extracted through the (d,^{2}He) reaction in a variety of nuclei [43, 35], focusing on cases of importance for astrophysical applications such as the medium-heavy mass nuclei. (d,^{2}He) has been performed at AGOR with the BBS magnetic spectrometer for several nuclei in the *sd*- and *fp*-shells [68, 42];. at RIKEN e.g. Okamura (1995) [64] on ^{12}C and Nuzeki (1994) [62] on ^{24}Mg and sd-shell nuclei ^{26}Mg and ^{28}Si.; and at Texas A&M University (starting with Betker et al. in 1989 [11]) with large solid angle but energy resolution of only 350 keV or worse.

The (d,^{2}He) reaction is an unusual charge-exchange probe in that the outgoing protons (identified with the ^{1}S$_0$(T=1) state) are unbound, thus making the reverse reaction, namely (^{2}He,d), unavailable as a complimentary tool. Having no data in the (^{2}He,d) direction is a disadvantage, since additional information from relations such as the Ikeda Sum Rule for total strengths S$_\pm$ ($S_-(GT) - S_+(GT) = 3(N-Z)$) is then not available. On the other hand, the (d,^3He) probe naturally selects for spin-flip transitions only, reducing certain backgrounds in the determination of GT strength.

2.4.3 (t,^{3}He) and (^{3}He,t)

The (t,^{3}He) experiments before 1990 used much lower triton energies due primarily to the fact that higher beam energies were not available at the time (1980s). The

(t,^{3}He) probe was studied extensively in the 1970s and 1980s at the Los Alamos Van de Graaff accelerator with primary triton energies of E_t = 17-24 MeV [32, 33, 2]. Other facilities with higher energy triton beams generally did not meet the 300 MeV threshold for intermediate energy studies. To address the lack of dedicated tritium ion sources, the NSCL developed a secondary triton beam from the fragmentation of an α-primary beam [25, 26]. The ^{12}C(t,^{3}He) reaction was successfully measured for small scattering angles in the late 1990s. These data predate both the commissioning of the S800 high resolution magnetic spectrometer at the NSCL and the configuration of the A1900 mass fragment separator [11]. The cross section was measured for small scattering angles, but lack of a measured angular distribution impaired determination of accurate Gamow-Teller strength. A later experiment, after the commissioning of the S800 at the NSCL, measured angular distrbutions for the ^{12}C,^{58}Ni(t,^{3}He) reactions and extracted Gamow-Teller distrbutions for comparison with the two inconsistent (n, p) and (d,^{2}He) data sets [23].

The present data set benefits from use of both the A1900 mass separator and the S800 spectrometer (available together only after 2002) and from higher triton beam intensity from the fragmentation of the intense ^{16}O primary beam. Generally, energy resolution for the (t,^{3}He) probe is facility-determined, not an inherent property of the reaction, and faces limits due to target thickness.

Though the magnetic spectrometer selects ^{3}He final state events and the intermediate energy of the triton beam favors the $V_{\sigma\tau}$ term in the potential, $J^\pi \neq 1^+$ transitions are indistinguishable in the focal plane detectors, on an event-by-event basis, from the desired $J^\pi = 1^+$ GT transitions. For given slices in excitation energy,

[11] The A1900 was preceeded by the A1200 mass separator.

the relative contribution of the various J^{π}transitions can be teased out statistically by decomposing the total angular distribution $(d\sigma(\Theta_{scat})/d\Omega)$ with that of the different ΔJ^{π} components. While the nuclei measured in this work (^{12}B and ^{24}Na) have clearly identifiable states, nuclei with more complicated structure require the separation of different (overlapping) ΔJ^{π} transitions through the above described multipole decomposition. This decomposition and extraction of GT strength require good descriptions of the angular distributions, and, therefore, a basic understanding of the reaction mechanism itself. No such comprehensive study exists at these intermediate energies for the (t,^{3}He) reaction.

The complimentary (^{3}He,t) reaction has recently undergone a systematic evaluation of the reliability for extraction of $B(GT)$s for a wide target-mass range with (slightly higher energy) $E_{^3He}$ = 420 MeV beams at RCNP in Osaka, Japan [12] [93]. This work at RCNP is interesting both for the broad target-mass range and for the relatively broad scattering-angle range. The (^{3}He,t) reaction can provide a consistency check both for relative cross sections and for B(GT) strengths for analogous states [92].

The present work lays the ground work for a similar study at the NSCL for the (t,^{3}He) reaction with E_t = 345 MeV. Once the reliability of the $B(GT)$ extraction is established, the CEX group will be able to address the reliability of theoretical placement of B(GT) in the electron-capture direction for medium mass nuclei for $A = 45 - 65$ and $A \leq 112$.

[12] A recent experiment measured differential cross sections for known weak transition strengths on ^{12,13}C, ^{18}O, ^{26}Mg, ^{58,60}Ni, ^{90}Zr, and ^{118,120}Sn target nuclei [90].

2.4.4 Heavier Probes

Interest in heavier probes is driven by the technical considerations for running charge-exchange reactions in inverse kinematics. Unstable nuclei, especially the very short lived, must be studied in inverse kinematics at rare isotope accelerators. For this geometry, where the heavier nucleus bombards the lighter nucleus, the hadronic probe must be made into a target of modest thickness. One option is to freeze isotopically enriched hydrogen and fight the constant battle of keeping the target frozen and sufficiently thin while the incident beam steadily dumps thermal energy into the target. Another option is to work with a compound target such as the cheap and readily available CH_2 foil, which requires a veto of either subtracting the charge-exchange spectra on the carbon or directly measuring the residual neutron from the (p, n) reaction. The cheapest and least challenging pure target is a solid foil of $Z>2$ nuclei.

Groups at the NSCL and RCNP [90] have completed test experiments using the (^{7}Li,^{7}Be*) reaction, the two facilities operating in inverse and forward kinematics respectively. The NSCL Charge Exchange group uses a known 430 keV gamma emitting low lying excited state in ^{7}Be in conjunction with the S800 spectrometer to tag the beam-like particle after the spin-isospin flip.

2.5 Proportionality Breaking

Extraction of Gamow-Teller strength is only as good as the proportionality between B(GT) and zero degree differential cross section at zero momentum transfer ($q = 0$). This linear relationship, however, is known to be broken in a few ways.

First, with charge-exchange reactions, the target nucleus can make a 1^+ transition (in the case of the ^{12}C and ^{24}Mg $N = Z$ targets, from the 0^+ ground states to a 1^+ states) in two distinct reactions. The $\Delta L = 0, \Delta S = 1, \Delta J = 1^+$ transition is the GT transition of interest. The $\Delta L = 2, \Delta S = 1, \Delta J = 1^+$ transitions[13] can be removed by decomposing the angular distributions into the $\Delta L = 0$ and $\Delta L = 2$ components. With the help of empirically based differential cross-section calculations such as FOLD, the analysis of the present data subtracts and accounts for this background explicitly. This background to the cross section will not likely be a major source of error in B(GT) extraction.

Second, the $\Delta L = 2, \Delta S = 1, \Delta J = 1^+$ portion may contain an interference contribution from the tensor-τ interaction (see discussion in Ref. [92]). From the nuclear structure and reaction view point, presents an interesting hurdle to extracting Gamow-Teller strengths. The role of this tensor interference is historically an often mishandled and misunderstood factor[14], even in seminal works on hadronic charge-exchange probes (e.g. see comments in Ref. [93] on Ref. [78]). The target can undergo a $\Delta L = 2, \Delta S = 1, \Delta J = 1^+$ transition for two geometries: for an angular momentum transfer of the target *relative* to the projectile J_R=0 or for J_R=2. The J_R=0 term is the source of interference that is not explicitly removed in this work. Experimentalists must take care to acknowledge this. One recent publication[93] estimates the contribution as a function of strength. (See page 93.)

The third source of linearity breaking in this work is additional cross section at small angles coming within a peak's energy window from nearby states for which

[13]Of the two, only the $\Delta L = 0, \Delta S = 1, \Delta J = 1^+$ transition is physically relevant for B(GT).

[14]The author and this work make no claim to superior clarity on the subject. Rather it is the very muddiness of this issue that makes charge-exchange reactions an active and newly reenergized subject matter.

$J^\pi \neq 1^+$. For the ^{12}C data, the nearest state to the ^{12}B 1^+ ground state is separated by a full 1 MeV, beyond the experimental or peak energy uncertainty. The (energy) tail of charge exchange on the deuterium in the target is more likely to overlap[15]. The sparce low-lying structure of ^{12}B makes intruding J^π states a non-issue. For the ^{24}Mg data, the E_x=1.3 MeV state in ^{24}Na, for example, carries the baggage of two J^π= 2^+ and 3^+ states within the energy uncertainty. This type of contribution to the cross section and its removal are discussed on a state by state basis. The cross section from these states are usually subtracted through a multipole decomposition of the angular distribution, which is generally more or less accurate with the availability of the structure of the residual nucleus.

Finally, Amos et al. [3] suggest that the radial dependence in the nucleon-nucleon interaction when combined with the Pauli principle on cross sections in the (n, p) direction could result in proportionality breaking for the very medium-heavy nuclei with astrophysical signficance. Whether this is born out in nature in the electron-capture direction will only be known once the NSCL amasses (t,^{3}He) data on more nuclei.

2.6 Distorted Wave Calculations of Angular Distributions for $J^\pi = 1^+$ Transitions with FOLD

The present data are interpretted through the direct reaction model of double-folded potentials in the model used in the code FOLD [24]. For a given transition in the target nucleus, the angular distribution of the cross section is calculated in the

[15]Because of the difference in reaction Q-value, charge exchange on the target deuterium appears (if at all) in the differential cross section as an overcount at larger scattering angles, away from zero degrees. With this separation, the deuterium does not alter the zero degree differential cross section to ^{12}B to within the experimental uncertainty.

distored-wave Born approximation. A basic description of the angular distribution calculations as used in the analyses of Chapters 4 and 5 is presented in this section. References [45] and [74] are excellent texts for broad overviews of direct nuclear reactions, including charge-exchange reactions in particular, and for a pedigogical framework for distored wave calculations and their use in evaluating isospin-flip differential cross sections.

The triton and ^{3}He system wavefunctions are taken from Variational Monte Carlo calculations from the Argonne group [66] as in Ref. [23]. The ^{24}Mg and ^{24}Na wavefunctions are calculated with the Woods-Saxon wavefunction routine in FOLD, using binding energies from OXBASH [16] shell model calculations with the USDB interaction [13] in the *sd*-shell model space. The USDB (2005) is a new version of the standard USD interaction for the *sd*-shell model space of 1983 updated to include the more recent experimental binding energies of the last two decades. Two versions of the 2005 update are available, labelled USDA and USDB, which differ primarily in the convergence criteria. Given the slight preference in ^{24,26}Mg(^{3}He,t) and ^{26}Mg(t,^{3}He) data for the USDB interaction, calculations of FOLD input such as one body transition densities are performed with the USDB interaction in this work; switching to the USDA interaction has no discernable effect on the angular distributions.

The distorted wavefunctions for the incoming triton and outgoing ^{3}He are the solutions of the usual Schrödinger equation,

$$(K + U)\Psi = E\Psi, \tag{2.6}$$

where the equation is solved separately for both particles, with the appropriate corresponding distorting potential for each particle. In this case, the distorting potentials are phenomenological descriptions of the interaction between the target and beam

particles. The distorting potential U is of the form

$$U(r) = V_C(r) + V(r) + iW(r) \tag{2.7}$$

where V_C is the usual Coulomb potential for a projectile-like nucleus (P) and a target-like nucleus (T),

$$V_C(r) = \begin{cases} Z_P\, Z_T\, e^2\, \frac{3-(r/R_C)^2}{2R_C} & \text{for} \quad r \leq R_C \\ Z_P\, Z_T\, e^2\, \frac{e^2}{r} & \text{for} \quad r > R_C, \end{cases} \tag{2.8}$$

and the nuclear potentials V and W take the Woods-Saxon form,

$$V(r) = \frac{V_0}{1 + e^{(r - r_v A^{1/3})/a_v}}. \tag{2.9}$$

R_C is $r_C A^{1/3}$, where r_C is the reduced Coulomb radius of 1.3 fm. V_0 (W_0) is the real (imaginary) well depth, r_v (r_w) is the radius, and a_v (a_w) is the diffuseness, all fit to elastic scattering data. (Tables for the Optical Model Parameters used in this work are given in Tables 2.1 and 2.2.)

There are no (t, t') elastic scattering data for E_t=345 MeV. Following previous work such as Refs. [82] and [92], the optical-model parameters for the triton are taken by scaling the ^{3}He depths by a multiplicative factor of 0.85 (as shown in Tables 2.1 and 2.2) and keeping the radii and diffusenesses for ^{3}He. The primary objective for these calculations is to generate reasonable angular distrbutions for the 1^+ transitions.

For ^{24}Mg, the optical model parameters are taken from a refitting of ^{3}He elastic scattering data on ^{28}Si [87] at 150 MeV/nucleon [16], following the work of Ref. [92]. These optical model parameters are entered into the WSAW routine in FOLD to generate wavefunctions for both the ^{12}C-^{12}B and the ^{24}Mg-^{24}Na systems.

[16]Large discrepancies were found between optical potential parameters for other nuiclei in Refs. [56] and [87], prompting a new fit of the scattering data.

Particle	V_0 [MeV]	r_v [fm]	a_v [fm]	W_0 [MeV]	r_w [fm]	a_w [fm]
triton	25.8	1.49	0.73	9.5	1.15	1.37
^{3}He	30.4	1.49	0.73	11.2	1.15	1.37

Table 2.1: The ^{12}C(t,^{3}He)^{12}B reaction optical-model parameters used in FOLD calculations [87].

Particle	V_0 [MeV]	r_v [fm]	a_v [fm]	W_0 [MeV]	r_w [fm]	a_w [fm]
triton	21.6	1.43	0.833	34.0	0.963	1.031
^{3}He	25.1	1.43	0.833	40.	0.963	1.031

Table 2.2: The ^{24}Mg(t,^{3}He)^{24}Na reaction optical-model parameters used in FOLD calculations [87].

The One Body Transition Densities (OBTD) for the ^{24}Mg(t,^{3}He)^{24}Na reaction are calculated in the shell model code OXBASH [16] in the proton-neutron formalism using the new USD-05B interaction [12] in the *sd*-shell space. For the case of the ^{12}C(t,^{3}He)^{12}B, the standard CKII interaction [22] is used in the *p*-shell model space.

The Love-Franey effective nucleon-nucleon interaction is the result of a fit of scattering data [58, 34]. The tensor-τ component in the interaction is set to zero. In FOLD, the Love-Franey effective nuleon-nucleon interactions are double-folded over the transition densities of the finite projectile-ejectile and finite target-residue systems to calculate the form factors used in the distorted-wave calculation. With these form factors, the distorted-wave born approximation generates reduced transition matrix elements or amplitudes. The cross section, then, is proportional to the square of these

amplitudes. Sections 4.4 and 4.5.2 present these angular distrbutions of the (t,^{3}He) differential cross sections from FOLD for both the ^{12}B and ^{24}Na residual nuclei.

CHAPTER 3

EXPERIMENTAL SET-UP: THE NSCL

The National Superconducting Cyclotron Laboratory (NSCL) in East Lansing, Michigan at Michigan State University is the premier rare isotope beam facility in the U.S. The K500 and K1200 coupled superconducting cyclotrons accelerate primary beams (from hydrogen to uranium) into massive (often beryllium) targets to produce a secondary beam of interest. The A1900 fragment mass separator culls the fast fragments and can deliver a wide variety of nuclear cocktail beams for experiments.

Current calculations for fragmentation cross sections to produce tritons are highly unreliable, underestimating the triton production by as much as a factor of 30. These calculations also provide little guidance on charge state (e.g. $^3He^+$) production. In preparation for the present experiment, the Charge Exchange Group at the NSCL ran a series of tests to optimize the production of a secondary triton beam with energies of interest for Gamow-Teller strength measurements. For further details on production of secondary triton beams from oxygen beams, see Ref. [50]. This chapter describes the triton beam and its production, the experimental set-up, the ^{3}He particle detection, and the reconstruction of the charge-exchange reaction.

3.1 The Secondary Triton Beam

Though there were many (t,^{3}He) experiments in the 1980s at places such as Los Alamos National Laboratory, those charge-exchange experiments generally used a triton beam of E=5-40 MeV/nucleon. The advent of a triton beam with medium energy ($\geq$85 MeV/nucleon) only occurred in the mid-1990s, most notably the secondary triton beam produced at the NSCL from an α primary beam. The following subsection describes the improved production configuration as used in the present data for a secondary triton beam produced from a ^{16}O primary beam; the yields from ^{16}O and ^{18}O are compared in greater detail in Ref. [50].

3.1.1 Secondary Triton Beam Production

Why use a secondary beam instead of a primary beam? A triton primary beam is, afterall, the experimenter's choice for producing a high quality, high intensity triton beam for (t,^{3}He) experiments. Such an ideal beam offers a valuable improvement in energy resolution of the incident triton beam and unparalleled purity. Secondary beams are by nature essentially cocktail beams with greater energy spread (from the production mechanism), reduce emittance at the cost of beam intensity, and come with a substantially lower triton intensity than the primary beam by virtue of the production mechanism.

With a half-life on the order of a decade, there are no natural sources of tritium[17]. Triton ion sources thus have to come *from reactors*. As with any material produced at a reactor, the triton primary beam comes with added bookkeeping baggage; every path of every triton coming from such an ion source must be measured for radiation

[17]Tritium is the atom; a triton is the tritium nucleus.

levels, and the sum of the radiation put into the ion source must be accounted for-which means regularly taking radiation measurements (for tritium activity in particular) along the entire beam line, essentially for the life of the facility. A triton primary beam is, therefore, somewhat labor prohibitive. While technically feasible, the NSCL has so far elected to not use a primary triton beam [73].

The natural alternative to the reactor tritium source is the fragmentation of a heavier and readily available primary beam. Selecting the heavy primary beam for maximum triton secondary beam intensity is non-trivial. As stated previously, current calculations [50] (such as those with the EPAX 2.5 parameterization [77, 76] as performed by LISE++ [5, 79]) for fragmentation cross sections to produce tritons are unreliable. In preparation for the present experiment, the Charge Exchange Group at the NSCL ran a series of tests to optimize the production of a secondary triton beam with energies of interest for Gamow-Teller strength measurements, 100-400 MeV/nucleon.

The present triton secondary beam is produced with an ^{16}O primary beam of E=150 MeV/nucleon instead of the α primary beam used in the late 1990s for two reasons. First, α primary beams at the NSCL require decoupling the two cyclotrons; decoupling the K500 and K1200 cyclotrons requires at least a couple of days of overhead before and after running in stand-alone mode. Since there are usually no other experiments running in stand-alone mode, this is a significant burden on the facility for a single experiment that may run for a week. Second, test experiments showed that for available primary beam intensities the ^{16}O primary beam improves the triton yield by a factor of 5-10 over the NSCL beam list[18] α primary beam fragmentation.

[18]The NSCL no longer provides the α primary beam; the present NSCL beam list does not include a primary α beam intensity, but typical intensities have historically been a factor of ten lower

While triton yields from the 120 MeV/nucleon ^{18}O primary beam are higher, the ^{16}O primary beam is favored for the higher triton energy; at optimal optical settings for ^{18}O, the triton energy $E_t = 82$ MeV/nucleon, short of the 100 MeV/nucleon lower bound required for the physics. On the other side, the upper bound on the NSCL incident triton energy is limited by the practical restriction of the maximum magnetic rigidity (Bρ= 4.8 T·m) available at the NSCL, which corresponds to 115 MeV/nucleon.

Though the stability of the high intensity ^{16}O primary beam for the present data can be described as sketchy at best, the reliability and stability of this beam has since been dramatically improved for subsequent experiments as demonstrated a year later in NSCL Experiment 05504 in December 2005 and NSCL Experiment 06032 in February 2008. As a result of the present experiment, the NSCL cyclotron vaults have been reconfigured to reduce neutron damage to solid state equipment (a frequent cause of lost beam time during the present experiment), and magnets in the magnetic spectrometer vault have been realigned for improved transmission, angular acceptance and ray tracing.

The radio frequency (RF) for the ^{16}O primary beam is 23.8 MHz, giving a minimum separation between bunches of 4.20 ns. As shown in Fig. 3.1, the ^{16}O is partially ionized, accelerated through the K500 cyclotron to an energy of 13 MeV/nucleon, stripped of the remaining 5 electrons by a carbon stripping foil and further accelerated by the K1200 cyclotron to an energy of 150 MeV/nucleon. For the present

than present day oxygen primary beam intensities. The safety issues posed by the large neutron production for α on Be are a major consideration in using primary α beams for the production of tritons.

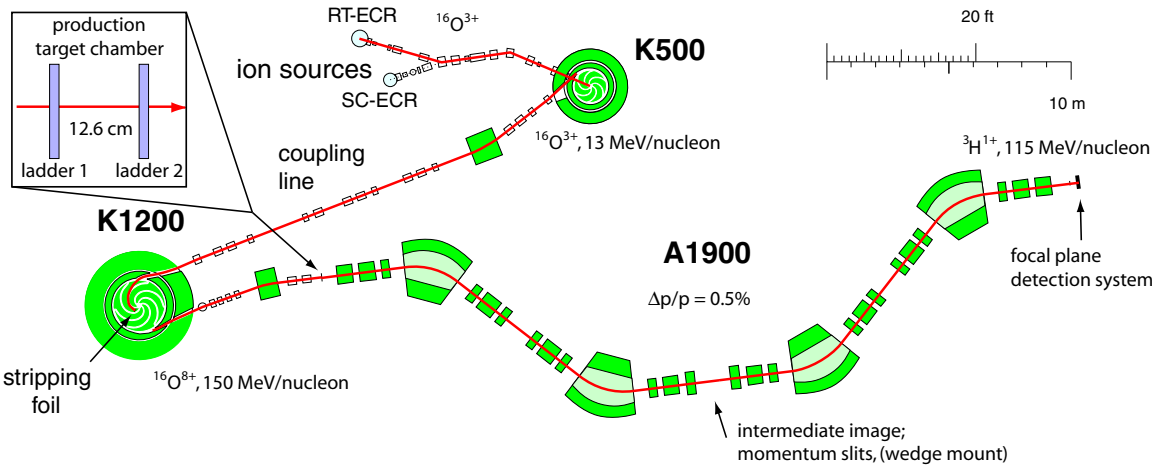

Figure 3.1: Coupled Cyclotron Facility Configuration: A primary beam of ^{16}O is accelerated in the coupled cyclotrons K500⊗K1200 to 150 MeV/nucleon. The ^{16}O beam on the Be target produces a cocktail secondary beam that is then magnetically separated in the A1900 projectile fragment separator [60]. The secondary beam travels through a switchyard before reaching the experimental vault. (Color.)

experiment, the ^{16}O primary beam is fragmented by a 3526 mg/cm^2 beryllium production target placed entirely at the first ladder position in the A1900 mass separator target box. Triton rates for Be production target masses over two ladders varying from 1480 to 5524 mg/cm^2 are described in Ref. [50].

The many fragments from the collision with beryllium are sifted in the A1900 by energy and mass-to-charge ratio A/Z. Figure 3.2 shows the secondary beam species content after the A1900, which is dominated ($\geq$85%) by tritons. With the relative purity of the E_t=115 MeV/nucleon secondary beam, no wedge is used at the intermediate image of the A1900 to suppress background. After the A1900 focal plane, the tritons travel through a switchyard (not shown) before reaching the object box of the S800, shown in Fig. 3.3.

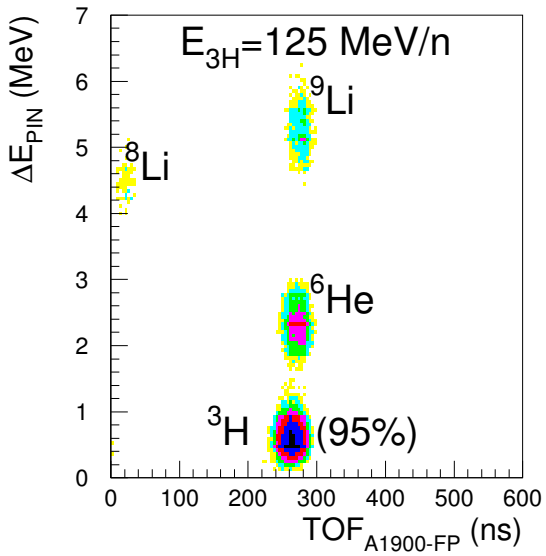

Figure 3.2: Typical particle identification spectrum measured in the focal plane of the A1900 during the triton production experiments: the energy loss in the PIN detector is plotted versus TOF. The different species are clearly separated.

The full momentum acceptance is limited to $dp/p_0 = 5 \times 10^{-3}$ (or $\pm 0.25\%$) by slits at the A1900 intermediate image. In preparation tests and during the present experiment, the optimal transmission of the secondary beam from the A1900 focal plane to a 1 mm in-beam scintillator at the object of the S800 analysis line was 60% and from the object to the S800 target in the scattering chamber was 85%, resulting in an overall transmission of 50%[19]. Since the alignment of the S800 magnets in 2007, subsequent experiments have enjoyed higher total transmission of approximately 80%, nearly doubling the net triton yield per particle nano-ampere of ^{16}O extracted from the cyclotrons.

[19]The overall transmission drops for triton energies above 115 MeV/nucleon, which is a primary consideration in determining the upper limit on the triton energy.

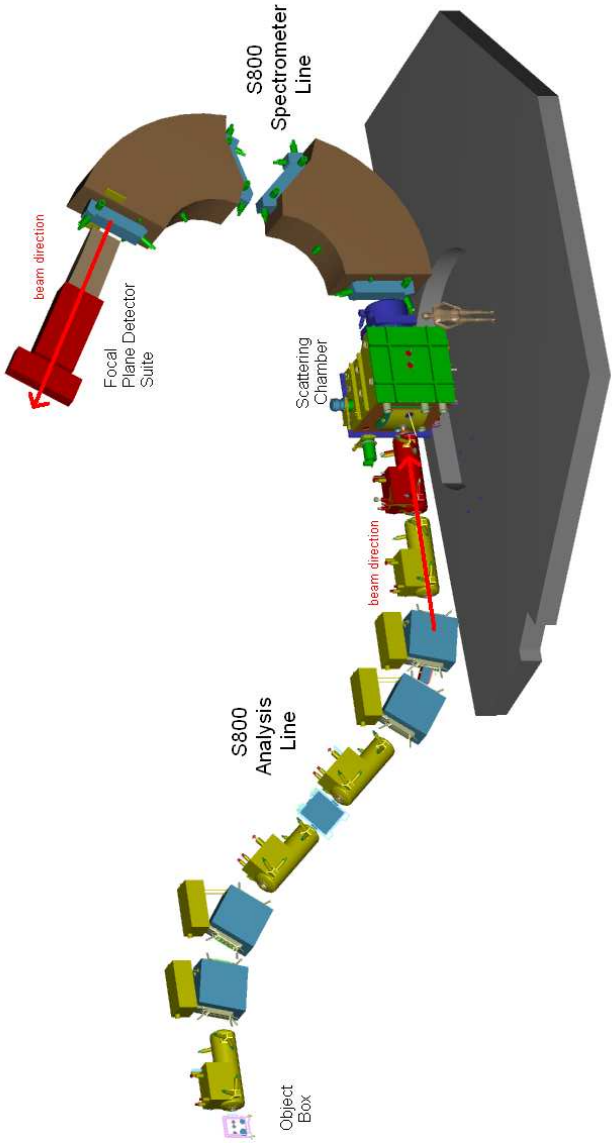

Figure 3.3: S3 vault configuration (color). The secondary triton beam travels through the S800 Analysis Line to the target in the Large Scattering Chamber. The outgoing ^{3}He particle travels through two large dipole magnets to the focal plane detector suite two stories above.

The primary ^{16}O beam intensity of 100 pnA (particle nano-amperes) with the present transmission produces triton beam intensities on target of 5×10^6 particles per second (pps). The analysis in Chapter 4 represents 1.77×10^{10} tritons on the CD_2 target and 2.75×10^{11} tritons on the ^{24}Mg target over the course of two days.

3.1.2 Calibration of the Triton Beam Intensity

Since the B(GT) measurement is essentially a cross-section measurement, the intensity of the triton beam and an understanding of the inherent uncertainties in the intensity are important; systematic and statistical uncertainties in the triton beam intensity contribute directly to the uncertainty in the Gamow-Teller strength. Placing a scintillator in front of the target would give a good measure of the incident beam intensity, but there are noteable problems with using such direct methods. A scintillator in the object box upstream from the S800 analysis line would introduce an incoherence between incident triton energy and position on the target in the dispersive direction, a correlation which is essential to optimal energy resolution in dispersion matching mode. A 1 mm thick scintillator immediately in front of the target would produce ^{3}He from charge-exchange reactions on the scintillating material, generating enormous background that would outweigh the signal events by more than 5 to 1. Active in-beam monitoring devices are not used in this experiment.

Instead, we use an indirect method to monitor the variations in the beam intensity in real time. Inside the first turn in the A1900, undesired and more proton-rich species in the cocktail beam hit a Faraday bar while the tritons and other A/Q=3 contaminants (e.g. ^{6}He) continue down the mass separator. For a given tuning of the primary beam, this current on the Faraday bar is assumed to be proportional to the

secondary triton beam intensity in the A1900 and proportional to the beam intensity on target at the S800 spectrometer.

The high beam intensity on the scintillator at the S800 target position pushes the plastic scintillator into a non-linear response regime in which the scintillator begins to saturate. A typical calibration data set of Faraday bar current with scintillator count rates is shown in Fig. 3.4. The relation between tritons counted in the scintillator and the Faraday bar current is fit with

$$S(F) = a\left(1 - e^{(-F+b)/c}\right), \tag{3.1}$$

where S is the scintillator count rate, F is the Faraday bar current in nAmps, and a, b, and c are the free parameters fit to the calibration data. The actual triton rate on target is calculated for the Faraday bar current from the slope of the exponential at the Faraday bar current for which S(F)= 0 tritons per second:

$$T(F) = \frac{a \cdot F}{c}. \tag{3.2}$$

A 10% uncertainty in the slope contributes a 10% uncertainty in the normalization of absolute cross sections, while contributing less to relative cross sections.

Regular calibrations of the triton rate on target as a function of the Faraday bar current account for changes such as deviations in beam line transmission from the fragment separator to the target (changes which can and do occur with each cyclotron tuning) and changes in the A1900 intermediate image momentum slit (dp/p_0) settings.

As shown in Fig. 3.2, the beam intensity must be corrected for the impurities in the beam. For a triton beam of 115 MeV/nucleon, the cocktail beam is approximately 87% tritons as shown in Fig. 3.5.

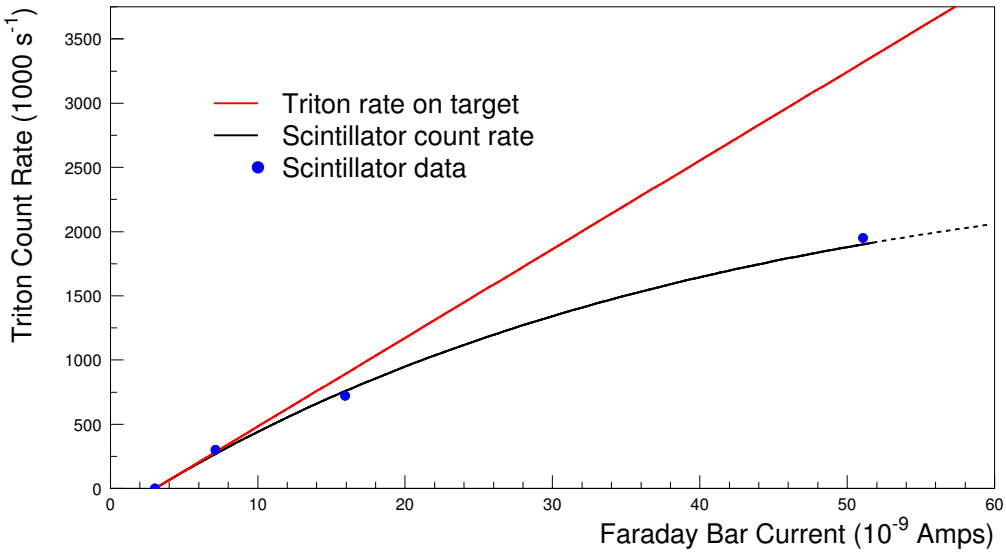

Figure 3.4: Typical correlation between Faraday bar current and scintillator count of tritons in the scattering chamber. The black curve is the fit of the data to the three parameter Eq. 3.1. The red line is the estimated triton count rate on target as a function of Faraday bar readings, calculated using the slope of the black curve where the triton count rate is zero. Statistical error bars are smaller than the data symbols.

Finally, the incident number of tritons on the 1.27 cm wide ^{24}Mg target must be corrected by an additional factor to account for tritons that miss the slightly more narrow target foil as compared to the 2.0 cm wide calibration ^{12}C target foil. (See target specifications in Table 3.1.) The distribution of the tritons in the non-dispersive direction gives an estimate of the tritons lost on the more narrow ^{24}Mg target. Specifically, a close examination of the distribution in the non-dispersive direction (y_{ta}) for the charge state and the main peak shows a discrepancy in the tails. Since the charge state angular distribution nearly has a zero degree deflection, this difference in the tails is evidence of the y_{ta} dependence on the angular acceptance of the spectrometer.

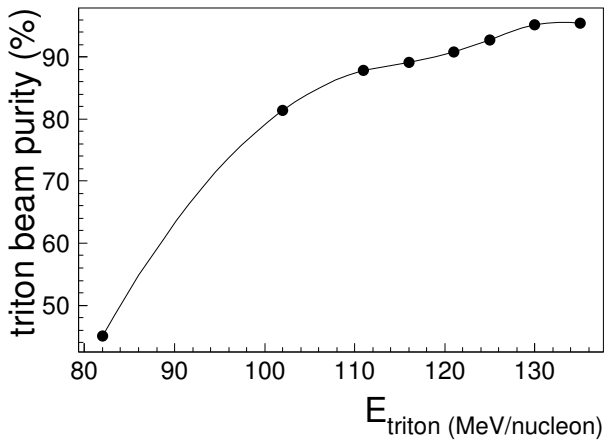

Figure 3.5: Secondary triton beam cocktail purity[50] as a function of triton beam energy in MeV/nucleon. Statistical error bars are smaller than the data symbols.

The GT transition angular distribution is more broad by comparison and is more truncated. The y_{ta} gate does not include this region in the analysis, and therefore does require a further correction to the cross section. See section 4.5.2 for more details. The total error in the number of incident tritons is discussed in the calculation of differential cross sections for each target in Chapter 4.

3.2 The Target Ladder

In the Large Scattering Chamber, multiple targets are mounted on a target ladder for quick changes under vacuum. Table 3.1 lists the target foil specifications for all data taken in Experiment 03018, including those not included in the present analysis. A viewer, or aluminum plate coated with a zinc oxide[20] (ZnO) phosphor paint, is mounted on top of the target frame at a 45 degree angle for easy viewing through

[20]ZnO is commonly called zinc white or calamine.

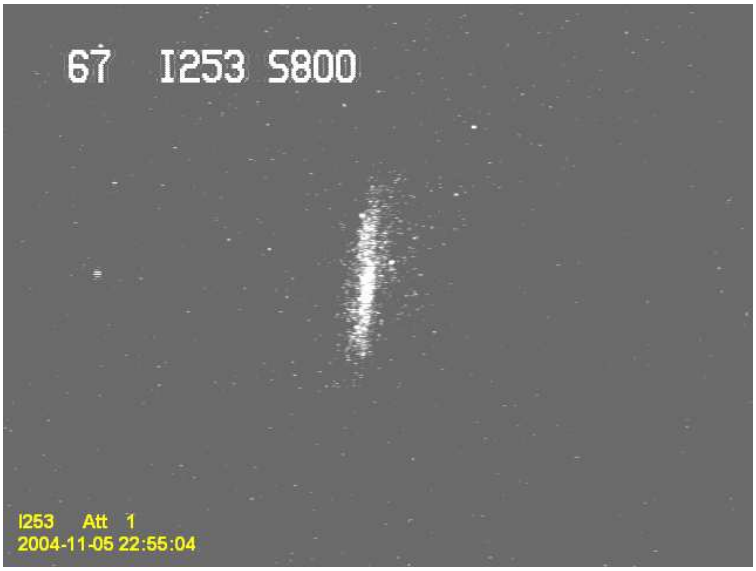

Figure 3.6: Typical triton secondary beam spot on a phorphor coated metal plate in the Large Scattering Chamber as seen by an image intensifying camera. The vertical dimension of the beam spot corresponds to 5 cm in the dispersive direction, and the horizontal dimension is a slightly distorted view of non-dispersive direction.

a side window on the door of the large scattering chamber. Figure 3.6 shows a typical beam spot at the target position as projected onto the ZnO coated viewer and captured by a low-intensity light camera. The target ladder is tall enough to hold two 5 cm tall targets in a frame. Figure 3.7 defines the coordinates at the target and shows the target frame to scale.

The target foils were attached to the aluminum frame with Scotch tape adhesive. Charge-exchange reactions on the hydrogen and carbon in the tape are visible in the data. These events are removed primarily with vetoes in the reconstructed parameter y_{ta}, the position on target in the dispersive direction, and the reconstructed target nucleus excitation energy. The Q-value for $(t,^3\mathrm{He})$ on hydrogen (-0.76 MeV) is such

Target	Thickness	Width × Height	Isotopic Enrichment	Vendor
CD_2	9.0 mg/cm^2	2.0 cm × 5.0 cm	nat. C	Icon Isotopes
^{24}Mg	9.86 mg/cm^2	1.27 cm × 5.08 cm	99.92%	ORNL
^{63}Cu	9.94 mg/cm^2	1.27 cm × 5.08 cm	99.86%	ORNL
^{94}Mo	10.03 mg/cm^2	1.27 cm × 5.08 cm	91.59%	ORNL

Table 3.1: Target foil specifications. For each target, columns indicate target thickness (or aerial density) in mg per cm^2; target foil width and height in cm; isotopic enrichment for each target nuclide, where the natural enrichment of ^{12}C is 98.89%; and the vendor that provided each target, where ORNL is Oak Ridge National Laboratory.

that the outgoing ^{3}He energy is substantially different than that for the same reaction on either ^{12}C ($Q_{g.s.}$= -13.350 MeV) or ^{24}Mg ($Q_{g.s.}$= -5.497 MeV). Since any charge exchange on carbon in the ^{24}Mg data will appear at $E_x(^{24}\text{Na}) \geq$ 7.85 MeV, which is above the excitation energies included in the analysis of ^{24}Na, subtraction of charge exchange on carbon is not necessary here[21].

With increasing target thickness, the overall experimental energy resolution goes down due to two effects. First, energy is lost by charged beams in the target material in discrete (not continuous) processes, e.g. in discrete transfers of energy to electrons in the target material. This phenomenon is commonly referred to as straggling, which increases with target thickness and projectile nuclear charge [88]. Second, the rate of energy loss of a particle travelling through the target depends on the charge of the particle, which doubles within the target at an unknown depth as shown in Fig. 3.8. Energy losses of tritons in the target foils are substantially lower than for ^{3}He, as shown in Table 3.2. This large relative difference in energy loss for the two species is

[21]In principle, other target nuclei with less convenient Q values may require background subtraction to remove charge exchange on carbon or other contaminants. This subtraction is a simple procedure if targets of the contaminants are available.

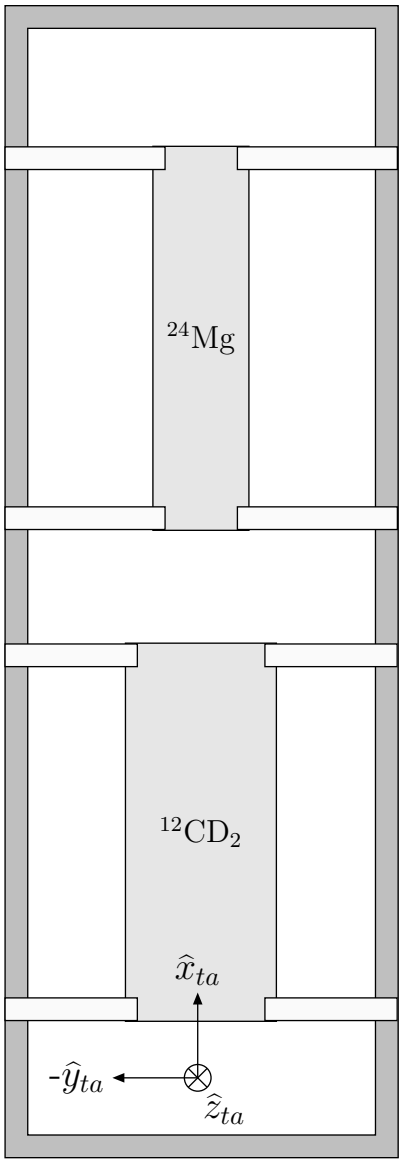

Coordinates

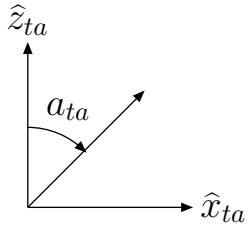

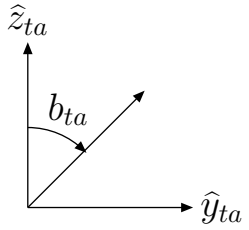

$$\tan\Theta_{\text{scatt}} = \sqrt{\tan^2 a_{ta} + \tan^2 b_{ta}}$$

Figure 3.7: Target Ladder Schematic and Coordinate System: actual size, as seen by incoming triton beam traveling along $\widehat{z}_{ta}$. The scattering angle Θ_{scatt} is calculated from the reconstructed angles in the dispersive direction a_{ta} and the non-dispersive direction b_{ta}.

Target Material	^{3}H loss [keV]	^{3}He loss [keV]	Diff. [keV]
^{12}C (10mg/cm^2)	58	247	189
^{24}Mg (9.86mg/cm^2)	53	210	157
^{63}Cu (9.94mg/cm^2)	44	180	136
^{93}Mo (10.03mg/cm^2)	41	165	124

Table 3.2: Projectile/ejectile energy loss in targets in units of keV.

the single largest contributor to the uncertainty in the reconstructed excitation energy of the target final state. Because the reaction position in z along the path of the beam is distributed statistically within the target and because of significant straggling as compared to the intrinsic S800 energy resolution, the overall energy resolution due to target thickness is approximately 175 keV[22]. When combined with the intrinsic energy resolution of the S800 spectrometer (including the position resolution of the ^{3}He in the focal plane detector), the overall energy resolution of the final state of ^{24}Na is 200 keV FWHM.

Estimations of angular straggling using LISE++ are approximately 0.3 mrad, smaller than the angular resolution at the target as reconstructed from focal plane data.

3.3 Measuring the ^{3}He: S800 Spectrometer

The first measurement of the outgoing ^{3}He nuclei from the charge-exchange reaction is in the S800 focal plane suite of detectors, which follow a series of magnets. The scattering angle and energy at the target are reconstructed with the position, angle

[22]Targets 10 mg/cm^2 thick made of material of higher mass A have fewer target nuclei, resulting in slightly smaller uncertainties due to the difference in energy straggling for the tritons and ^{3}He.

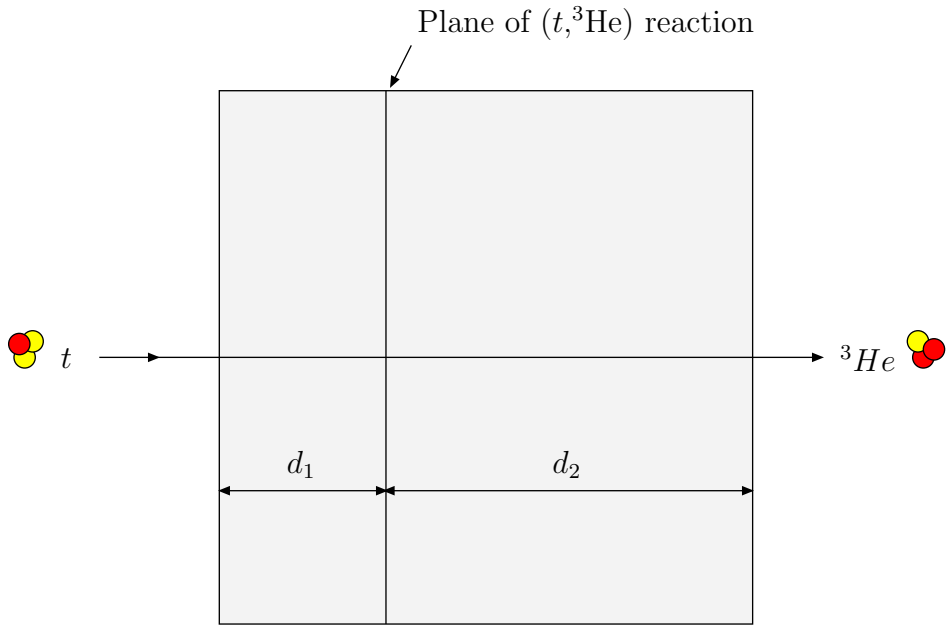

Figure 3.8: Beam straggling and loss of energy resolution in target foils. See text for details.

and energy in the focal plane. This section describes both the focal plane detectors and event reconstruction. See Refs. [6] and [89] for details on the S800 spectrometer and the focal plane detector suite, respectively.

3.3.1 Dispersion Matching Mode

The inherent energy resolution of the S800 spectrometer in dispersion matching mode for an infinitely thin target is roughly 35 keV for beam energies of 345 MeV, or one part in 10,000. In this mode, the analysis line is chromatic and the spectrograph is achromatic, meaning that the momentum spread of the beam at the object is cancelled at the focal plane, eliminating the need for tracking incoming particles and consequently achieving the highest momentum resolution. The energy in the focal

Energy resolution (intrinsic)	1 part in 10,000	30 keV
Energy acceptance	10%	30 MeV
Dispersion	$11cm/\%$	
Momentum acceptenace	0.5%	
Solid angle acceptance	$\Delta\Theta$=10° (175 mrad)	
	$\Delta\Phi$=7° (120 mrad)	
	Ω=20 msr	

Table 3.3: Parameters for the S800 magnetic spectrometer

plane corresponds to the *change* in the projectile's energy in the target without regard to the spread in initial momentum. Note that the initial momentum has a spread of $\pm 0.25\%$, which is large for intermediate reaction energy experiments.

The alternative is to run in focus mode, whereby the analysis line is achromatic and the image in the focal plane is chromatic. While one advantage in this mode is the larger momentum acceptance ($\pm 2\%$ vs $\pm 0.25\%$) which allows for a higher incident projectile intensity, the energy resolution is 24 MeV for a 345 MeV triton beam, far worse than even the (n, p) energy resolution. Focus mode is not an option, regardless of target thickness.

3.3.2 Focal Plane Detector Suite

The focal plane detector suite of the S800 shown in Fig. 3.9 consists of two parallel Cathode Readout Drift Chambers (CRDC) that measure projectile position and angle over an active area of approximately 60 cm by 30 cm, an ion chamber (not used in the present experiment), and three plastic scintillator bars (E1, E2, and E3), each with a Photo-Multiplier Tube (PMT) on each end used for particle identification (PID).

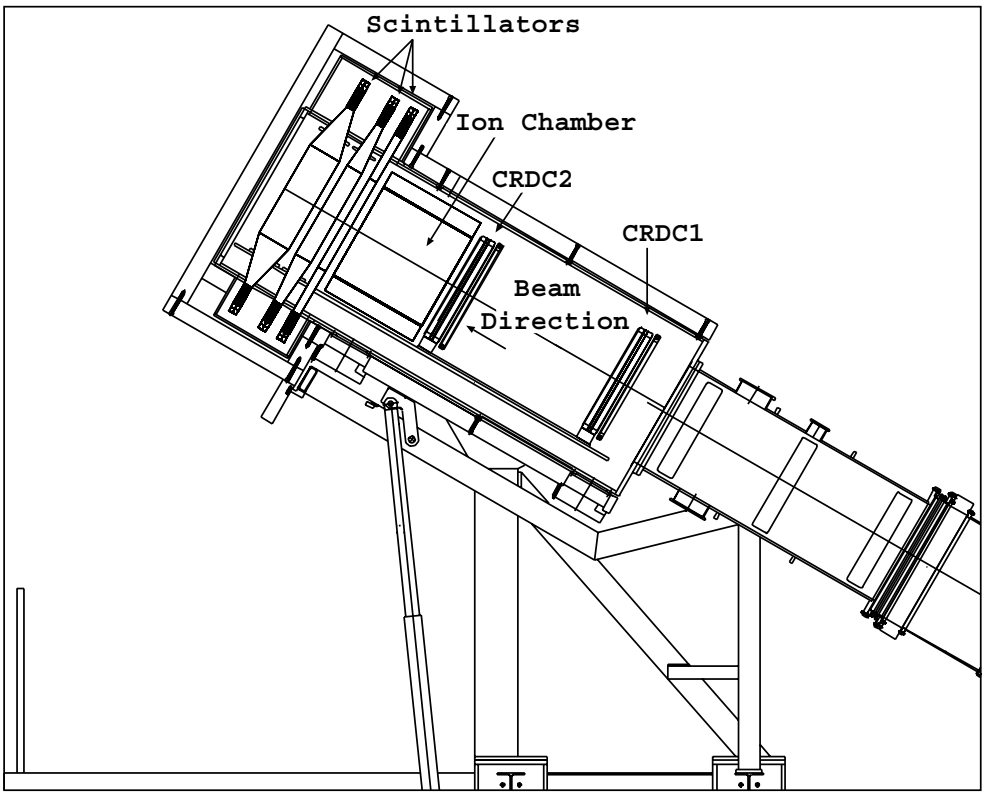

Figure 3.9: S800 Focal Plane Detector Suite [89].

The first scintillator, which is 3 mm thick, acts as the rear window of the unused ion chamber, the trigger for the data acquisition, and the stop for the time-of-flight (TOF) signal. The second and third scintillators are 5 cm and 10 cm thick, respectively. The third scintillator is largely unused in the present analysis due to a defect in the plastic from radiation damage. The scintillators serve to measure energy loss or total energy of (fully stripped) nuclei to identify the atomic number Z.

Each CRDC is filled with a mixture of 80% CF_4 and 20% isobutane (iC_4H_{10}). Charged particles traveling through a CRDC ionize the gas mixture. The y-position is calculated from the drift time. Charge collecting on the anode wire induces image

charges on a series of 236 cathode pads. The charge distribution generally spreads out over as much as 2 cm, while the ^{3}He x-position must be known to better than 0.5 mm for the desired energy resolution. The x-position along the anode wire is calculated by fitting the cathode pad signal distribution to a standard three-parameter function using signals from 7 to 9 good cathode pads. Incomplete calibration of the pad signal response[23] (see second item in section 3.3.5) does not significantly impact energy or angular resolution in Monte Carlo simulations[24]. Missing calibration data is managed with gain matching from a previous experiment and consistency checks against (t,^{3}He) reaction data.

The S800 CRDC are protected against abuse such as particle rates above 5 kHz in the focal plane. With a typical intensity on target of 10^6 tritons/second and the low cross section for an isospin flip, the maximum rate of ^{3}He in the focal plane is only about 30 Hz, well below the limit. At the NSCL, (t,^{3}He) experiments are rate-limited only by the NSCL Coupled Cyclotron Facility's capacity for primary beam intensity and not by detector constraints.

3.3.3 CRDC Calibration

To calibrate the signals for the y-position in the CRDC, two metal plates (hereafter, the CRDC masks) with a series of holes with known positions are inserted 8 cm directly upstream from a detector. Figure 3.10 shows the center portion of the CRDC

[23]Before experiments, the CRDC are calibrated in part by stepping an active α source across the detector to calibrate individual pad response. Cathode pads ($\leq$3%) with dramatically different responses to ^{3}He data are not used in fits.

[24]Events that straddle two neighboring modules of 16 cathod pads have a slightly higher risk of a small systemmatic deviation in reconstructed energy.

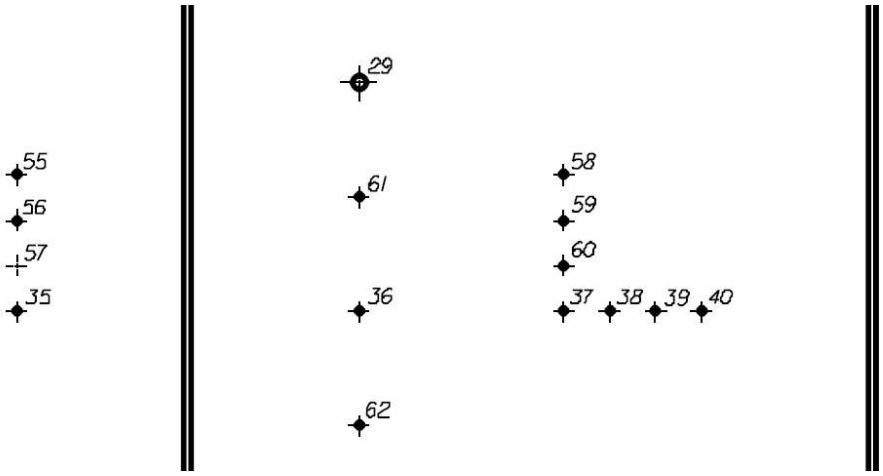

Figure 3.10: CRDC mask, center region. This portion of the mask includes two of five slits and 16 of 64 holes.

mask, including 2 of the 5 vertical slits for calibration of the x-position and 15 of the 64 holes with diameters up to 3 mm.

The ^{3}He particles that travel through the holes are separated in the PID as a result of the substantial energy loss suffered by those particles that otherwise travel through the thick metal. The path of each particle identified as passing through the mask holes is traced 8 cm back upstream (toward the target) to the mask. The centroids of the holes and slits are used to calibrate the parameters for translating CRDC signal to positions in the dispersive and non-dispersive directions.

Since the ^{3}He trajectory is traced 8 cm back to the mask using a preliminary calibration of both detectors, the calibration for any one CRDC depends on the calibration of the other. The calibration of each detector is then improved by tracing the ^{3}He path with updated parameters from the previous iteration until the parameters

stablize, which usually happens in a few iterations. This recursive method is more fully described in Ref. [21].

There are two sets of mask calibration data taken for the entirety of the 9 day experiment. For the experiment runs on the CD_2 and ^{24}Mg targets before the replacement of CRDC1, there is only one mask calibration run. While the calibration for the x-position is quite stable, the y-position calibration is highly sensitive to changes in the CRDC gas. Small deviations in the y-position in the focal plane most directly alter the calculation of the scattering angle at the target. To improve the resolution between mask calibrations and to correct for transient drifting in the y-position, relative run-by-run corrections (to the variables used in the calculation of detector position) are made based on the relative changes in position of the charge state spot on CRDC1. (See, e.g., Fig. 3.14.) The charge state spot walks over a range of approximately 10 cm in the vertical position for the present data and over a range of 45 cm for the data not included in this work.

3.3.4 Event Reconstruction at Target

Positions, angles and energies of the ^3He leaving the target are not measured directly. Instead, these parameters are reconstructed from the particle's parameters in the S800 focal plane as generally described in Ref. [6]. The magnetic fields and fringe fields for given magnetic settings (namely the electric current in two quadrupole and two dipole electromagnets) are calculated as described in Ref. [6]. With these fields, the code COSY Infinity Version 8.1 (Ref. [8]) calculates the non-dispersive position y_{ta}, the angles in the dispersive and non-dispersive directions a_{ta} and b_{ta}, and the relative deviation δ_{ta} of the energy from the spectrometer central ray. Each

reconstructed parameter is a sum of (Taylor expansion) terms up to 5th order in the focal plane parameters x_{fp}, y_{fp}, a_{fp} and b_{fp}.

$$\text{Parameter}_{target} = \sum_{i+j+k+l\leq 5} C(i,j,k,l) \cdot x_{fp}^{i} \cdot a_{fp}^{j} \cdot y_{fp}^{k} \cdot b_{fp}^{l}, \tag{3.3}$$

where parameter$_{target}$ is one of y_{ta}, a_{ta}, b_{ta} or δ_{ta} and C(i,j,k,l) are the coefficients calculated in COSY Infinity (see Appendix A). These parameters at the target are corrected to remove certain correlations as described in section 3.4.

From the scattering angle projections on the x_{ta} and y_{ta} axes, the laboratory scattering angle Θ_{scatt} is given by $\tan(\Theta_{scatt}) = (tan^2(a_{ta}) + tan^2(b_{ta}))^{1/2}$. The laboratory angles are converted to the center of momentum frame with a factor described in Eq. 4.4.

3.3.5 Unexpected Complications

There were several unexpected snags in the configuration for this experiment. Each is described here, and the prescribed solutions and estimated contribution to uncertainties are discussed in detail in Chapter 4.

• Time-of-flight data are missing for approximately 40% of the events due to an electronics error that is not correlated to event timing or any other parameter. Since particle identification and background subtraction are best done with the TOF, background for this 40% of the data is removed *statistically* (not on an event-by-event basis) by scaling data for which TOF is available. (See section 4.2 for prescribed method of subtraction.) This electronics problem has since been fixed and is not present in the subsequent (t,^{3}He) experiments (NSCL Experiment 05504 on ^{64}Zn and ^{93}Nb) in December 2005 and (NSCL Experiment 06032 on ^{150}Sm) in January 2008.

• The first CRDC (and most important position detector) in the focal plane imploded in an accident after the replacement of gas cylinders halfway through the experiment in the middle of the ^{63}Cu data runs. The replacement CRDC1 was faulty in a large region in the negative dispersive direction. For the bending dipole magnetic fields (Bρ=2.3100 T·m) used in the first half of the experiment, ^{3}He from charge-exchange reactions to low-lying excited states in the ^{63}Ni [from ^{63}Cu(t,^{3}He)] did not register on CRDC1. Consequently, the magnetic fields in the dipoles were increased (to Bρ=2.35643 T·m), shifting the ^{3}He particles to sample more positive positions in the dispersive direction. Since half of the CD_2 data was taken at the end of the experiment, only the ^{63}Cu and ^{12}C data are taken at more than one magnetic setting in the spectrometer. Due to the reduced angular acceptance, the ^{12}C data from the second half of the experiment are not presented here.

• Ground settling in the S3 vault altered the optics of several magnets through the Spring of 2005. After observing unusual distributions and correlations in reconstructed parameters (e.g. y_{ta}, b_{ta} vs y_{ta}) in the present data, the physical positions of landmarks were measured, first on the analysis line before the target and later on the spectrometer. The observed shifts of these landmarks have two major consequences. First, the axis of the analysis line shifted in the non-dispersive direction relative to the axis of the spectrometer by almost 1 cm. This has the potential to reduce the acceptance of the spectrometer, reduce the transmission of the beam from the object box to the pivot point of the S800, and lead to optical aberrations. Second, the (unrelated) shift of the focal plane detector suite in the non-dispersive direction and slight translations and rotations in the spectrometer magnets are not accounted for in the standard NSCL supported COSY Infinity calculation of inverse maps. New

maps with altered parameters (distances between the target and spectrometer doublet magnets and between the focal plane and the second dipole, and shifted y_{fp} positions) are used instead. The new map optimizes energy and angular resolution and correlations for reconstructed parameters of the ^{3}He at the target. Tables of the inverse map parameters for the S800 spectrometer and discussions of the alterations to the COSY input file and the reconstruction are in Appendix A and Section 3.3.4, respectively.

• Finally, the high intensity primary beam exposed some minor flaws in vault configurations. The unusually high primary beam intensity generated such high levels of neutron radiation that solid-state relays began to change positions independently of facility operations. During the experiment, slits in the beamline between the cyclotrons spontaneously closed on several ocassions, essentially stopping the experiment briefly. As a result of this work, several pieces of hardware were later relocated for smoother operation with all high intensity beams at the NSCL. This experiment also served as a development exercise for more efficient tuning and stability in high intensity primary beams. Whereas this experiment underwent primary tunes on a daily basis or more often, subsequent experiments with high intensity ^{16}O primary beams have already enjoyed superior stability, sometimes not requiring any major tuning of the primary beam over the course of a week.

3.4 Calibration of Reconstruction and Optimization

The inverse map for transforming positions and angles in the S800 focal plane to position, angles and energy at the target is slightly modified to improve energy resolution and uncertainties in the phase space of the outgoing ^{3}He. Before corrections

to the inverse map, the correlation between angle and position in the non-dispersive direction, for example, and resolution of the target image do not match the physical orientation of the target ladder and target size. The alterations to the event reconstruction and the underlying justification for these changes are described here.

3.4.1 Modifications to Inverse Map Calculations

The reconstruction of the outgoing ^{3}He is optimized by moving the target and focal plane (fp) position inputs in COSY inverse map calculations to improve energy and angular resolution of individual states in the data and to resolve the reconstructed phase space occupied by both the target material and the hydrocarbon support material. One primary objective is to rotate the relation between position in the non-dispersive direction and the angle b_{ta}. This working assumption is supported by the good agreement between MOCADI[25] [75] simulations and the data as observed in the focal plane of the S800. Specifically, the slope of the b_{fp} vs y_{fp} spectrum matches the MOCADI simulation that uses a shift in the focal plane position of approximately 7 cm upstream [49].

Figure 3.11 shows an unusual shadow of the reconstructed beam spot at the target. Panels b) and d) in particular show the position of the target material and supporting tape, respectively. The projection onto the y_{ta} axis clearly inflates the width of the target. In panel c) the two hydrogen marks from tape on the left and right side of the target are barely resolved. The resolution in y_{ta} is improved with successive shifts of the distance along the beam line between the target and first magnet in the spectrometer. (See Appendix A for more details.)

[25]MOCADI is a Monte Carlo simulation that calculates primary and fragment particle trajectories through ion optics and thin material. All MOCADI simulations used in this work were produced by Mr. G. Wes Hitt at the NSCL.

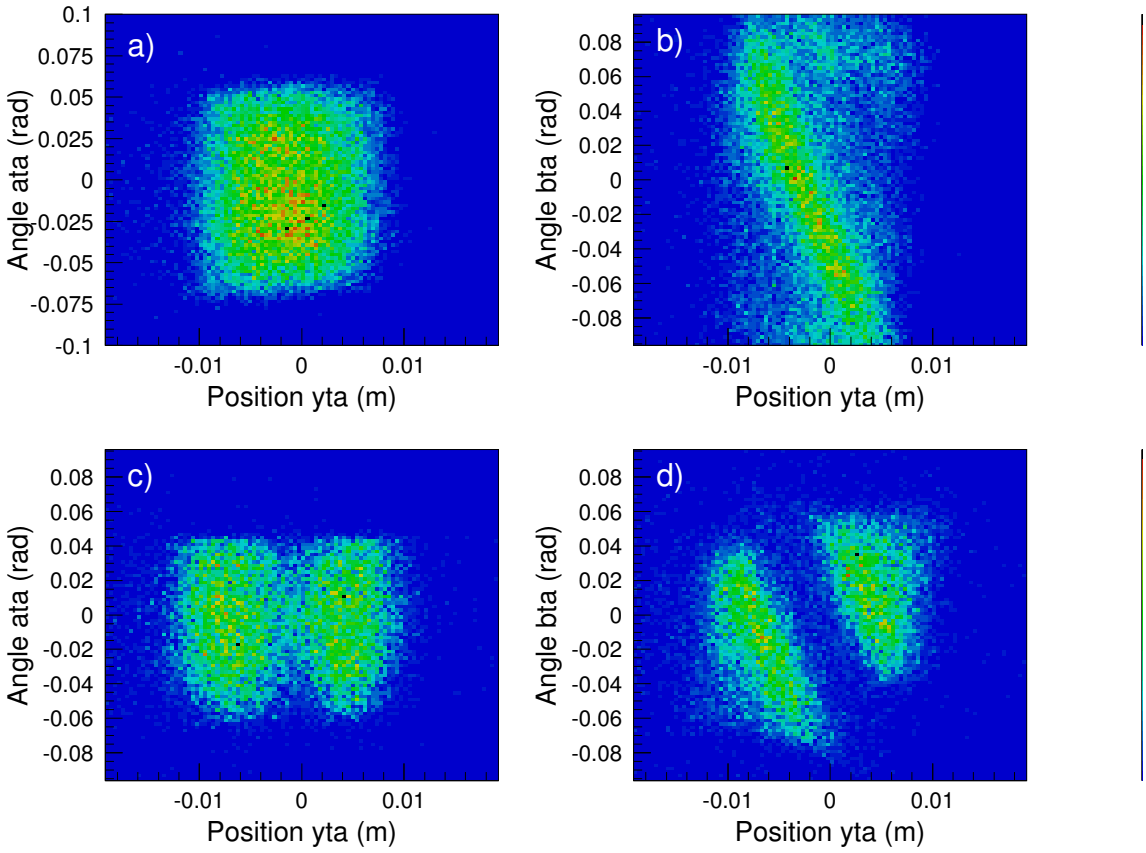

Figure 3.11: Reconstructed ^{3}He phase space on target using the default target position. The left (right) panels are the reconstructed angle in the dispersive (non-dispersive) direction a_{ta} (b_{ta}) vs. the reconstructed position in the non-dispersive direction y_{ta}. The upper (lower) two panels are gated on events that are charge exchange reactions on target (hydrogen) material. All angles are in radians, and the target position y_{ta} is in meters relative to the central beam axis.

The optimal reconstruction is shown in Fig. 3.12. Correlations between reconstructed scattering angle at the target and the reconstructed position y_{ta} in the non-dispersive direction on target are corrected in the inverse map calculations with a shift of the nominal pivot point by approximately 8.5 cm upstream. This second correction in the inverse map calculation is likely correcting for a combination of physical shifts in the target position and focus of the analysis line from the nominal positions. Furthermore, the subsequent CEX NSCL Experiment 05504 independently finds the same shifts in focal plane and target positions to within 1 cm. These corrections in the y_{ta} calculation are important in this particular data set for the purpose of background removal as discussed in Chapter 4.

The end result is that the energy resolution is refined as shown e. g. in Fig. 3.13 from 170 keV to 110 keV for the ^{4}Mg main 1^{+} state first 30 mrad in ^{3}He scattering angle. Figure 3.13 shows the progressive improvement in energy resolution as a result of these corrections to the inverse map calculation for events in the main peak with scattering angles 17 mrad $\leq \Theta_{scatt} \leq$ 28 mrad [26]. The shift in target position makes little change in the excitation spectra, aside from improved background removal due to the y_{ta} reconstruction.

3.4.2 Serendipity: The $^{3}He^{+}$ Charge State Contamination

Figure 3.14 is a typical spectrum of the ^{3}He ejectile positions y_{fp} vs x_{fp} in the focal plane detectors of the S800 magnetic spectrometer. The vertical straight lines are different exited states in the target nucleus; the main $J^{\pi} = 1^{+}$ state at 1.346 MeV

[26] Fig. 3.13 shows the progression of the energy resolution for the main peak in ^{24}Na to take advantage of large statistics; the second angular bin is used both for the statistics and for the relative improvement in angle, which in turn effects the reconstructed energy. This FWHM does not reflect the overall energy resolution.

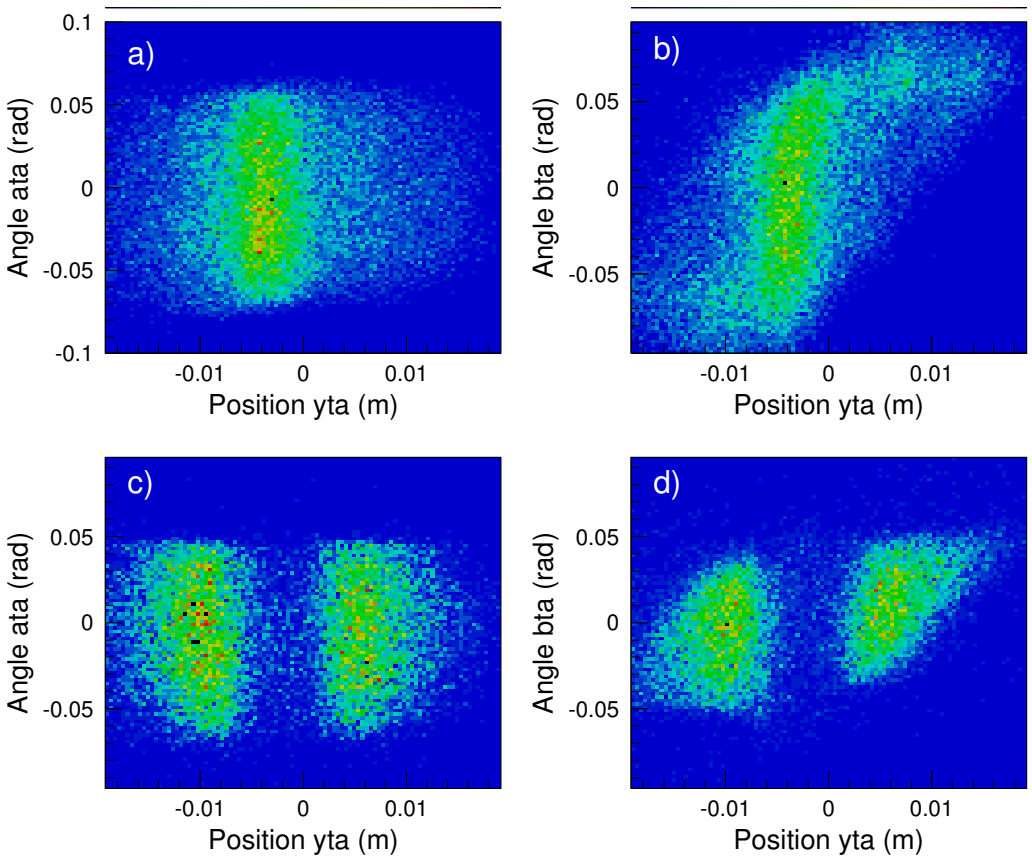

Figure 3.12: Optimally reconstructed ^{3}He phase space on target. Same as Fig. 3.11, with an 8.5 cm shift in the target position in the COSY input file. All angles are in radians, and the target position y_{ta} is in meters relative to the central beam axis.

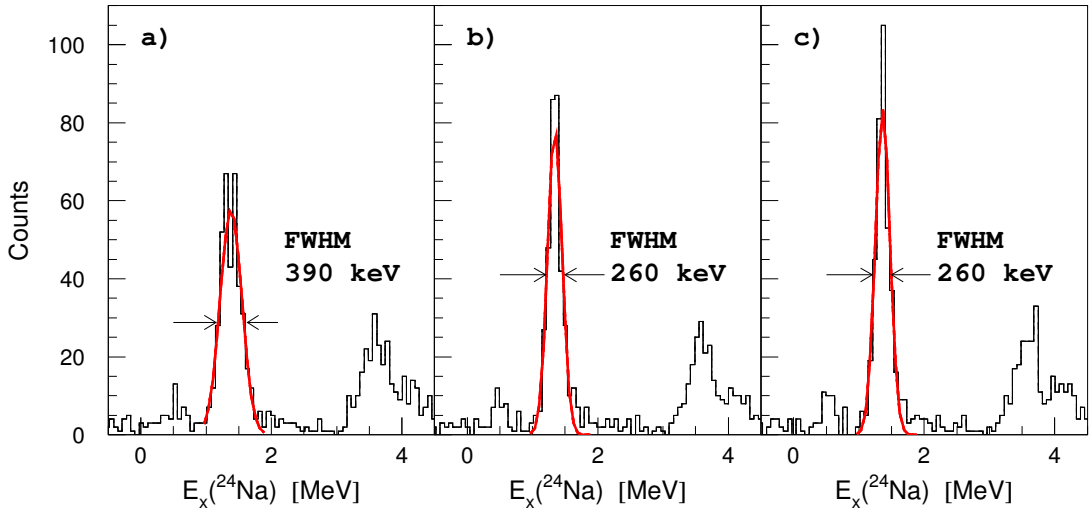

Figure 3.13: Reconstructed ^{24}Na energy spectra with three different inverse maps. The main peak is fit with a gaussian (red line) to estimate the energy resolution for relatively small scattering angles. a) Excitation energy spectrum reconstructed with (default) nominal focal plane and target positions. b) Same as a), with a shift in focal plane position along the beam axis. c) Same as b), with additional shift in target position along beam axis. See discussion in text.

above the ^{24}Na ground state is circled to aid the eye. As the projectile transfers more energy to the target nucleus, the ^{3}He ejectile has less momentum, placing it further to the right in the focal plane. The higher excited states in ^{24}Na appear as parallel, vertical lines to the right of the ground state. The double sideways parabolas are events from the tell-tale charge-exchange reactions on hydrogen, mostly coming from the tape on the edges of the targets. If all nuclei in the target plane have negative Q values for charge-exchange reactions, there should be no nuclear reactions to the left of the hydrogen in this figure.

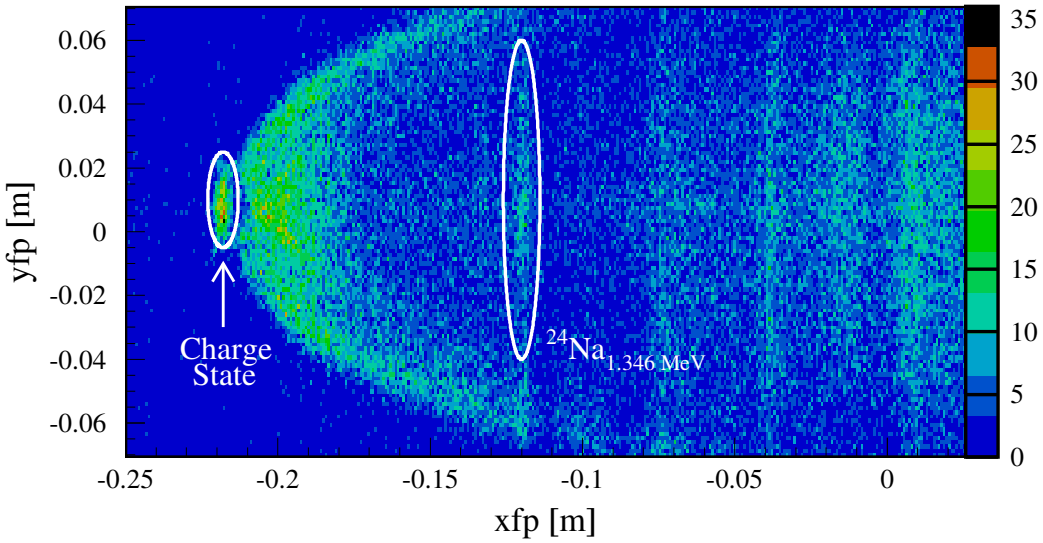

Figure 3.14: Charge state (^{3}He$^+$) spot in S800 focal plane detectors (color). The charge state spot (circled, left) in the y_{fp} position vs x_{fp} position is from the background (^{3}He$^+$,^{3}He^{++}) reaction, or electron stripping. The ^{24}Mg(t,^{3}He)^{24}Na$_{1.346\ MeV}$ reaction events are also circled (right). Excited states in the ^{24}Na are easily visible as parallel lines to the right of the ground state. The sideways double parabolas next to the charge state are from the H(t,^{3}He)n reaction on the adhesive on each side of the target.

The small localized feature to the left of the double hydrogen lines has nearly the same energy as the incident triton beam and occupies a small phase-space. Unlike previous (t,^{3}He) experiments at the NSCL, the current secondary triton beam has a very small ^{3}He$^+$ charge state contamination [27] that is fully stripped in the target material. The TOF of the charge state events indicate that the ^{3}He$^+$ particles are

[27] Though the charge state is a very small component of the cocktail beam, all charge state projectiles are stripped, whereas only tens of tritons for every million undergo a charge-exchange reaction. This substantial difference in cross sections accounts for the clear visibility of the charge state in the data. Note that this charge state would not be present in a primary triton beam.

not produced in the Be production target, but at some other unknown location in the beam line. These events, because of their low Q value, are in no way a background in the GT spectra. The (^{3}He$^+$,^{3}He^{++}) events do, however, give an unanticipated shadow of the secondary beam *incident* angle on the target in the non-dispersive direction, further reducing the uncertainty in relative scattering angle. Figure 3.15(b) shows the reconstructed angles for xthe (^{3}He$^+$,^{3}He^{++}) charge-state stripping in the ^{24}Mg target. The path of the charge state is not deflected significantly in the target. Figure 3.15(b) is fitted with a 6^{th} order polynomial to produce Fig. 3.15(c). Correcting the reconstruction of b_{ta} in this manner reduces the uncertainty in the overall scattering angle Θ_{scatt}.

The angle a_{ta} in the dispersive direction for the charge state does not have the same pronounced correlation with y_{ta}. Since the position x_{ta} in the dispersive direction cannot be reconstructed while operating in dispersion matching mode, the incident angle in a_{ta} is not corrected for correlations with x_{ta}. Even so, the a_{ta} distribution for the charge state events is no more broad than the b_{ta} distribution.

3.5 Calculated Angular Distributions

Though the magnetic spectrometer does a good job of selecting ^{3}He final state events and the energy of the incident triton beam favors the $V_{\sigma\tau}$ term in the potential, $J^\pi \neq 1^+$ transitions are indistinguishable in the focal plane detectors on an event-by-event basis from the desired $J^\pi = 1^+$ GT transitions. Different ΔL transitions are separated in the data by decomposing $d\sigma(\Theta_{scat})/d\Omega$ for slices in excitation energy into the ΔL=0, J$^\pi$=1$^+$ and other order transitions, giving priority to known J$^\pi$ states in the residual nucleus. This method, known as Multiple Decomposition Analysis (hereafter

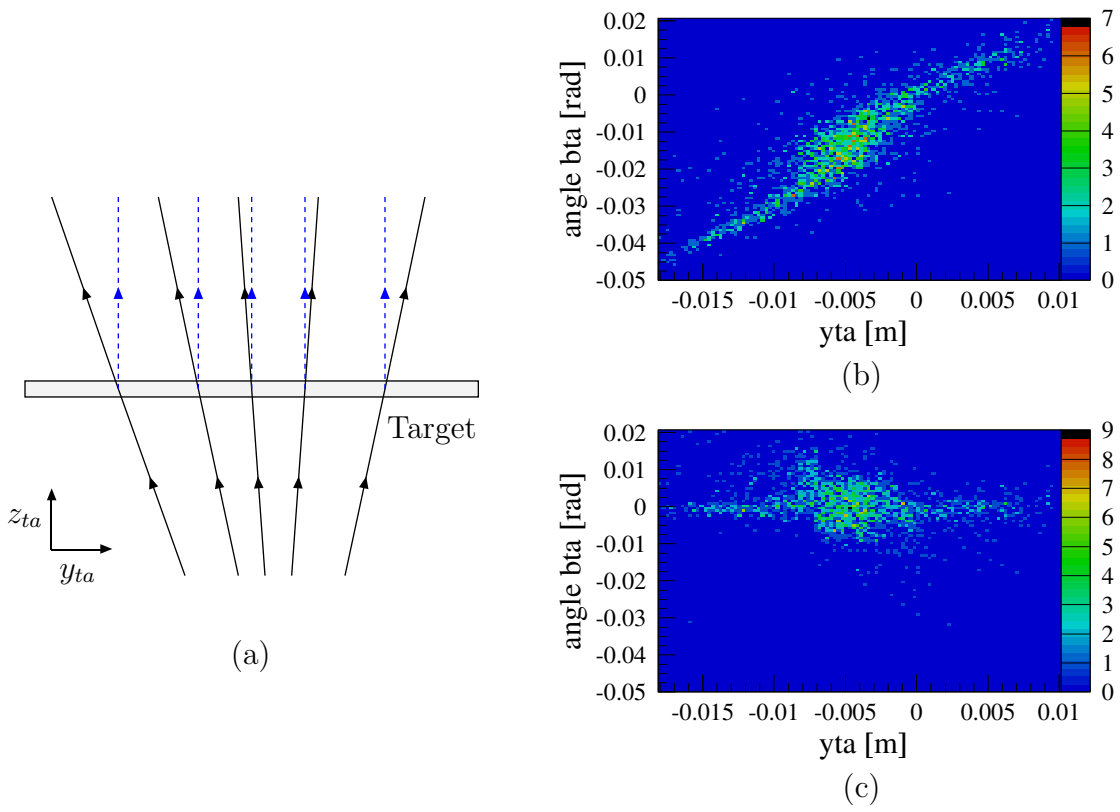

Figure 3.15: Corrections for incident beam angles. (a) Schematic of charge state reaction physical angles at target (solid) and angles after corrections (dashed). (b) Reconstructed physical incident angles b_{ta} vs. y_{ta} for charge state. (c) The same as b), after corrections for the incident angle.

MDA), is an established method of extrapolating the ΔL=0, ΔS=1 differential cross section to zero degrees in scattering angle. Due to limited statistics and the small angular range of the detector, decompositions here include at most 2-3 transitions.

Data in the (^{3}He,t) direction from RCNP cover a smaller angular range, precluding decomposition of the the $J^\pi=1^+$ states into the ΔL=0, ΔS=1 and the ΔL=2, ΔS=1 components. Both facilities, however, are capable of measuring differential cross

section at higher angles by way of rotating the spectrometer[28] , allowing for more extensive multipole decomposition analysis when required.

Angular distributions of cross section for given ΔL, J^+ transitions in the (t,^{3}He) reaction are calculated with the program FOLD [24]. DW81 is a Distorted Wave Born Approximation code that treats a nucleon in the incoming nucleus as a distorted wave. FOLD differs most importantly from other Distorted Wave Born Approximation codes such as DW81 in that it is double folding, treating both the projectile and the target as composite objects. (Tables of the FOLD output for each target are in Appendix B.)

Input for both codes include Optical Model Potentials (OMP) for both the incoming and outgoing channels. OMP for a given target energy are target/probe dependent. Ideally, (t,^{3}He) charge-exchange data should include (t,t') data to measure an OMP appropriate for the relevant triton beam energy. The S800 analysis line delivers 115 MeV tritons with a magnetic rigidity of Bρ = 4.8 T·m to the target. The S800 spectrometer line, however, is limited to Bρ of 4 T·m and thus cannot bend tritons (A/Q=3) with such high energy (and thus such high Bρ) into the focal plane. Instead, optical model parameters are taken from (^{3}He,^{3}He$'$) elastic scattering data at an energy of $E_{^3He}$=450 MeV in Ref. [87] and modified for the triton; the depths (radii and diffusenesses) are taken to be 0.85 (1.0) times that of ^{3}He [82]. (No (t,t') data are available at energies above 100 MeV/nucleon.)

[28]The primary reason that measurements are not taken over a broader ranger of scattering angles is that rotating the spectrometer (e.g. from 0° to 4° to double the scattering angle range) requires a substantial and impractical interruption in the experiment.

CHAPTER 4

DATA AND ANALYSIS

Chapter 4 presents event selection criteria, background removal, and the calculated differential cross sections for the ^{12}C(t,^{3}He)^{12}B and ^{24}Mg(t,^{3}He)^{24}Na charge-exchange reactions. The $\Delta L = 0$, $\Delta S = 1$ component of the measured differential cross sections are extracted to zero degrees in scattering angle, using empirically-based calculations of angular distributions.

The cross section for ^{12}C(t,^{3}He) to the ^{12}B ground state is compared to previous measurments and to complimentary ^{12}C(^{3}He,t)^{12}N data from RCNP in Japan [90]. Whereas this measurement of charge exchange using the (t,^{3}He) probe is the first at intermediate energies for the ^{24}Mg target, only the ^{24}Na B(GT) distribution is compared to other probes in the same direction, such as the (d,^{2}He) probe, and to complimentary ^{24}Mg(^{3}He,t)^{24}Na data from RCNP in Japan [90] in Chapter 5.

4.1 Particle Identification

The focal plane detectors (Fig. 3.9) identify the Z=2 ^{3}He particles with signals in the lower[29] PMT on scintillators 1 and 2. The relatively large change in the B·ρ setting

[29]The upper PMT data in scintillators 1 and 2 are not used to circumvent signal deterioration from scintillator damage.

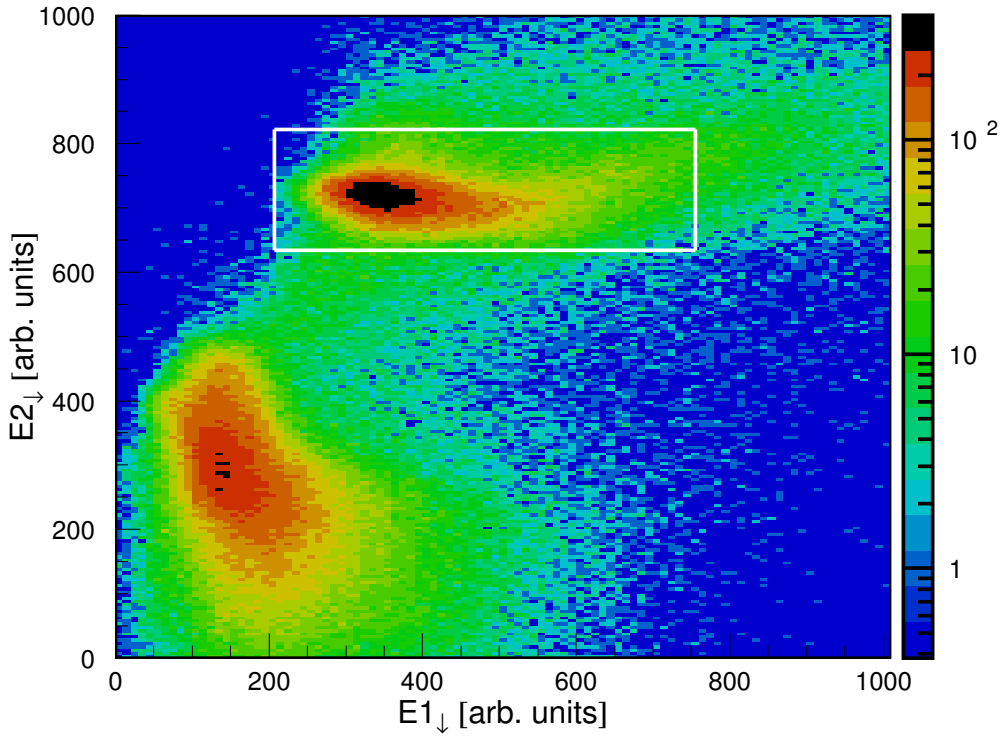

Figure 4.1: Typical particle identification spectrum: Lower PMT E_2 vs. PMT E_1 signals. The white box denotes the window for ^{3}He PID. (Note the log color scale.)

of the S800 spectrometer line as compared to the S800 analysis line (i.e. pre-target rigidity of 4.8 T·m vs. post-target rigidity of 2.31 T·m) accounts for the simplicity of the PID spectrum in the focal plane as shown in Fig. 4.1. (For a linear color scale, see Fig. 4.4(d).) Only events within the PID gate defined by the white box are included in the analysis. The efficiency for the scintillator PMT hardware is assumed (in a reasonable approximation) to be 100%, which is typical for the low count rate in the focal plane for this experiment.

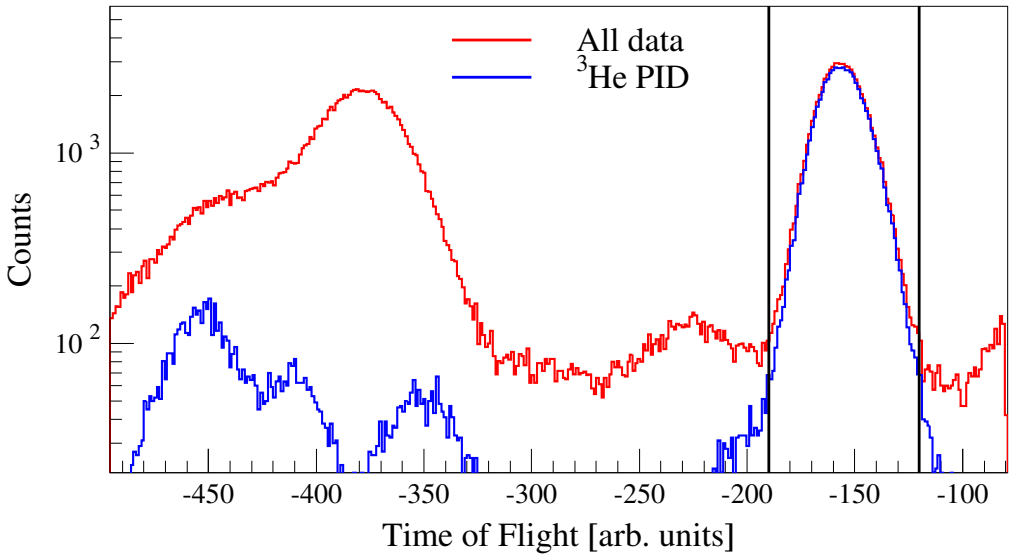

Figure 4.2: Time-of-Flight distribution. The red line is the TOF distribution for all events in the spectrometer focal plane. The blue line is the subset of these events that meet the PID criteria. Of the events in the CEX PID gate (blue line) where the particle in the focal plane is identified as ^{3}He, roughly 12% are background outside of the ^{3}He TOF window (vertical lines) and are not likely from (t,^{3}He) at the target. (Note the log scale on the vertical axis.)

4.2 The Good, the Bad, and the No TOF

Figure 4.2 shows a typical Time-of-Flight distribution for the charge-exchange data. Ideally, the TOF further distinguishes nuclei by the A/Z ratio. The upper red line is the distribution for all events[30]. The lower blue line is the subset of all events for which the scintillator data are within the PID window. The vertical black lines indicate the window of TOF values that correspond to an additional identification of ^{3}He in the focal plane. This window marks the "good" or ^{3}He-like TOF values. In the TOF (blue) spectrum gated on events within the CEX PID window, a 12%

[30]Events with no TOF information in the data stream appear as events with a TOF value of -10 000, beyond the range of Fig. 4.2.

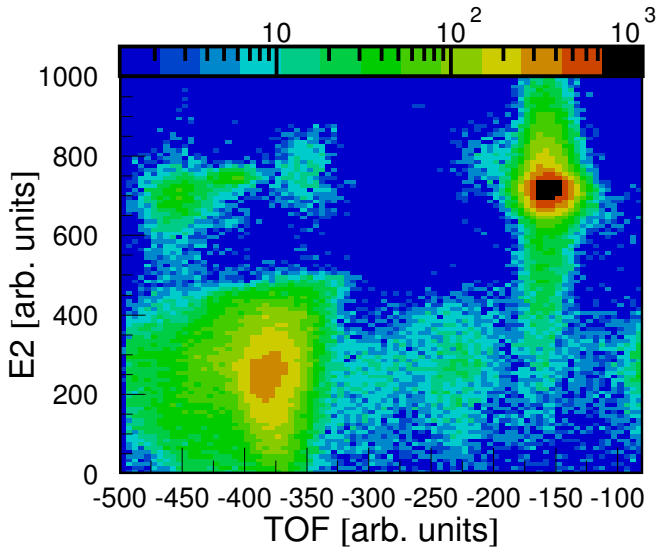

Figure 4.3: Scintillator E_2 PID signal vs time-of-flight. Events with no TOF data are not shown.

background remains in the CEX PID cut. The majority of these "bad" or background TOF values are from -500 to -300 (arbitrary units). This background is independent of target material. (Later experiments confirm this background actually comes from different components of the incident secondary beam such as ^{6}He and partially ionized $^3He^+$[90], both of which have the same A/Z ratio as the triton.)

Ideally, the ^{3}He particles from the (t,^{3}He) reaction are identified both from the energy (deposition) in the focal plane scintillators and from TOF data. Applying the additional constraint that the event TOF have values between -190 and -120 removes much of the remaining background on an event-by-event basis. Figure 4.3 shows a typical spetrum for scintilator signal vs. TOF. The the events to be removed from the no-TOF data are clearly visible in the upper left quadrant. Events for which the TOF is missing (see section 3.3.5)- approximately 40% of all charge-exchange data- retain

this small background that cannot be removed on an event-by-event basis. (Data for which the TOF is missing are hereafter denoted as "no-TOF.")

The two halves of the data are combined under the basic assumption that the no-TOF set is otherwise just like the other data with TOF information. No clear correlation between missing TOF and angle or excitation energy appears in the data to suggest otherwise. Figure 4.4 supports the claim that the events with no TOF are

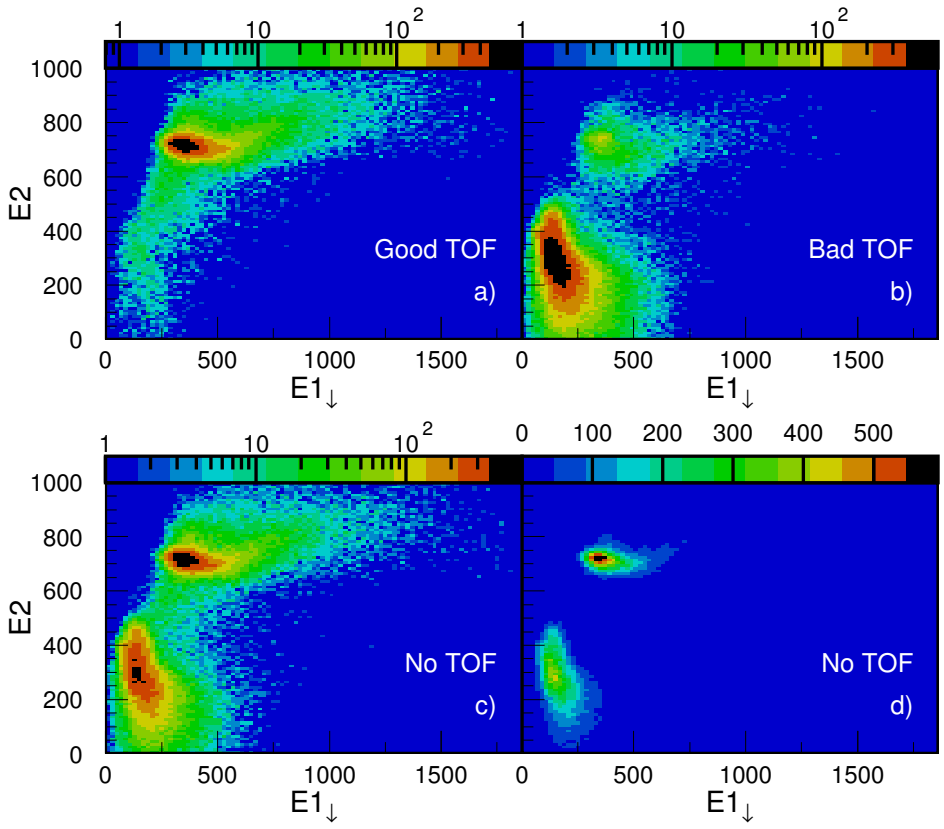

Figure 4.4: a) PID spectrum of E2 vs $E1_{\downarrow}$ for events with good TOF values. b) Same as a) for events with bad TOF values. c) PID spectrum for events with no TOF data. d)Same as c), with linear color scales. E2 is the corrected sum of the two PMT signals on scintillator E2, and $E1_{\downarrow}$ is the signal in the bottom PMT on scintillator E1.

linear combinations of good PID and bad PID spectra; adding the events with TOF information in the two upper panels gives the same structure as the no-TOF events in the lower panels.

In Fig. 4.5 the angular distribution for relative counts of events with good TOF (lower left panel) and with no TOF (lower right panel) in the ^{12}B ground state agree within the drawn statistical error bars. The same holds true for the main peak in ^{24}Na at 1.346 MeV, as shown in Fig. 4.6. In both figures, the lower left panel shows the absolute number of events with good ^{3}He TOF values as a function of scattering angle in the laboratory frame. The lower right panel shows the same for events for which there are no TOF data. (The target's reconstructed excitation energy for the events selected in the two lower panels are highlighted in blue in the upper panel energy spectra.)

After statistically subtracting the expected number of no-TOF events which would have TOF values outside the good TOF window in each angular bin for a given excitation energy, the angular distributions of data without TOF are in agreement to within error bars with the angular distributions for the events with TOF data.

To remove the background from the no-TOF events in the differential cross-section spectra, the no-TOF energy spectra for each angular region are decomposed into two parts, the distribution of the bad TOF events and the distribution of the good TOF events. The charge exchange on hydrogen, such as that shown in Fig. 4.6(a), is a strong and broad feature in the energy spectrum of events with bad TOF values. This undesired feature telegraphs the relative fraction of bad TOF events within the no-TOF set with small uncertainty, despite the low statistics for bad TOF events for

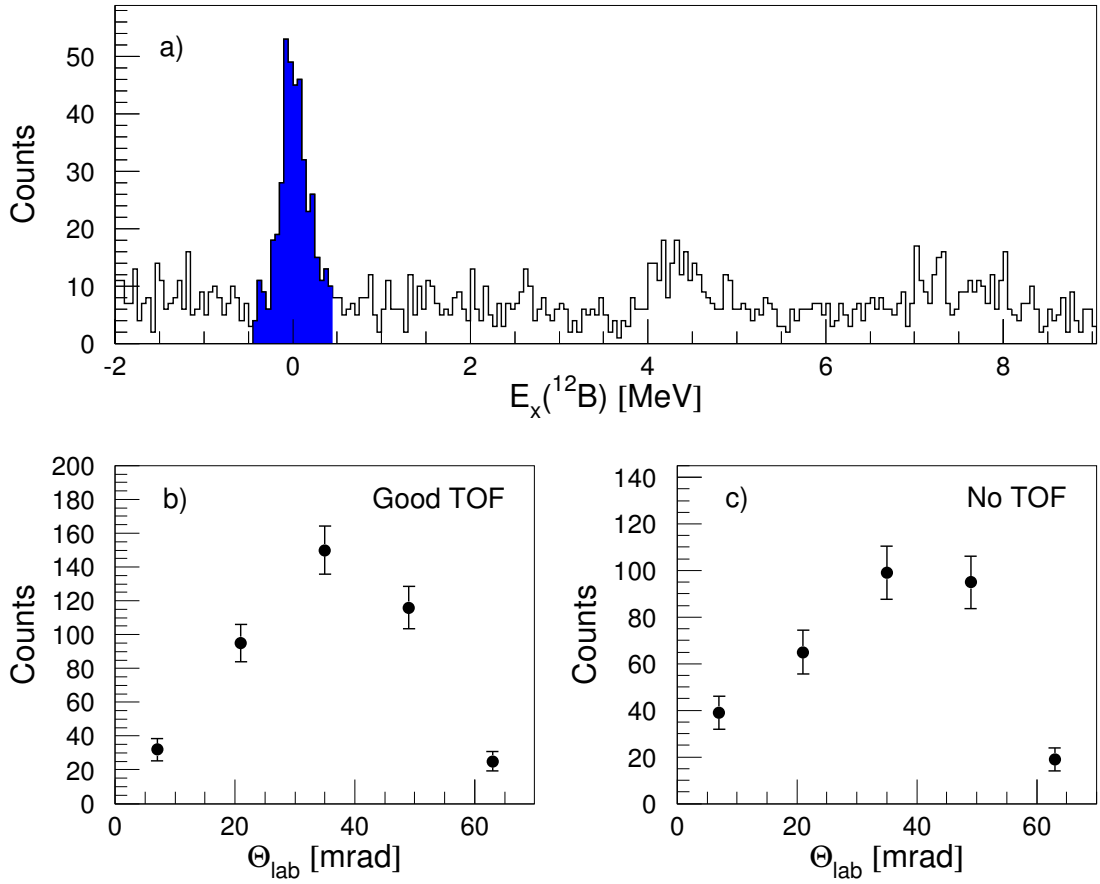

Figure 4.5: a) Energy excitation for (t,^{3}He) events on the CD_2 target with good particle PID, both with good TOF and no TOF. b) Angular distribution (in lab frame) for events in the (blue) ^{12}B ground state in panel a) with good TOF values and good energy PID. c) Same as b), for events with no TOF data.

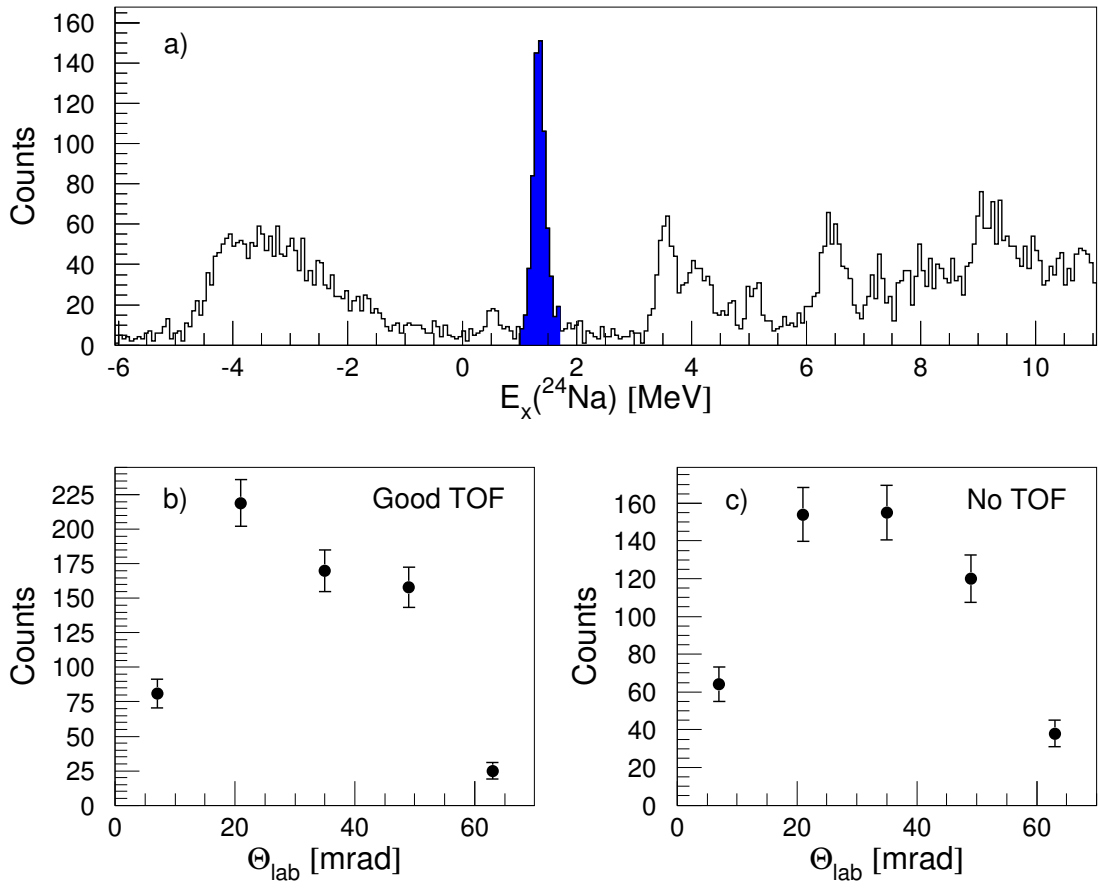

Figure 4.6: a) Energy excitation for $(t,^3\mathrm{He})$ events on the ^{24}Mg target with good particle PID, both with good TOF and no TOF. Charge exchange on hydrogen appears as a broad peak near -4 MeV. b) Angular distribution (in lab frame) for events in the (blue) ^{24}Na 1.346 MeV state in panel a) with good TOF values and good energy PID. c) Same as b), for events with no TOF data.

$E_x \geq 0$. Likewise, the pronounced main GT peaks in ^{12}B and ^{24}Na are strong and sharp features in the energy spectrum of events with good TOF values.

For each angular bin, the entire energy spectrum of no-TOF events is decomposed into two components, the good TOF distribution and the bad TOF distribution, calculated from the events with TOF information. Since the subtraction cannot be done on an event-by-event basis, the *relative statistical fraction* of events with no TOF data that would have had TOF values outside the ^{3}He values drawn in Fig. 4.2, were they available, is estimated based on the TOF distributions for events within the ^{3}He PID window. The relative fraction of the background in the no TOF events is then subtracted from the combined energy spectra and from the angular distributions for each peak (or region) in excitation energy. Unless otherwise indicated, all following spectra include both the good TOF events and the no-TOF events for which background is subtracted statistically, as described above.

4.3 Cross Sections

With the statistics available, the scattering angles are divided into 5 bins of 14 mrad in the laboratory frame for a total of 70 mrad ($\sim 4^\circ$) in scattering angle. (In the center-of-mass frame, 70 mrad of Θ_{scatt} is 87 mrad or 5.2° for the magnesium target and 115 mrad or 6.6° for the carbon target.) The solid angle Ω_i in the laboratory frame for scattering angles in 14 mrad bins is

$$\Omega_i = \int_{\phi=0}^{2\pi} \int_{\theta=\theta_i}^{\theta_i+0.014rad} sin(\theta) d\theta d\phi. \tag{4.1}$$

For example, the two forwardmost solid angles Ω_0 for scattering angles of 0-14 mrad and Ω_1 for scattering angles of 14-28 mrad are

$$\Omega_0 = 2\pi \int_{\theta=0}^{0.014\ rad} sin(\theta) d\theta = 0.0006157\ sr \tag{4.2}$$

$$\Omega_1 = 2\pi \int_{\theta=0.014\ rad}^{0.028\ rad} sin(\theta) d\theta = 0.0018471\ sr = 3.00\ \Omega_0. \tag{4.3}$$

In the case of the two outermost angular bins, the limits of integration are further constrained to reflect the angular acceptance of the S800 spectrometer, excluding angles for which b_{ta}, $a_{ta} \geq 50$ mrad in the laboratory frame. The laboratory opening solid angles and scattering angle range for the five angular bins are listed in Table 4.1.

For each opening angle Ω_i, the differential cross section $d\sigma/d\Omega_{c.m.}$ is

$$\frac{d\sigma(\Theta_i)}{d\Omega_{c.m.}} = \frac{1}{(f_{rel.})^2 \Omega_i} \cdot \frac{N_{^3He}}{n_{target} N_{triton}}, \tag{4.4}$$

where $N_{^3He}$ is the number of ^{3}He particles in the focal plane attributed to the charge-exchange reaction for a given number of incident tritons $N_{tritons}$ on n_{target} number of target nuclei per unit area, and where f_{rel} is the transformation factor for scaling angles in laboratory frame to the relative angles in the center-of-mass frame. $N_{^3He}$ is further adjusted for the relative fraction of events that are excluded through, e.g., cuts in y_{ta} that are imposed to reduce background from reactions on the tape. These factors are discussed with the respective cross-section calculations. The transformation factor f_{rel}^2 is $(1.283)^2$ for the ^{12}C target data set and $(1.14)^2$ for the ^{24}Mg target data set.

The (zero degree) cross sections are cited with the statistical error (e.g. from fitting angular distributions with 5 angular bins and extrapolating to zero degrees with a given number of events) and do not include the systematic error due to uncertainty in the overall normalization of the triton beam intensity. For the ^{12}C(t,^{3}He)^{12}B data, the (zero degree) cross section is cited with two uncertainties, the first being the statistical error (e.g. from fitting angular distributions with 5 angular bins and extrapolating to zero degrees with a given number of events) and the second being the systematic error due to uncertainty in the overall normalization of the triton beam intensity.

i	Θ_{scatt} Range [mrad]	Ω_i [sr]	Ω_i/Ω_0
0	[0,14)	0.0006157	1.000
1	[14,28)	0.0018471	3.000
2	[28,42)	0.0030781	5.000
3	[42,56)	0.0034959	5.678
4	[56,70)	0.0009637	1.535

Table 4.1: Laboratory scattering angle ranges and opening angles. For data, all event count and cross-section angular distributions are divided into five angular bins. For each bin, the range for Θ_{scatt} indicates the limits for the laboratory angles in constructing all angular distribution spectra. The effective opening angles Ω_i for each scattering angle range exclude reconstructed scattering angles outside of the S800 acceptance, which is readily apparent in the last two bins.

The single largest contribution to the systematic uncertainty for cross sections come from a 15% (25%) error in the incident number of tritons on the carbon (magnesium) target[31]. For the ^{24}Mg(t,^{3}He)^{24}Na data, the cross sections include only the statistical uncertainty. The systematic (normalization) error in the cross sections for the ^{24}Mg target is handled only at the stage of extracting Gamow-Teller strengths by way of scaling the unit cross section: see section 5.1.

4.4 ^{12}C(t,^{3}He)^{12}B(1^+) Cross Section

The present work includes a subset of the total time-integrated beam luminosity taken on the $^{12}CD_2$ target during the experiment. All data taken after the replacement of the damaged CRDC1 in the spectrometer focal plane are excluded here[32].

[31]See section 4.5.1 for discussion of uncertainty of incident number of tritons on the smaller magnesium target.

[32]The later data set has superior statistics but troubling systematic uncertainties and reduced angular acceptance resulting both directly and indirectly from faulty or damaged hardware in the

The present data includes 1.77×10^{10} tritons on the $^{12}CD_2$ target. Due to the limited statistics, only the main GT state, namely the ground state in ^{12}B, is discussed here. The next two known $J^\pi = 1^+$ (GT) states are at 5.0 MeV and 6.6 MeV, which are not discernable in the spectra. (See the excitation energy distribution in the upper panel of Figure 4.5.) With the highest stable ^{16}O primary beam intensities currently available, the NSCL is capable of producing as many tritons in a few hours of beam time, making this target an excellent candidate as the cross-section calibration target[33] for the charge-exchange program.

Reorganizing Equation 4.4, the differential cross section for the ^{12}C(t,^{3}He)^{12}B reaction becomes

$$\begin{aligned}
\frac{d\sigma(\Theta_i \in \Omega_i)}{d\Omega_{c.m.}} &= \frac{N_{^3He}(\Theta_i)}{(\Omega_i/\Omega_0)} \cdot \frac{1}{(f_{rel})^2\Omega_0} \cdot \frac{1}{N_{triton}} \cdot \frac{1}{n_{target}} \qquad (4.5) \\
&= \frac{N_{^3He}(\Theta_i)}{(\Omega_i/\Omega_0)} \cdot \frac{1}{(1.283)^2(0.0006157sr)} \cdot \frac{1}{(0.90 \times 1.77 \times 10^{10})} \\
&\quad \times \frac{12 \times 10^3 g/mole}{(0.9889 \cdot 6\frac{g}{cm^2} \cdot 6.022 \times 10^{23}/mole)} \cdot 10^{27}\frac{mb}{cm^2} \\
&= (0.208\, mb/sr/^3He)\frac{N_{^3He}(\Theta_i)}{(\Omega_i/\Omega_0)}, \qquad (4.6)
\end{aligned}$$

where the number of incident tritons N_{triton} includes scaling factor of 90% to account for the cut in the parameter y_{ta}, which removes possible background from charge-exchange reactions on carbon in the tape at the expense of 10% of the incident triton beam. See panels b) and d) in Figure 3.12.

replacement CRDC. See section 3.3.5. The data from the 7.52×10^{10} tritons on target in the later half of the experiment may have value beyond the scope of this work.

[33]A cross-section calibration target serves to integrate a collection of cross-section data from multiple experiments into one set for which the relative cross sections are consistent, despite possible variation in systematic errors in the absolulte cross section. Since the precision of the relative cross section is more refined than the precision of the absolute cross sections, such a cohesive data set provides a better assessment of the reliability of theoretical calculations.

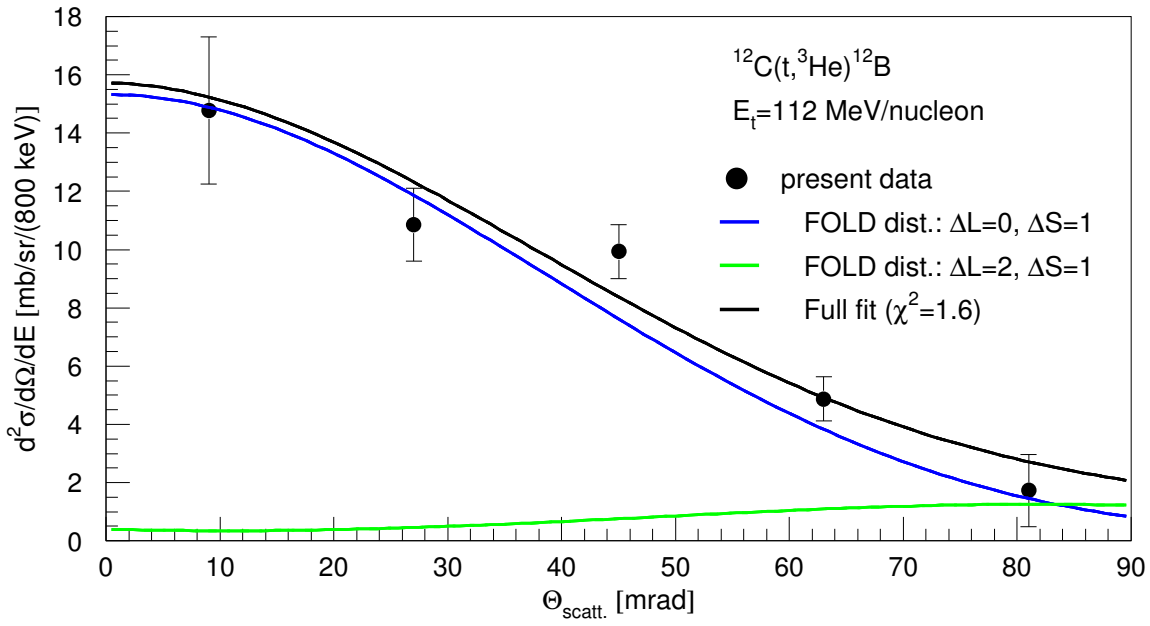

Figure 4.7: The ^{12}C(t,^{3}He)^{12}B(1^+) reaction differential cross section as a function of center-of-mass scattering angle. The blue (green) line is the calculated angular distribution for the ΔL=0 ΔS=1 (ΔL=2 ΔS=1) term, scaled to fit the data. The black line is the sum of the two components. Error bars do not include systematic uncertainty. See text.

Figure 4.7 is the differential cross section for the ^{12}B ground state fitted with the FOLD calculated angular distribution. The experimental differential cross section is decomposed with two free parameters into the two ($\Delta L = 0$ and $\Delta L = 2$) angular distributions for the $J^\pi = 1^+$ transition to the ground state as calculated with FOLD. The unscaled angular distributions for the two separate components are shown in Fig. 4.8[34]. The black line is the FOLD calculated differential cross section, scaled to fit the experimental distribution.

[34]Table B.1 in Appendix B lists FOLD output for both the ΔL=0 and the ΔL=2 components of the J$^\pi$=1$^+$ transition in 0.2° increments. As the FOLD output is discrete, the two FOLD angular distributions are fit with a seventh order polynomial, both for the purpose of fitting the data with two functions and for visualization in Figure 4.7.

The χ^2 of the overall fit is 1.6 per degree of freedom, giving a scaling factor of 0.64 ± 0.06 for the predicted ΔL=0 (GT) component and 0.8 ± 0.6 for the non-GT component. Combined with the fact that the nearest known state is a $J^\pi = 2^+$ state at 0.953 MeV, the fit does not suggest other J^π components should be included.

The zero degree differential cross section of the ΔL=0 component is 15.4±1.4±1.5 mb/sr, where the first component in the uncertainty is due to the fit of the angular distribution and the second component is a nominal 10% uncertainty in the triton beam normalization. The zero degree differential cross section of the ΔL=2 component is 0.4±0.3 mb/sr, where both the fit error and uncertainty in the triton beam normalization are included. For this level of statistics, any error in extracting the B(GT) for this state from the ΔL = 2, ΔS = 1 contributions to the ΔJ = 1 GT excitation are overwhelmed by the uncertainties for the ΔL=0 state.

Three ^{12}C(t,^{3}He)^{12}B(1^+, g.s.) measurements, all taken at the NSCL in a 10 year time span, though with different primary beams, triton energies, and angular resolution, have somewhat inconsistent results. The two previous measurements by Daito [25] and Cole [23] use α primary beams to produce 127 MeV/nucleon and 140 MeV/nucleon triton beams, respectively. Additionally, the Daito data have significantly poorer angular resolution; as the ^{12}C(t,^{3}He)^{12}B(1^+, g.s.) reaction differential cross section falls off by a factor of 2 comfortably within a center-of-mass scattering angle of 3°, the 11.8±1.4 mb/sr cross section for very small angles in the Daito data may be consistent with the current result. Reference [25], however, does not document the angular range over which the cross section is 11.8±1.4 mb/sr, owing to the limited tracking capability of the detector configuration, which pre-dates construction of the S800. This comparison serves as an excellent example for why naive comparisons of

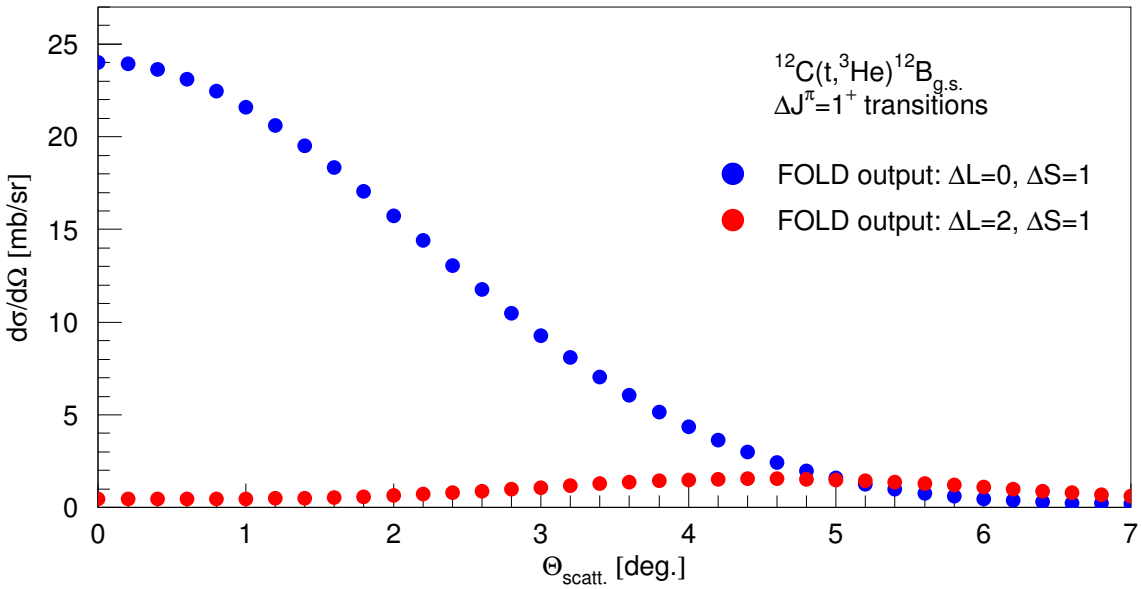

Figure 4.8: FOLD angular distributions calculated for the ΔL=0 (blue) and the ΔL=2 (red) components of the $J^{\pi}=1^{+}$ transition for the ^{12}C(t,^{3}He)^{12}B$_{g.s.}$ reaction.

different data (even among experiments taken at the same institution) are difficult without either careful extrapolation to zero degrees scattering angle or explicit documentation of the angles over which the forward cross section is measured. The Cole data cites the differential cross section in the same manner as the present work, but the overall normalization, and consequently the extrapolated zero degree differential cross section, differs significantly from the present work. For a triton energy of 140 MeV/A, Cole et al. report a zero degree differential cross section of 22±3 mb/sr, approximately 2 standard deviations higher[35].

[35]The interpretation of the Cole data is complicated by the fact that none of the experimentalists who took the data participated actively in the analysis in Ref. [23]. The calibration of the Cole triton beam uses the count rate of a ^{3}He secondary beam from the fragment separator piloted to the S800 focal plane, which requires assumptions about the transmission of both the ^{3}He and ^{3}H beams. Since active detection of the incoming tritons is not in the data stream, any error underestimating

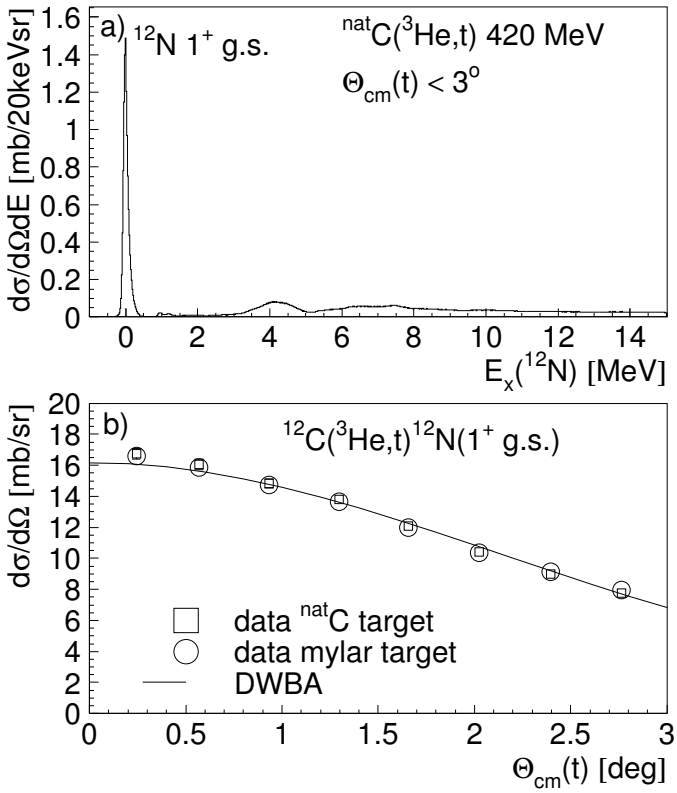

Figure 4.9: ^{12}C(^{3}He,t)^{12}N reaction cross section data from RCNP [90]. Upper panel a) shows the observed energy distribution for the ^{12}N final state. Lower panel b) is the ^{12}N 1$^+$ ground state differential cross section as a function of scattering angle.

Future experiments will do well to improve triton number normalization, placing the extraction of B(GT) for other targets on more solid ground, and to clearly document the angular range of the charge-exchange data (which was difficult to do with the Daito data), allowing for other groups to easily make simple comparisons.

the total number of tritons on target (by way of misinterpreting experiment documentation logs) would handily account for discrepancies between the Cole data and the present data.

Figure 4.9 shows the excitation energy spectrum and the differential cross section for the complimentary ^{12}C(^{3}He,t)^{12}N reaction [90]. The calibrated RCNP experimental differential cross section[36] extrapolated to zero degrees is 16.1±0.1±1.6 mb/sr with an incident ^{3}He energy of $E_{^3He}$ = 420 MeV, which is slightly higher than the NSCL triton energy. Correcting for the difference in reaction energy and isospin symmetry breaking, the present data should have a zero degree cross section of approximately 16 mb/sr. On this count, the present work is consistent with that of Ref. [92].

4.5 The ^{24}Mg(t,^{3}He)^{24}Na Reaction

The Q-value for the (t,^{3}He) charge-exchange reaction to the ^{24}Na ground state is -5.5 MeV. By virtue of the fact that Q=-13.4 MeV for charge exchange on ^{12}C, the first 7 MeV of the ^{24}Na data is free of ^{12}B background from the target supports.

Charge exchange on ^{24}Mg in the (n,p) direction has also been recently studied with the (d,^{2}He) probe at KVI in The Netherlands at energies of 85 MeV/nucleon by Rakers et al. [68, 69].

4.5.1 Correction of incident triton beam intensity

Figure 4.10 shows the systematic difference in the distribution of tritons in the y_{ta} direction on the target. The most probable source for the more narrow triton distribution on the ^{24}Mg target is the difference in target width. Because of the difference in target widths, the incident number of tritons on the ^{24}Mg target per unit of current on the Faraday bar is reduced to account for the slightly different distribution of tritons in y_{ta}.

[36] All RCNP data cross sections on the various targets across a number of experiments are scaled so that the ^{26}Mg(^{3}He,t)^{26}Al cross section is consistent with a single, previous measurement.

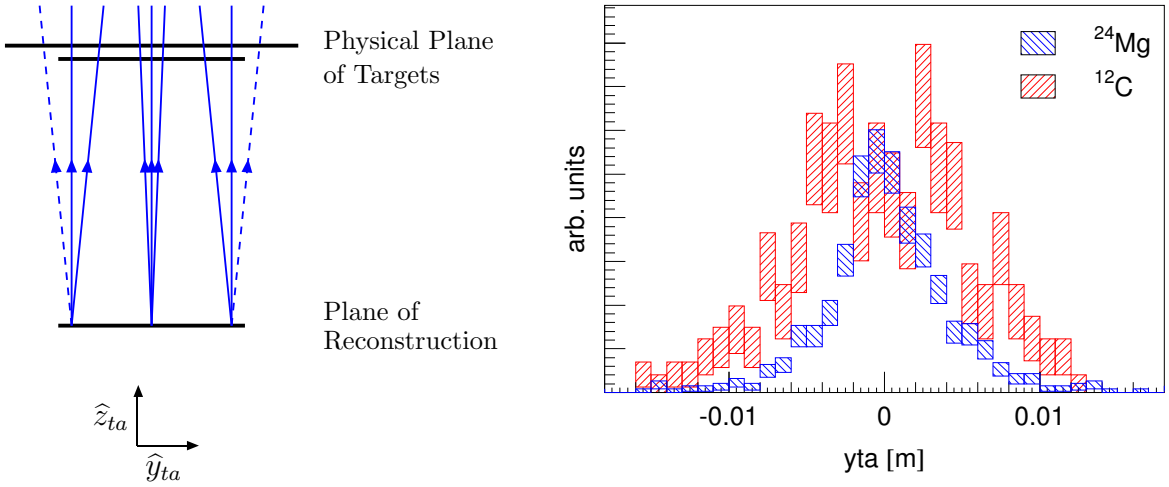

(a) (b)

Figure 4.10: a) Schematic for incident reconstruction relative to physical targets. In the plane of the physical targets, the two lines represent the relative width of the CD_2 and ^{24}Mg targets. Dashed triton paths pass through the wider CD_2 target but not the ^{24}Mg target. b) Distributions in y_{ta} for CD_2 and ^{24}Mg targets. The distributions are normalized to make the central distributions consistent for the two targets.

The position in y_{ta} for tritons on the target is reconstructed in a slightly different plane along the z-axis than the physical position of the target, which is why the distributions in Fig. 4.10 (b) do not have sharp edges reflecting the width of the target. To estimate the number of tritons that are missing within the 8 mm wide y_{ta} cut for the ^{24}Mg target, the y_{ta} distributions for the two targets are normalized so that the incident triton distribution near $y_{ta} = 0$ is the same for both the ^{12}C and ^{24}Mg targets. The "missing" triton intensity, drawn as the dashed triton paths in Fig. 4.10 (a), is then the relative difference between the two experimental distributions integrated over $y_{ta} = \pm 4$ mm.

Within the 8 mm cut for the ^{24}Mg target width, approximately 31% of the incident triton intensity misses the target. The normalization of the distributions and the

two integrated sums of tritons with the $|y_{ta}|\leq 4$ mm are limited by the experimental statistics and the precision with which the position y_{ta} is reconstructed. The incident number of tritons on target is scaled by a factor of 69%, but could be as low as 50% or as high as 80%. With this additional source of uncertainty in the incident triton number N_{triton} and the slight correlation between y_{ta} and scattering angle (see e.g. Fig. 3.11), the statistical error bars in all following differential cross-section spectra are correspondingly increased by 20%. (Though the incident triton primarily effects the overall normalization, the correlation between y_{ta} and Θ creates a small higher order systematic error that is dependent on angle.)

4.5.2 ^{24}Mg(**t**,^{3}He)^{24}Na Cross Section

Reorganizing Equation 4.4 in the same manner as Eq. 4.5, the differential cross section for the ^{24}Mg(t,^{3}He)^{24}Na reaction becomes

$$\begin{aligned}
\frac{d\sigma(\Theta_i \in \Omega_i)}{d\Omega_{c.m.}} &= \frac{N_{^3He}(\Theta_i)}{(\Omega_i/\Omega_0)} \cdot \frac{1}{(f_{rel})^2\Omega_0} \cdot \frac{1}{N_{triton}} \cdot \frac{1}{n_{target}} \qquad (4.7)\\
&= \frac{N_{^3He}(\Theta_i)}{(\Omega_i/\Omega_0)} \cdot \frac{1}{(1.14)^2(0.0006157sr)} \cdot \frac{1}{(2.39\times 10^{11})} \\
&\quad \times \frac{24\times 10^3 g/mole}{(0.9992\cdot 9.86\frac{g}{cm^2}\cdot 6.022\times 10^{23}/mole)} \cdot 10^{27}\frac{mb}{cm^2} \\
&= (0.038\, mb/sr/^3He)\frac{N_{^3He}(\Theta_i)}{(\Omega_i/\Omega_0)}, \qquad (4.8)
\end{aligned}$$

where the number of incident tritons N_{triton} includes scaling factors of 87% to account for the triton beam purity, 64% to account for the more narrow ^{24}Mg target (see section 4.5.1), and 69% to account for the cut in the parameter y_{ta}.

The experimental cross sections at $\Theta_{scat.} = 0^\circ$ for the various excitation energy regions are summarized in Table 4.2. Once the zero degree cross sections are extracted, the GT cross sections are extrapolated to $q = 0$ with the ratio $\sigma(q = 0)/\sigma(\Theta = 0^\circ)$

^{24}Na State	$\frac{d\sigma(Q,\theta=0)}{d\Omega}_{exp.}$	$\frac{d\sigma(Q,\theta=0)}{d\Omega}_{exp.}$	$\frac{\sigma(q=0)}{\sigma(Q)}_{FOLD}$	$\frac{d\sigma(q=0)}{d\Omega}_{exp.}$
E_x [MeV]	Total [mb/sr]	GT only [mb/sr]		[mb/sr]
0.472	0.76(13)	0.69(10)	1.08	0.75(10)
1.346	5.60(22)	5.30(21)	1.11	5.86(23)
3.14-3.94	3.69(23)	3.23(19)	1.17	3.78(23)
6.5-7.1	1.30(18)	1.22(16)	1.29	1.57(20)

Table 4.2: ^{24}Mg(t,^{3}He)^{24}Na cross section data. For each of the four energy regions, the total and GT cross sections are extracted to zero degrees scattering angle. $\sigma(q = 0)/\sigma(Q)$ is the multiplicative factor calculated with FOLD used to extrapolate cross sections to zero momentum transfer, $d\sigma(q = 0)/d\Omega_{exp}$.

as calculated in the DWBA code FOLD. Since some neighboring 1^+ peaks cannot be resolved with the experimental energy resolution, the method of combining multiple peaks and the extraction of the differential cross section are discussed individually here below.

Peak 1: 0.47 MeV

Figure 4.11 shows the reconstructed energy and angular distributions of the first 1^+ peak in ^{24}Na at 0.47 MeV. The first 1 MeV of the known ^{24}Na structure is relatively sparce[31], with only two states of similar energy that are not fully resolved, as is the energy spectrum. For each angular range, the background for this peak is assumed to be a flat distribution in energy, estimated with the events just outside the peak's energy range. Panel (c) in Fig. 4.11 shows the number of events in excess of this small background. Dividing each data point in this figure by the relative opening

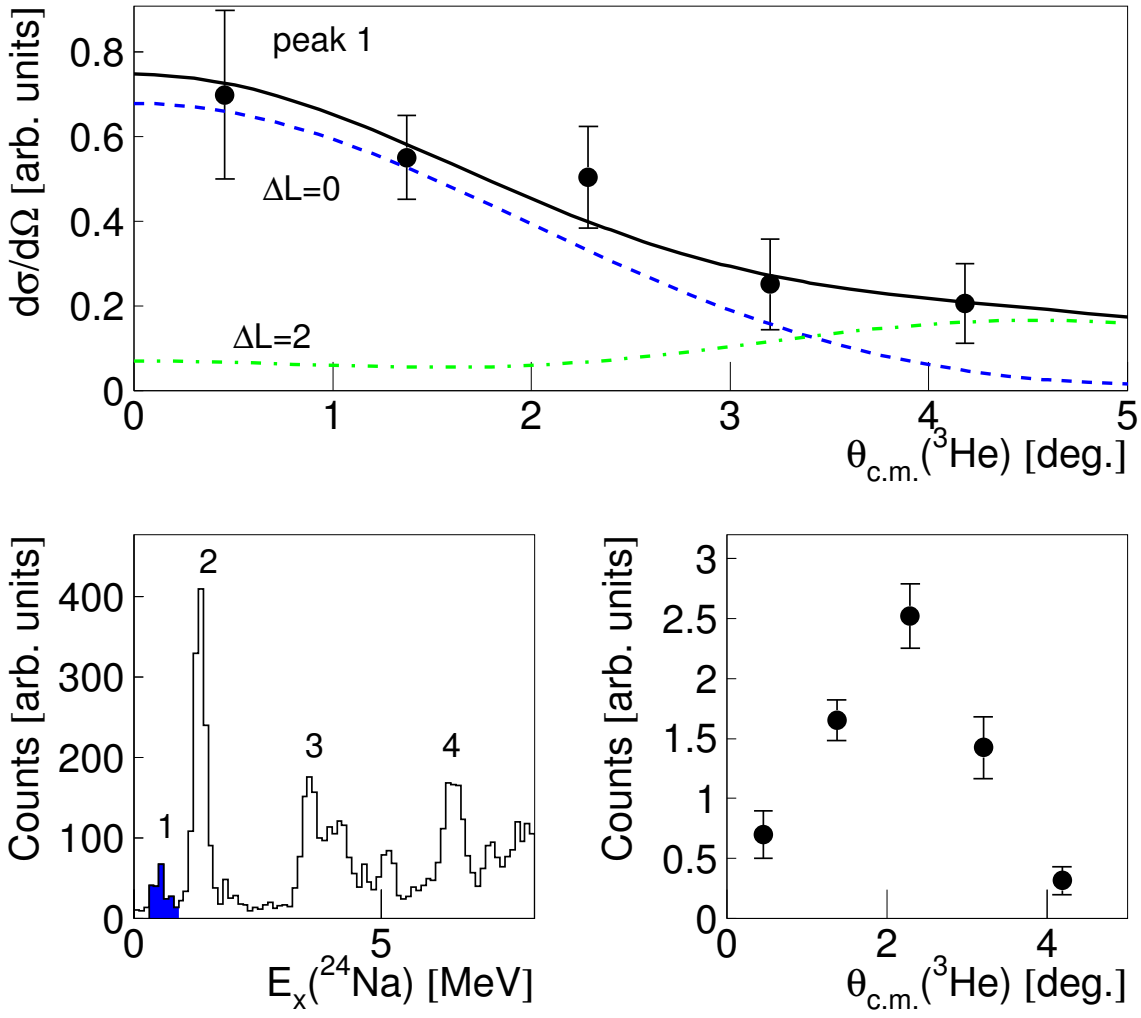

Figure 4.11: ^{24}Mg(t,^{3}He)^{24}Na(1^+, E_x=0.47 MeV) reaction differential cross section as a function of center-of-mass angle. a) The differential cross section ($Q_{exp.}$) is decomposed into the FOLD distributions for the two components in the $\Delta J = 1^+$ transition: the $\Delta L = 0$, $\Delta S = 1$ term (blue), and the $\Delta L = 2$, $\Delta S = 1$ term (green). The sum of the two components is shown in black. The location of the peak in the energy spectrum is highlighted in blue in panel b). The distribution of measured ^{3}He counts in excess of background is shown in panel c). (All error bars are statistical.)

angle and multiplying by the factor in Eq. 4.6 gives the differential cross section, shown in Fig. 4.11 a).

The experimental zero degree differential cross section for the GT transition is extracted by decomposing the angular distribution into the two $\Delta J^\pi = 1^+$ contributions, the $\Delta L = 0$, $\Delta S = 1$ term and the $\Delta L = 2$, $\Delta S = 1$ term. The angular distributions for both components are calculated as described in section 2.6 and are listed in Table B.1. The least-squares fit gives a scaling factor of 0.245±0.034 for the GT term and (3.9 ± 1.7) for the quadrupole $\Delta L = 2, \Delta S = 1$ term. Extrapolating the GT component to zero degrees gives $d\sigma/d\Omega$= 0.69±0.09 mb/sr for this peak. (For all ^{24}Na states, the statistical uncertainties in extrapolated zero degree cross sections and associated B(GT) are based on the uncertainty from the MDA. See Table 5.1.)

Peak 2: 1.37 MeV

Several states lie within the energy limits for peak 2, including $J^\pi = 1^+$, 2^+, and 5^+. Since the angular distributions for excitations of 2^+ and 3^+ states are quite similar [92] and the choice of which angular distribution to use, besides the GT component, does not significantly affect the error in $\hat{\sigma}(\Theta = 0°)$ beyond statistical uncertainties, only the ΔL=0 and ΔL=2 distributions are used the MDA for peak 2. The least-squares fit of the total angular distribution gives a scaling factor of 0.28±0.01 for the GT term and (0.9 ± 0.1) for the $\Delta L = 2, \Delta S = 1$ term. Extracting the GT component to zero degrees gives $d\sigma/d\Omega$= 5.3±0.2 mb/sr for this peak. Because of the nearby 2+ state at 563 keV, this may be a slight over-estimation.

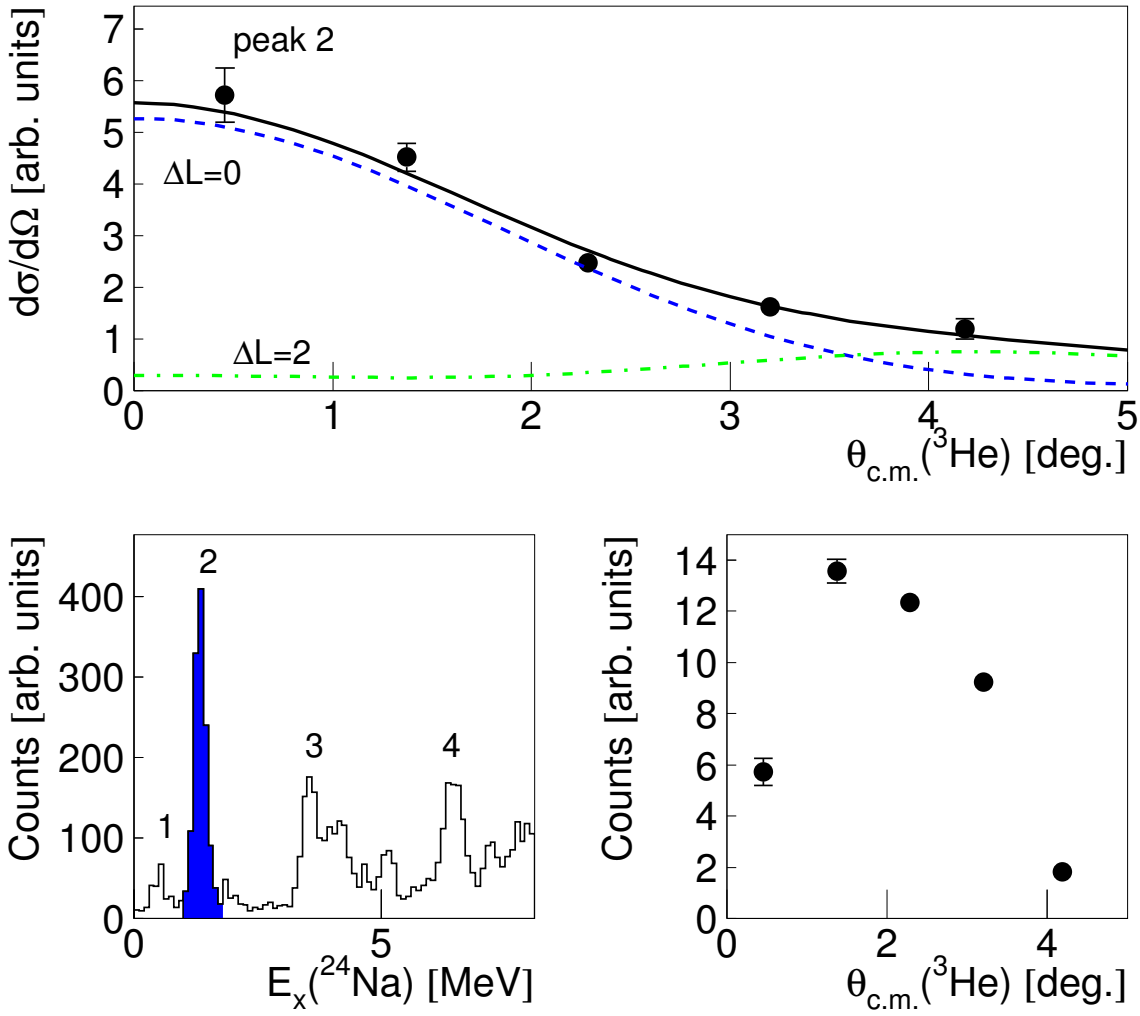

Figure 4.12: ^{24}Mg(t,^{3}He)^{24}Na(1^+, E_x=1.35 MeV) reaction differential cross section as a function of center-of-mass angle. a) The differential cross section is decomposed into the FOLD distributions for the two components in the $\Delta J = 1^+$ transition: the $\Delta L = 0$, $\Delta S = 1$ term (blue), and the $\Delta L = 2$, $\Delta S = 1$ term (green). The sum of the two components is shown in black. The location of the peak in the energy spectrum is highlighted in blue in panel b). The distribution of measured ^{3}He counts in excess of background is shown in panel c). (All error bars are statistical.)

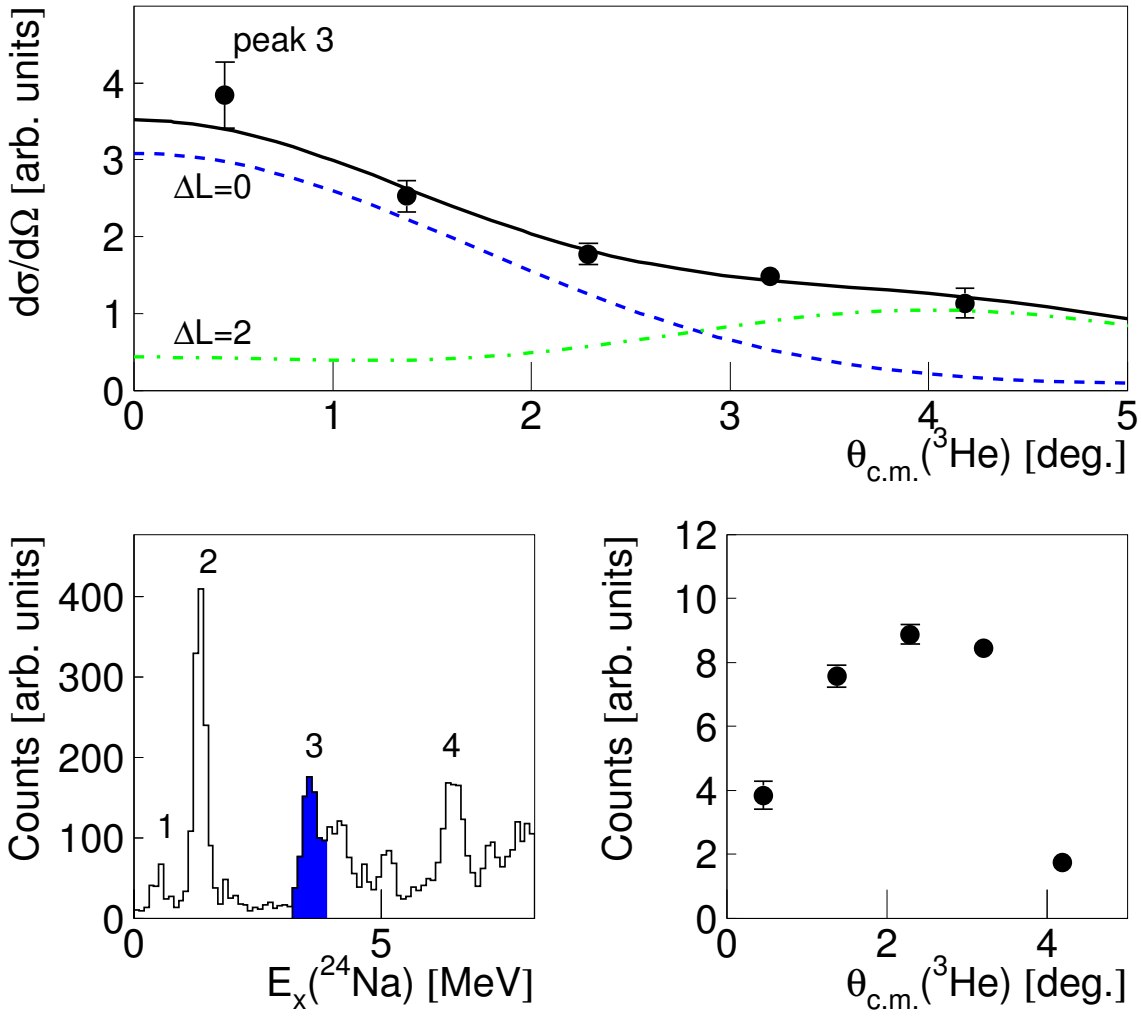

Figure 4.13: ^{24}Mg(t,^{3}He)^{24}Na(1^+, E_x=3.4 and 3.6 MeV) reaction differential cross section as a function of center-of-mass angle. a) The differential cross section is decomposed into the FOLD distributions for the two components in the $\Delta J = 1^+$ transition: the $\Delta L = 0$, $\Delta S = 1$ term (blue), and the $\Delta L = 2$, $\Delta S = 1$ term (green). The sum of the two components is shown in black. The location of the peak in the energy spectrum is highlighted in blue in panel b). The distribution of measured ^{3}He counts in excess of background is shown in panel c). (All error bars are statistical.)

Peak 3: 3.4 and 3.6 MeV

Two $J^\pi = 1+$ lie at 3.41 MeV and 3.59 MeV (and possibly another at 3.66 MeV), too close to be resolved within the energy resolution. For this region, the spectra are integrated over 3.14-3.94 MeV in excitation energy. The least-squares fit gives a scaling factor of 0.23±0.01 for the GT term and 0.72 ± 0.07 for the $\Delta L = 2, \Delta S = 1$ term. The χ^2 of the overall fit is 0.95 per degree of freedom. Extracting the GT component to zero degrees gives dσ/dΩ= 3.23±0.19 mb/sr for the sum of these two peaks. Given the only other state is a 3^+ state at 3.63 MeV, there is likely little systematic error due to a limited decomposition of the angular resolution.

Peak 4

In the fourth energy region, there is a known 1^+ state at 6.9 MeV and several other states with unassigned J^π values [31]. Previous data from the (d,^{2}He) probe finds strength at 6.70 and 7.2 MeV [68]. For this region, the spectra are integrated over 6.5-7.1 MeV in excitation energy. Given the relatively strong dipole transition at 6.5 MeV, the MDA for peak 4 includes the ΔL=1 distribution as shown in Fig. 4.14. The difference in the GT contributions for the MDA with ΔL=1 vs. ΔL=2 is 10%, which should be a fair indication of the systematic error for the MDA in this case using two components.

Missing ^{24}Na(1+) peaks

Within the 0 to 7.0 MeV excitation energy window, there are additional known $J^\pi = 1^+$ states in ^{24}Na for which the present data do not indicate Gamow-Teller-like angular distributions. One such example is the state at $E_x = 4.20$ MeV with $J^\pi = 1^+, 2, 3^+$ [31]. Figure 4.15 shows the failure of a forced fit of the angular

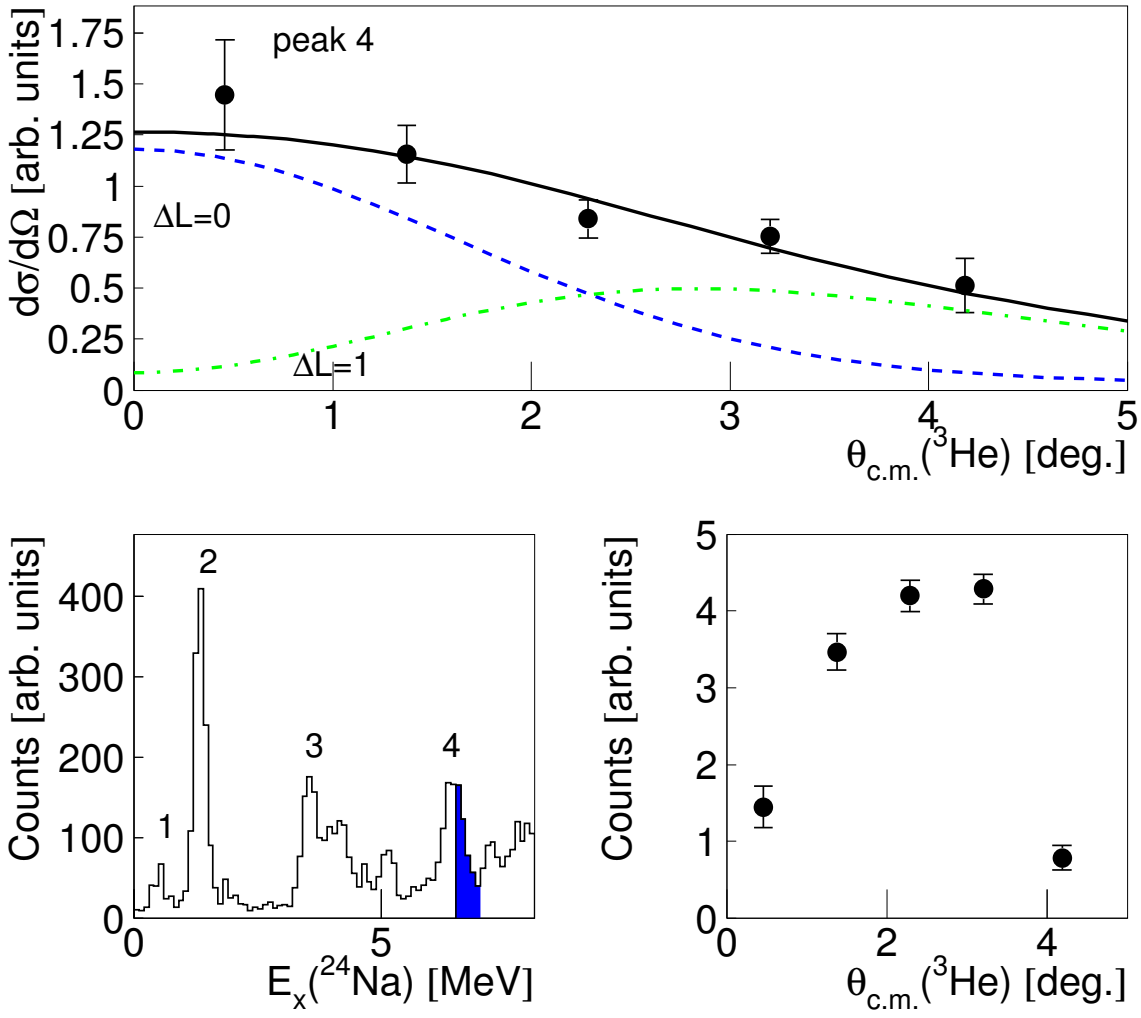

Figure 4.14: ^{24}Mg(t,^{3}He)^{24}Na(1^+, E_x=6.9 MeV) reaction differential cross section as a function of center-of-mass angle. a) The differential cross section is decomposed into the FOLD distributions for the two components in the $\Delta J = 1^+$ transition: the $\Delta L = 0$, $\Delta S = 1$ term (blue), and the dipole $\Delta L = 1$, $\Delta S = 1$ term (green) from a neighboring state. The sum of the two components is shown in black. The location of the peak in the energy spectrum is highlighted in blue in panel b). The distribution of measured ^{3}He counts in excess of background is shown in panel c). (All error bars are statistical.)

distribution to the calculated GT distribution for this state. Clearly, with a χ^2 for the one parameter fit in excess of 200 per degree of freedom, this state does not reproduce the FOLD angular distributions for the 1^+ transitions. The distribution appears to be dominated by the transitions with higher angular momentum transfer[37].

Similarly, the data do not identify $\Delta L = 0, \Delta S = 1$ transition angular distributions at 4.6, 5.8 and 6.9 MeV. The differential cross sections for the first energy regions are shown in panels a) and b) in Fig. 4.16. These angular distributions peak at angles more typical of larger ΔL transfer. Measuring these states with the (t,^{3}He) probe is both a problem of limited statistics and of an uncertain MDA due to the unknown or incomplete J^π assignments of the nearby states in the background. The MDA could be more successful with more information on the states in this region.

[37]Since the parity of the $J = 2$ state is unknown, an MDA is not performed here.

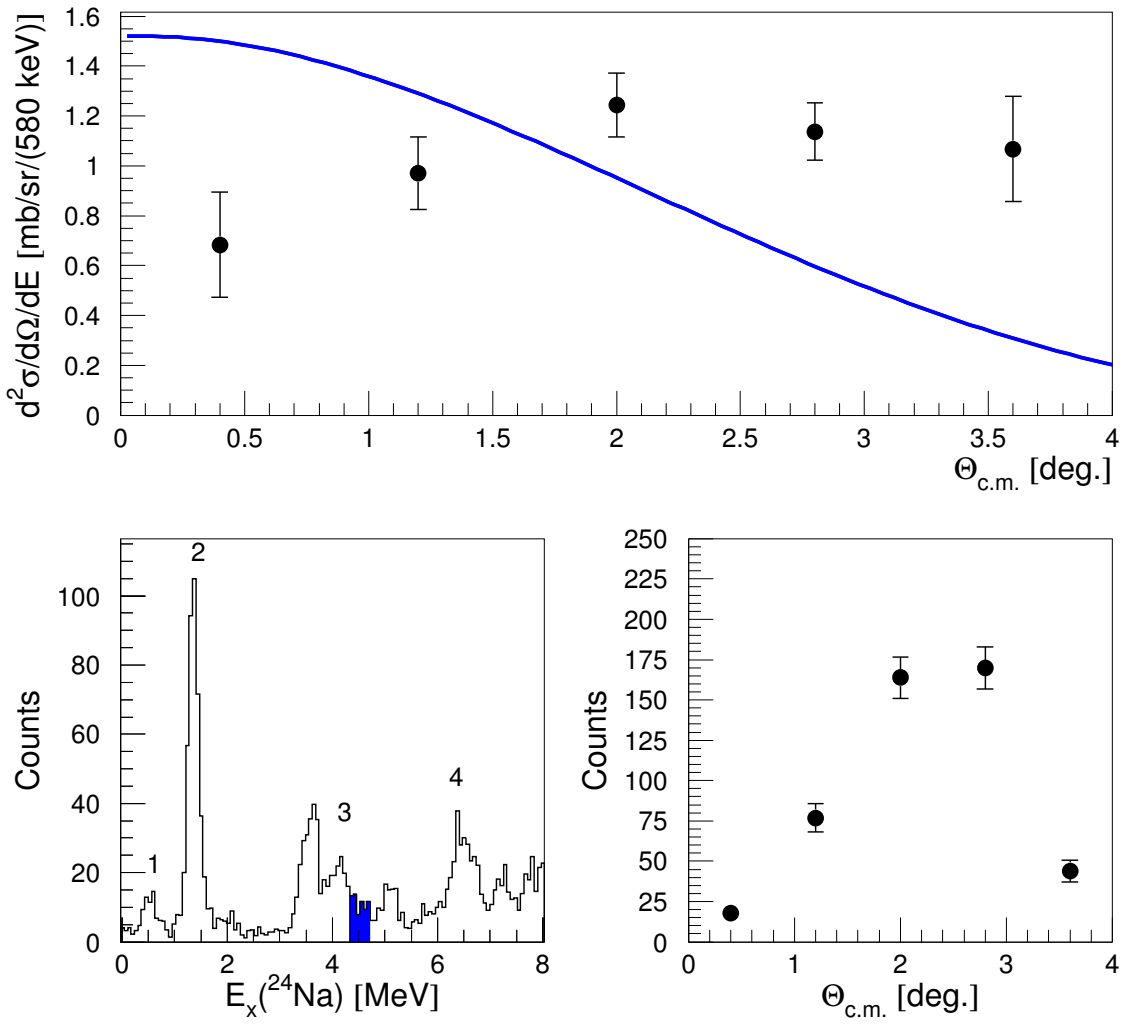

Figure 4.15: ^{24}Mg(t,^{3}He)^{24}Na(1^+, E_x=4.20 MeV) reaction differential cross section as a function of center-of-mass angle. a) The differential cross section is fitted with the FOLD distribution for the GT transition in blue. The location of the peak in the energy spectrum is highlighted in blue in panel b). The distribution of measured ^{3}He counts in excess of background is shown in panel c). (All error bars are statistical.)

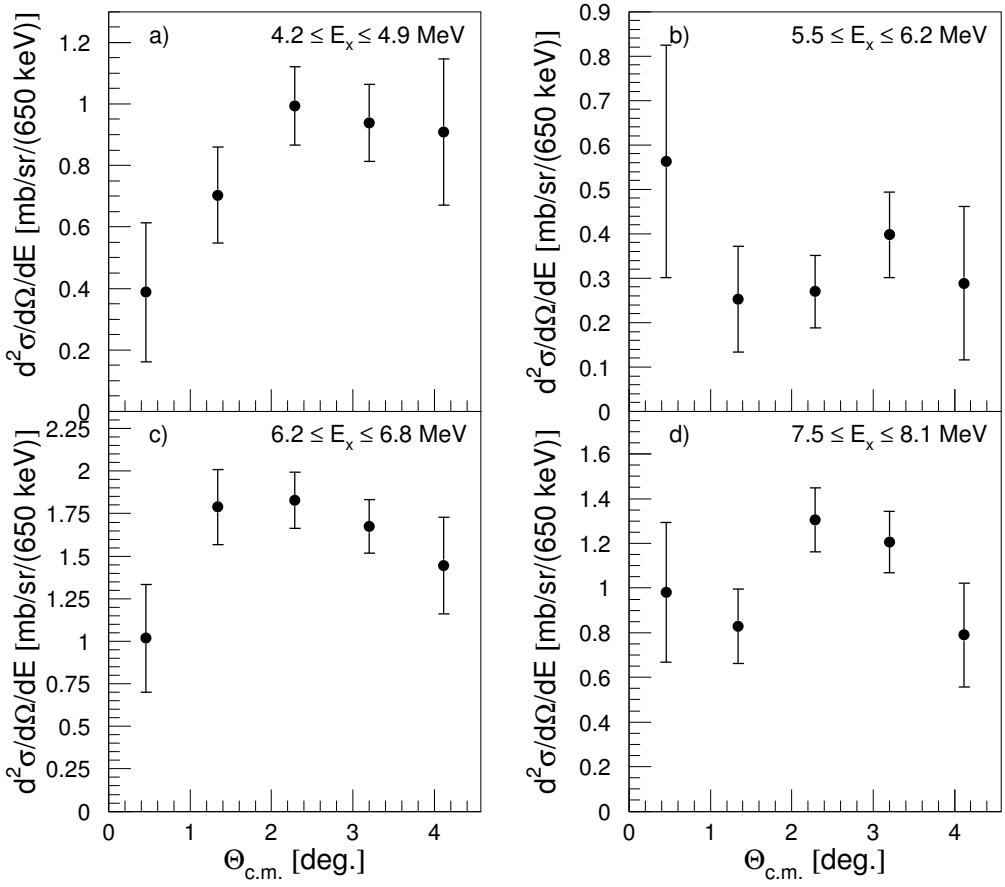

Figure 4.16: Typical ^{24}Na angular distributions for energies void of known 1^+ states.

CHAPTER 5

RESULTS

Chapter 5 presents the extraction of the Gamow-Teller strength in the first 7 MeV of excitation energy of ^{24}Na from the differential cross sections in Chapter 4. The extracted B(GT) are compared with competing charge exchange probes in the literature, measurements using the (d,^{2}He) probe at KVI in The Netherlands and the analogous transitions in ^{24}Mg(^{3}He,t)^{24}Al data from RCNP in Japan. Finally, the extracted B(GT) distribution is compared with theoretical calculations of B(GT) using the 1982 and the updated 2005 *sd*-shell model space interactions.

5.1 Experimental B(GT) Distribution

For the ^{24}Mg(t,^{3}He)^{24}Na reaction, the experimental B(GT) for individual states in ^{24}Na should be

$$B(GT) = \frac{1}{\hat{\sigma}_{GT}} \left[\frac{\frac{d\sigma}{d\Omega}(q=0)}{\frac{d\sigma}{d\Omega}(Q,0^\circ)} \right]_{\mathrm{FOLD}} \times \left[\frac{d\sigma}{d\Omega}(Q,0^\circ) \right]_{\mathrm{exp}}. \tag{5.1}$$

With the experimental $\frac{d\sigma}{d\Omega}(q=0)$ from Chapter 4, the missing ingredient is the unit cross section, $\hat{\sigma}_{GT}$. Unlike the (^{3}He,t) probe, a phenomenologically based relationship between unit cross section $\hat{\sigma}_{GT}$ and mass number A for the (t,^{3}He) probe at 345 MeV is so far unknown. Indeed, the purpose of this work is to start a systematic survey of

the relationship between GT strength and cross section for the (t,^{3}He) reaction over many nuclei.

The (^{3}He,t) data from RCNP are still useful for establishing the unit cross section for the (t,^{3}He) probe, $\hat{\sigma}_{(t,^3He)}$. The basic prescription is to follow the methods successfully used in Ref. [92] for ^{26}Mg(t,^{3}He)^{26}Na at the NSCL and ^{26}Mg(^{3}He,t)^{26}Al at RCNP. The ^{24}Mg target is an $N = Z$ nucleus, which more closely observes isospin symmetry than many other nuclei[38].

Assuming isospin symmetry, the strengths of analog transitions are connected by the multiplicative factor of the ratio of their Clebsch-Gordan coefficients; as is the case for $N = Z$ targets, $\frac{\mathrm{B(GT)}_{^{24}\mathrm{Mg}}(^3\mathrm{He,t})}{\mathrm{B(GT)}_{^{24}\mathrm{Mg}}(\mathrm{t},^3\mathrm{He})} = 1$. For the (^{3}He,$t$) probe at 420 MeV, the unit cross section is

$$\hat{\sigma}_{GT} = 109\, mb/sr \times A^{-0.65} = 13.8\, mb/sr. \tag{5.2}$$

To account for the slight differences (e.g. different kinematic factors $\frac{E_i E_f}{(\hbar^2 c^2 \pi)^2}$) between the (^{3}He,$t$) probe at 420 MeV and the (t,^{3}He) probe at 345 MeV, the cross sections calculated with FOLD are used as a guide. By taking the FOLD calculated $q = 0$ cross sections and dividing by the assumed B(GT) from the FOLD input[39], the relationship between the two unit cross sections is as follows:

$$\hat{\sigma}_{(^3He,t)} = \frac{21.6\, mb/sr}{0.884}, \tag{5.3}$$

$$\hat{\sigma}_{(t,^3He)} = \frac{20.8\, mb/sr}{0.918}, \tag{5.4}$$

$$\frac{\hat{\sigma}_{(t,^3He)}}{\hat{\sigma}_{(^3He,t)}} = 0.93. \tag{5.5}$$

[38]In nature, the locations of the individual levels measured in the $\Delta T_z = -1$ channel are slightly shifted from those measured in the $\Delta T_z = +1$ channel because of the Thomas-Ehrmann effect [81]. Similarly, the strengths in the two directions are slightly different, as shown in Fig. 5.2, coming from the Coulomb interaction for the slightly different total charge in the final state.

[39]The FOLD input is calculated with the code OXBASH using the USDB [13] interaction. The B(GT) for same interaction is also calculated in OXBASH.

The best value for the unit cross section $\hat{\sigma}_{(t,^3He)}$ for ^{24}Na is, therefore,

$$\hat{\sigma}_{(t,^3He)} = 13.8\, mb/sr \times 0.93 = 12.85\, mb/sr. \tag{5.6}$$

This unit cross section is useful, however, only once the systematic peculiarities with the normalization in this work are more fully understood- which is not the case here. In other words, the unit cross section derived above only applies to properly normalized (t,^{3}He) data. Using $\hat{\sigma}_{(t,^3He)}$ = 12.85 mb/sr would likely underestimate the B(GT) depending on how much of the incident triton intensity is lost on the narrow ^{24}Mg target. (For the main peak at 1.35 MeV, the B(GT) would then be approximately 0.4.)

The provisional solution to get around this complication is to correlate the main GT transition for the strongest $J^\pi = 1^+$ state at E_x=1.35 MeV with the analog state in ^{24}Mg(^{3}He,t) data. Based on the success of Ref. [92] with the ^{26}Mg target, the absolute normalization for GT strength in ^{24}Na (and thus the unit cross section) is fixed by pegging the B(GT) of the strong low-lying 1^+ state in ^{24}Na with the B(GT)= 0.668(3) measured for the analog state in ^{24}Al at RCNP. With higher strength, the state's increased cross section lends to higher confidence in the proportionality between cross section and B(GT) [92] by virtue of the relatively reduced $\Delta L = 2$, $\Delta S = 1$ amplitude. Reference [93] estimates the uncertainty for a state with B(GT)=0.7 to be approximately 5%, compared to 20% for states with B(GT)=0.01. So by removing the factors that naturally cancel in the equations above, the B(GT) for a given state with excitation energy E_i is

$$B(GT) = \frac{0.668}{5.30\ mb/sr} \times \left[\frac{d\sigma}{d\Omega}(q=0)\right]_{\mathrm{E_i}} = 1.26 \times \left[\frac{d\sigma}{d\Omega}(q=0)\right]_{\mathrm{E_i}}, \tag{5.7}$$

effectively making the unit cross section in Eq. 5.1 $\hat{\sigma}_{eff.}$=8.78 mb/sr $\sim$ 70% $\hat{\sigma}_{(t,^3He)}$.

The experimental ^{24}Na B(GT) values extracted from the present data and the factors used to calculate these values are listed in Table 5.1. Differential cross sections include only the GT ($\Delta L = 0$) component. The B(GT) uncertainties in the table are from the MDA fit errors in the zero degree cross section for the GT component only. Any systematic scaling in the overall normalization in the incident triton beam intensity will correspondingly scale the experimental B(GT) values without changing the energy. Similarly, fixing the main ^{24}Na peak to have a strength of 0.67 likely has two effects of systematically inflating the strengths, the first coming from the small difference in the strengths due to a slight breaking in isospin symmetry, and the second coming from the 7% difference in unit cross section for the two directions reflected in Eq. 5.5.

As the ratio for $\left[\frac{\frac{d\sigma}{d\Omega}(q=0)}{\frac{d\sigma}{d\Omega}(Q,0^\circ)}\right]_{\mathrm{FOLD}}$ monotonically increases smoothly and gradually with excitation energy, the transformation from the experimental Q-value to $q = 0$ for states that are not resolved experimentally is made by using the value of the ratio of $\left[\frac{\frac{d\sigma}{d\Omega}(q=0)}{\frac{d\sigma}{d\Omega}(Q,0^\circ)}\right]_{\mathrm{FOLD}}$ for the strongest GT state of all unresolved states for energy regions 3 and 4. The energy region labeled peak 3 is attributed to three known 1^+ states in ^{24}Na, of which the lowest contains the bulk of the GT strength. Without more statistics, this choice has little effect on the final strength and does not contribute to the uncertainty, given this ratio varies by $\sim$1% over 1 MeV of excitation energy and the higher states are very weak transitions.

The measured B(GT) distribution for both the (t,^{3}He) and (d,^{2}He) probes are shown in Fig. 5.1 and compared with shell-model calculations using the old USD and newly updated USDB [13] interactions. The (d,^{2}He) data are drawn with the B(GT) error bars listed in Ref. [68], but no energy errors. The energy error bars

^{24}Na	$\frac{d\sigma}{d\Omega}(Q,0^\circ)_{GT}$		$\frac{\frac{d\sigma}{d\Omega}(q=0)}{\frac{d\sigma}{d\Omega}(Q,0^\circ)}$	$\frac{d\sigma}{d\Omega}(q=0)_{exp.}$	Gamow-Teller Strength		
E_x [31] [MeV]	Present [mb/sr]	Fit Error	FOLD		B_{USDB}	B_{USD}	$B_{present}$
0.472	0.69(10)	14%	1.08	0.75(10)	0.122	0.061	0.08(1)
1.346	5.30(21)	4%	1.11	5.86(23)	0.919	0.955	0.67(3)
3.413			1.17		0.748	0.512	
3.589	3.23(19)	6%	1.18	3.78(23)	1.5×10^{-4}	0.034	0.43(3)
4.196			1.19		0.048	0.062	
6.962	1.22(16)	13%	1.29	1.57(20)	0.083	0.146	0.18(2)

Table 5.1: ^{24}Mg(t,^{3}He)^{24}Na reaction cross sections and extracted Gamow-Teller strengths. All cross sections are for the GT term only as extracted in Section 4.5.2. Fit errors are the uncertainties in the zero degree cross section for the GT component only. B(GT) errors are from this uncertainty alone. (See text.) Theoretical Gamow-Teller strengths for the USDB and USD interactions are calculated with OXBASH in the pn-formalism. Overall systematic error due to beam current integration, etc. is not included here. Theoretical strengths are *not* scaled by 0.59.

for the (t,^{3}He) data reflect the energies overwhich the data is integrated, not the experimental energy resolution. Unlike Table 5.1, the theoretical results are scaled by a multiplicative factor of 0.59[40] [15] to account for quenching of the GT strength due to configuration mixing with $2p-2h$ states and coupling to the $\Delta(1232)$-isobar nucleon-hole state.

With a neutron separation energy of 6.960 MeV and a proton separation energy of 10.55 MeV, $J^\pi = 1^+$ states in the ^{24}Na continuum above 7 MeV are excluded from this analysis.

[40]The factor 0.59±0.03 is an empirical factor for *sd*-shell nuclei [14, 84]. The factor changes slightly below the *sd*-shell and for heavier nuclei. The fact that this factor is not the same for all nuclei is a consequence of the evolution of the structure of nuclei as a function of mass number A.

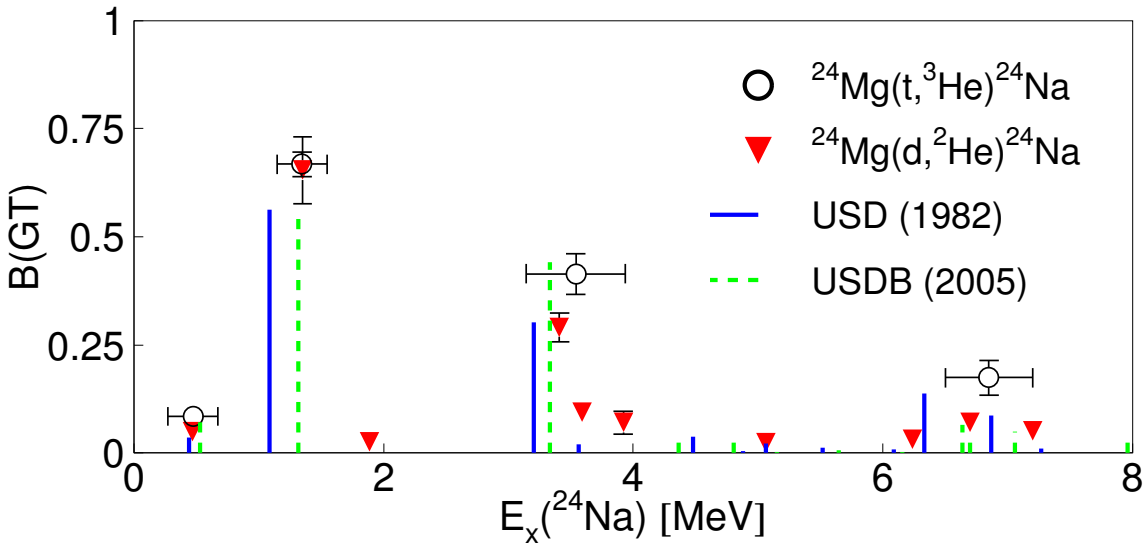

Figure 5.1: ^{24}Na B(GT) distribution comparison with theoretical calculations using the USD and USDB interactions. The energy error bars for the data are representative of the region for which the data are integrated. All theoretical strengths are scaled by 0.59 to reflect quenching.

5.2 Comparison with Other CEX Probes

A convenient way to compare GT strength distributions is to plot cumulative sums, as is done in Fig. 5.2. The summed strength for the present data is drawn with the results from a ^{24}Mg(d,^{2}He) experiment [68] and ^{24}Mg(^{3}He,t) experiment [91] are also included (the latter based on the assumption of isospin symmetry). For the sake of consistency, the results from the three data sets are plotted with incremental errors due to statistical and fitting uncertainties only. The summed strength for the present data and the ^{24}Mg(d,^{2}He)^{24}Na data largely overlap even conservative errors.

The energy resolution of the ^{24}Mg(d,^{2}He) experiment is 145 keV, slightly better than in the present experiment. Combined with the smaller statistical error margins,

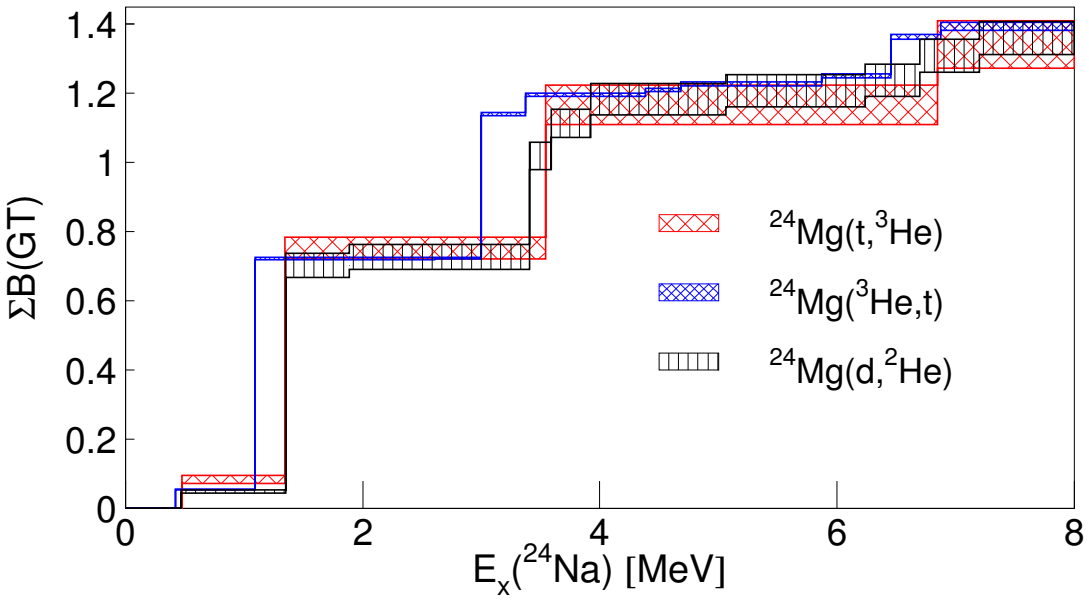

Figure 5.2: Summed B(GT) comparison of (t,^{3}He) data with competing CEX probes. The (t,^{3}He) and (d,^{2}He) data are in red (large hatches) and black (vertical bars), respectively. The (^{3}He,t) data in the opposite direction is in blue (small hatches).

some very weakly excited states seen in the (d,^{2}He) experiment are not separated in the present data. Nevertheless, the overall good agreement between the two data sets demonstrates that (t,^{3}He) reaction studies using a secondary beam of tritons produced from a ^{16}O primary beam are appropriate for extracting GT strength distributions. The ^{24}Mg(^{3}He,t) [41] experiment had very high resolution (35 keV) and very small statistical error margins, hence the finer detail. With better statistics, the (t,^{3}He) probe at the NSCL can likely achieve the detail seen in the (d,^{2}He) data.

5.3 Comparison with Theoretical Calculations Using the New *sd*-Shell Interaction

Figure 5.3 shows the summed B(GT) with three competing *sd* shell-model interactions, the USD, USDA and USDB. For the theory, no uncertainties are drawn to keep the figure uncluttered. As with previous measurements, the B(GT) distribution of the present data in excitation energy is generally in agreement with theoretical calculations, though the theoretical strengths must be quenched to 59%.

The old USD interaction places the states at slightly lower energies than seen in the data here or in high-precision measurements [1]. Between 3 and 6 MeV, the old interaction underestimates the summed strength in comparison to the other two interactions. The new USDB interaction for the $sd-$shell better reproduces both the relative strength and excitation-energy location for the main peak than the old USD interaction. At 7 MeV, all of the summed B(GT) distributions overlap.

[41] A detailed comparison between ^{24}Mg(p,n) [4] and ^{24}Mg(^{3}He,t) experiments is performed in Ref. [91].

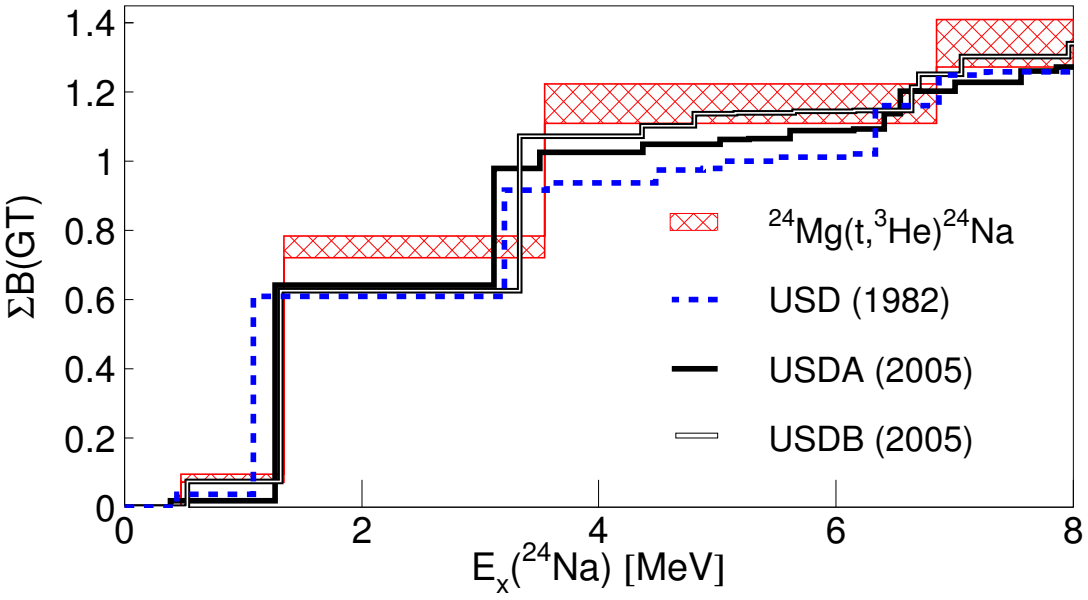

Figure 5.3: Summed B(GT) comparison of (t,^{3}He) data with theory. The USDA interaction is drawn in black. All theoretical strengths are are scaled by 0.59 to reflect quenching and exclude uncertainties.

CHAPTER 6

CONCLUSIONS

6.1 ^{12}C(t,^{3}He)^{12}B Results

The zero degree differential cross section of the $^{12}C(t,^3\mathrm{He})^{12}\mathrm{B}_{g.s.}$ reaction in the present work of 15.4±1.4±1.5 mb/sr, while differing significantly from a previous measurement at the NSCL, is consistent with an analogous transition for the ^{12}C(^{3}He,t)^{12}N reaction recently measured at RCNP. One previous (t,^{3}He) experiment on ^{12}C cannot be easily compared to the present data. Alternately, the Cole et al. data [23] differs significantly, most likely due to uncontrolled and poorly quantified systematic errors in incident triton beam normalization in both experiments. For the current configuration at the NSCL, the triton normalization and the acceptance of the S800 make up the two largest experimental contributions to uncertainty in cross section.

Since there are no other low-lying states in ^{12}B within typical energy uncertainties above the ground state, there are no excess events from states of different angular momenta or parity. The high cross section for the ^{12}B ground state, measured β decay, scarcity of low-lying states, and low cost for the carbon makes for an ideal calibration target, which will no doubt be measured many times over.

6.2 ^{24}Mg(t,^{3}He)^{24}Na Results

The present experiment is the first charge-exchange reaction data on a ^{24}Mg target using the (t,^{3}He) probe at energies above 100 MeV/nucleon. Cross sections are extracted for individual $J^\pi=1^+$ peaks at ^{24}Na excitation energies of 0.4 MeV and 1.3 MeV only. The 1^+ peaks at from 3.0-4.0 MeV and 6.5-7.0 MeV are grouped into two regions and fitted with typical differential cross sections for 1^+ peaks in the respective energy region.

A combination of lower cross section and the presence of other non-GT transition peaks prevent the resolution of the other know 1^+ states through 7 MeV, and are not included here. In particular, the present analysis does not include the following states that are resolved in the Rakers et al. data [68] for ^{24}Mg(d,^{2}He)^{24}Na: 1.89 MeV, 5.06 MeV, and 7.2 MeV. States above 7 MeV do not appear analysiss due to the Q value for charge exchange on carbon on the target edges and due to the neutron separation energy. Experimental uncertainties are larger for the ^{24}Na results as compared to ^{12}B due to the smaller ^{24}Mg target and other issues related to the calibration of the number of tritons on target.

The systematic uncertainty due to the normalization that is particularly pronounced in the narrow ^{24}Mg target is not included in these cross sections. Instead, the B(GT) extraction is calibrated with ^{24}Mg(t,^{3}He)^{24}Al data. Overall, the B(GT) distribution in the present data is in good agreement with measurements with other probes and with theoretical calculations.

6.3 Future of (t,^{3}He) Experiments at the NSCL

As a result of the present experiment, magnets in the S800 analysis line (upstream from target) and spectrometer line (downstream from target) have been realigned [90]. Together with improved control of the high-intensity ^{16}O primary beam, the realignment produced higher rates (by a factor of 2) for tritons on target due to improved transmission as already seen in NSCL Experiments 05027 on ^{64}Zn and 06032 on ^{150}Sm and other targets. Aside from technical challenges, such as making large targets of sometimes brittle material, the main hurdle to running (t,^{3}He) experiments for the purpose of extracting Gamow-Teller strength is the competition for beam time at the NSCL.

Thoughtful target choices are imperative. For the purpose of improving astrophysics weak interaction databases for astrophysics modelling, there is little guidance as to which nuclei will have the greatest impact in reducing supernova modelling uncertainties, for example. No such Top Ten lists really exist. Though there are lists of nuclei compiled by Heger et al. [48, 46] of the most important weak reactions for SNe of a given progenitor mass group, there is no clear correspondence between a single reaction and the macroscopic SNe dynamics or the final isotopic nuclear abundances.

Unfortunately, these priorities are a luxury; target choice is often determined either by the affordability of a given target material[42] or the target material malleability, the ease with which the material can be uniformly rolled into a 2 cm $\times$ 5 cm cross section.

[42]Material for a 10 g ^{50}V target rents for approximately \$50,000.

6.4 Future of B(GT) Measurements

These (t,^{3}He) analyses are predicated on several reasonable but untested assumptions. First, on the reaction side, there is no elastic scattering (t,t') data for 100-200 MeV/nucleon. The S800 spectrometer at the NSCL cannot create magnetic fields strong enough to bend tritons at 125 MeV/nucleon into the focal plane due to the low charge-to-mass ratio, which gives these tritons such a high magnetic rigidity. Instead, we follow the examples in the literature where the optical model potentials for tritons of this energy are taken from scaled (by a factor of 0.85) ^{3}He optical model potentials from (^{3}He,^{3}He') data (see e.g. Ref.[92] and references therein). While the effect should be small, new experimental data for elastic scattering of tritons of 125 MeV/nucleon has the potential to make systematic adjustments to all B(GT) measurements obtained from the (t,^{3}He) charge-exchange probe.

Second, on the structure side, the angular distributions of excited states are fitted with calculations based on standard interactions, some of which have not been updated since the 1960s and 1970s and are possibly inappropriate for charge-exchange reactions, depending on to which data the interactions were fit. This theoretical source of uncertainty can have a significant impact on strengths measured for nuclei with substantially fragmented GT strength or background states with similar angular distributions. Because the (t,^{3}He) probe currently has limited energy resolution and beam intensities at the NSCL, excitation energy regions with small GT strength are difficult to resolve on a state-by-state basis, which further complicates a multipole decomposition analysis of the angular distribution of the differential cross section. Several groups are currently working on improving old interactions by updating the

fits to include recent nuclear structure data and developing new reaction codes specifically designed for charge-exchange experiments.

There are, however, no known proposals or plans to measure triton elastic scattering at charge-exchange energies. Future facilities with plans to run charge-exchange experiments in inverse kinematics, however, will have the luxury of taking elastic scattering data with the charge-exchange data since the magnetic rigidity of the beam will only differ slightly from that of the studied projectile-like nucleus. A ^{58}Ni beam at 125 MeV/nucleon, for example, only makes a 5% change in magnetic rigidity after a single isospin flip, as opposed to the 100% increase in rigidity for the ^{3}He reacted beam when compared to the scattered t beam. The (^{7}Li,^{7}Be*) probe in inverse kinematics, for example, has the potential to carry smaller inherent systematic errors from optical model potentials.

Even with these limitations, the (t,^{3}He) probe is the best available tool today for experimental determination of B(GT) distributions for stable nuclei in the (n, p) direction for several reasons. The (n, p) probe's energy resolution of an MeV is simply not good enough for the sensitivity of astrophysical electron capture in supernovae. While the (d,^{2}He) probe has competitive energy resolution, the (d,^{2}He) program at KVI is no longer running and has no plans to run in the foreseeable future. More massive probes can only introduce more complicated reactions and hinder extraction of B(GT) from cross sections unreliable due to linearity breaking effects for these probes. Charge exchange in inverse kinematics has inferior energy resolution and is still under development, and faces several technical challenges, partly due to the branching ratio and efficiency for detecting the 430 keV gamma-decay of the excited ^{7}Be*.

Ultimately, the holy grail of B(GT) measurements lies in charge exchange on unstable nuclei. These measurements will be the only constraint on the theoretical calculations that are used in weak reaction libraries for supernovae model calculations, which are heretofore used unchecked. Systematic misplacement of Gamow-Teller strength for even a scant percentage of a core's mass has been shown to have macroscopic consequences for electron capture rates and energy production both during core collapse and post bounce dynamics [59]. These measurements for unstable nuclei are a growing motivation for design plans for future medium energy nuclear physics facilities in the United States, such as the proposed upgrade to the NSCL and new rare isotope accelerator facitlities.

APPENDIX A

EVENT RECONSTRUCTION

A transfer matrix R maps the ^{3}He particle positions and angles in the S800 focal plane (x_{fp}, y_{fp}, a_{fp}, b_{fp}) to the phase space parameters at the target (y_{ta}, a_{ta}, b_{ta}, δ_{ta}) immediately after the charge exchange reaction,

$$\begin{bmatrix} a_{ta} \\ y_{ta} \\ b_{ta} \\ \delta_{ta} \end{bmatrix} = R \begin{bmatrix} x_{fp} \\ a_{fp} \\ y_{fp} \\ b_{fp} \end{bmatrix}. \tag{A.1}$$

The inverted transfer matrix R is calculated for a given magnetic field setting in two quadrupole magnets and two 75° bend dipoles References. [19, 21] nominally describe the calculation of the inverted transfer matrix R for a given magnetic field setting and Ref. [7] describes the removal of abberations.

For a complete description of inverse maps and ray tracing for particle optical systems in general and for the S800 spectrometer specifically, see the COSY Infinity Version 8.1 User's Guide and Reference Manual [8] [43] and Ref. [53] respectively. Calculate an inverse map for arbitrary magnet currents, particles and shifts in the focal plane and target at http://www.nscl.msu.edu/tech/devices/s800/map2.php.

[43] In particular, start with the manual's section 1.4, "How to avoid reading this manual."

A.1 Corrections to COSY File Variables

As a result of this work, inverse maps are now offered with variable positions of the focal plane and target position as alternatives to the default values.

The following tables are the inverse map parameters as used in the present data analysis with an S800 spectrometer magnetic rigidity of 2.3100 T·m, and shifts of the focal plane and target positions as described in Section 3.3.4.

Table A.1: Inverse map parameters for reconstructing angle a_{ta} in the non-dispersive direction on the target. See Section 3.3.4, Equation 3.3.

Coefficient $C(i,j,k,l)$	Order	Order in x_{fp} i	Order in y_{fp} j	Order in a_{fp} k	Order in b_{fp} l
0.01692579890008413	1	1	0	0	0
-0.95718105540867982	1	0	1	0	0
-0.01249279020270155	2	2	0	0	0
0.19619833903500761	2	1	1	0	0
0.04097706613601207	2	0	2	0	0
0.02927551899816852	2	0	0	2	0
-0.24322257835494271	2	0	0	1	1
0.26766968817234421	2	0	0	0	2
0.00342431985152042	3	3	0	0	0
-0.05223017854226105	3	2	1	0	0
0.19173163312895480	3	1	2	0	0
-4.30915934458574235	3	0	3	0	0
0.11582887398796519	3	1	0	2	0
-6.91669721032469020	3	0	1	2	0
-0.17013833005601339	3	1	0	1	1
13.86227771659214980	3	0	1	1	1
-0.06934958568897057	3	1	0	0	2
-8.68325549834845845	3	0	1	0	2
-0.00093393922304288	4	4	0	0	0
0.02047672306376659	4	3	1	0	0
-0.39094523064337272	4	2	2	0	0
4.93592099963043474	4	1	3	0	0
1.84103407084185400	4	0	4	0	0
-0.12723846760132071	4	2	0	2	0
2.99600230752782215	4	1	1	2	0
34.93732082918054260	4	0	2	2	0
0.25509465888610000	4	0	0	4	0
0.18415266208499700	4	2	0	1	1
-0.50522276376313446	4	1	1	1	1
-243.54451932953631399	4	0	2	1	1
-3.55163419393023005	4	0	0	3	1
0.00618535780447680	4	2	0	0	2
-1.77752088172985201	4	1	1	0	2
202.29130304587150135	4	0	2	0	2

(Continued on following page.)

Table A.1: (continued)

Coefficient $C(i,j,k,l)$	Order	Order in x_{fp} i	Order in y_{fp} j	Order in a_{fp} k	Order in b_{fp} l
19.02178413818047176	4	0	0	2	2
-60.30885718279660779	4	0	0	1	3
82.55209873813063837	4	0	0	0	4
0.00029165312679237	5	5	0	0	0
-0.01255140712709260	5	4	1	0	0
0.34233828314416748	5	3	2	0	0
-3.61568694369820509	5	2	3	0	0
7.72256482823526369	5	1	4	0	0
-96.73090170616305272	5	0	5	0	0
0.05628428583590045	5	3	0	2	0
-0.35075520296287938	5	2	1	2	0
-14.34364153422695054	5	1	2	2	0
-231.24188164621170927	5	0	3	2	0
2.17081777761925609	5	1	0	4	0
-131.00919127069849424	5	0	1	4	0
-0.04441726991758074	5	3	0	1	1
-5.14372776474627980	5	2	1	1	1
141.20426906911541209	5	1	2	1	1
974.27242847175602947	5	0	3	1	1
-17.11703115878061965	5	1	0	3	1
1076.54159963705001246	5	0	1	3	1
-0.03521475272898729	5	3	0	0	2
4.56693602197211312	5	2	1	0	2
-75.68782934204722324	5	1	2	0	2
-1861.16820017408599597	5	0	3	0	2
88.18348902774171449	5	1	0	2	2
-5518.76986105005744321	5	0	1	2	2
-225.37405250255940814	5	1	0	1	3
14235.18796247542013589	5	0	1	1	3
130.29826111915468800	5	1	0	0	4
-9507.68736347999401914	5	0	1	0	4

Table A.2: Inverse map parameters for reconstructing angle y_{ta} in the non-dispersive direction on the target. See Section 3.3.4, Equation 3.3.

Coefficient $C(i,j,k,l)$	Order	Order in x_{fp} i	Order in y_{fp} j	Order in a_{fp} k	Order in b_{fp} l
-0.29659502527203729	1	0	0	1	0
0.83693178956864900	1	0	0	0	1
-0.10005776374510150	2	1	0	1	0
0.12463283364152369	2	0	1	1	0
0.12065842976306471	2	1	0	0	1
-2.57609817427697996	2	0	1	0	1
0.01732191153276191	3	2	0	1	0
-0.21035687833260600	3	1	1	1	0
9.51334161802247102	3	0	2	1	0
2.76864995360991895	3	0	0	3	0
-0.00626410007822936	3	2	0	0	1
-0.68361243407646621	3	1	1	0	1
-9.80699874298026764	3	0	2	0	1
0.53032695220363801	3	0	0	2	1
-52.49344240902068748	3	0	0	1	2
137.33687507870780564	3	0	0	0	3
-0.00482471384028922	4	3	0	1	0
0.40736130963726380	4	2	1	1	0
-6.88594597703721334	4	1	2	1	0
-20.02062854386926105	4	0	3	1	0
-1.41532727425946203	4	1	0	3	0
-24.74871586786553124	4	0	1	3	0
-0.00443874292216284	4	3	0	0	1
0.04870521829213800	4	2	1	0	1
1.14974495633321205	4	1	2	0	1
130.39310216985120405	4	0	3	0	1
5.51104095985695874	4	1	0	2	1
219.08152306213739280	4	0	1	2	1
-27.71282224502958869	4	1	0	1	2
-382.23250479100659049	4	0	1	1	2
66.66820666933048756	4	1	0	0	3
136.05268703717331391	4	0	1	0	3
0.00454977834327933	5	4	0	1	0
-0.28568758691750751	5	3	1	1	0

(Continued on following page.)

Table A.2: (continued)

Coefficient $C(i,j,k,l)$	Order	Order in x_{fp} i	Order in y_{fp} j	Order in a_{fp} k	Order in b_{fp} l
3.06599365907849819	5	2	2	1	0
9.58751450207432043	5	1	3	1	0
125.49758762468489692	5	0	4	1	0
0.23074267007732610	5	2	0	3	0
3.43713955999217902	5	1	1	3	0
264.90071942898379120	5	0	2	3	0
41.42413798385626222	5	0	0	5	0
-0.00130060125276432	5	4	0	0	1
0.00650901109380145	5	3	1	0	1
5.80756874351331298	5	2	2	0	1
-130.71598940345998585	5	1	3	0	1
-143.23177548855031205	5	0	4	0	1
-0.10161833141157960	5	2	0	2	1
-57.15953417332183051	5	1	1	2	1
-1700.50269156397803272	5	0	2	2	1
-416.04999364083619184	5	0	0	4	1
2.87125420536313491	5	2	0	1	2
-34.52027953372807190	5	1	1	1	2
6225.10467869811873243	5	0	2	1	2
1294.63472657891111339	5	0	0	3	2
-7.16378481623262964	5	2	0	0	3
163.99448390835959799	5	1	1	0	3
-8385.84808669700396422	5	0	2	0	3
6543.39394668609656947	5	0	0	2	3
-52420.60534331521193963	5	0	0	1	4
88258.38994798292696942	5	0	0	0	5

Table A.3: Inverse map parameters for reconstructing angle b_{ta} in the non-dispersive direction on the target. See Section 3.3.4, Equation 3.3.

Coefficient $C(i,j,k,l)$	Order	Order in x_{fp} i	Order in y_{fp} j	Order in a_{fp} k	Order in b_{fp} l
-1.42867229344592794	1	0	0	1	0
0.65982650610793026	1	0	0	0	1
0.10361597266967131	2	1	0	1	0
4.09022239145823097	2	0	1	1	0
0.06622191138795594	2	1	0	0	1
-23.67336127433368986	2	0	1	0	1
0.02684201267521681	3	2	0	1	0
-0.80936300399720307	3	1	1	1	0
-6.32656907230881771	3	0	2	1	0
-8.06522377552861336	3	0	0	3	0
-0.13187335308033479	3	2	0	0	1
5.77314659440557243	3	1	1	0	1
17.35501356868835998	3	0	2	0	1
87.88449287305357416	3	0	0	2	1
-494.40775791554739271	3	0	0	1	2
1084.63425562925704071	3	0	0	0	3
-0.00476294452409521	4	3	0	1	0
-0.18296272845769401	4	2	1	1	0
6.13299358771711756	4	1	2	1	0
18.43016532502857174	4	0	3	1	0
1.80119449140463006	4	1	0	3	0
12.67655068694486076	4	0	1	3	0
0.02094999803479995	4	3	0	0	1
-0.88782414221146500	4	2	1	0	1
-3.20406069853717490	4	1	2	0	1
-140.19367310956531014	4	0	3	0	1
-15.48174886582460985	4	1	0	2	1
-65.62178223976096092	4	0	1	2	1
69.77591359345881017	4	1	0	1	2
60.36025584308016079	4	0	1	1	2
-115.39207696537759773	4	1	0	0	3
-1116.76021283609907186	4	0	1	0	3
-0.00222260766032243	5	4	0	1	0
0.21804792998542241	5	3	1	1	0
-2.46611626166754716	5	2	2	1	0

(Continued on following page.)

Table A.3: (continued)

Coefficient $C(i,j,k,l)$	Order	Order in x_{fp} i	Order in y_{fp} j	Order in a_{fp} k	Order in b_{fp} l
-10.62234592998315996	5	1	3	1	0
-128.45934978402320326	5	0	4	1	0
-0.21988455922774319	5	2	0	3	0
-1.34696293889601604	5	1	1	3	0
-305.98406316297200647	5	0	2	3	0
-109.45973743117770027	5	0	0	5	0
-0.00166271425260294	5	4	0	0	1
0.11759787815510450	5	3	1	0	1
-5.16959577091264588	5	2	2	0	1
128.63507643266601121	5	1	3	0	1
200.17383583993009211	5	0	4	0	1
3.61318566328561586	5	2	0	2	1
28.05403844288126081	5	1	1	2	1
1856.52887885242307675	5	0	2	2	1
2489.57172455471300054	5	0	0	4	1
-24.63221232421146922	5	2	0	1	2
57.80385274582175015	5	1	1	1	2
-5715.90978943562004133	5	0	2	1	2
-27709.33578310242955922	5	0	0	3	2
50.24793852351042034	5	2	0	0	3
-155.99774892850160768	5	1	1	0	3
8818.35812519586033886	5	0	2	0	3
168521.73965979210333899	5	0	0	2	3
-540070.73281427170149982	5	0	0	1	4
727422.08324769511818886	5	0	0	0	5

Table A.4: Inverse map parameters for reconstructing angle δ_{ta} in the non-dispersive direction on the target. See Section 3.3.4, Equation 3.3.

Coefficient $C(i,j,k,l)$	Order	Order in x_{fp} i	Order in y_{fp} j	Order in a_{fp} k	Order in b_{fp} l
-0.00000000000000036	0	0	0	0	0
0.19875345017911469	1	1	0	0	0
-0.00305606217133495	1	0	1	0	0
0.01460774297086249	2	2	0	0	0
0.15820664286206851	2	1	1	0	0
0.54987114373926693	2	0	2	0	0
0.10312826594930760	2	0	0	2	0
-0.66450228793174915	2	0	0	1	1
1.80006855912970298	2	0	0	0	2
0.00117643464438051	3	3	0	0	0
-0.02320060759448063	3	2	1	0	0
0.14909716475975460	3	1	2	0	0
-2.36513769939297891	3	0	3	0	0
0.04929430585810790	3	1	0	2	0
-3.08847079912818900	3	0	1	2	0
-0.06297358131710659	3	1	0	1	1
5.75689186940123410	3	0	1	1	1
0.00492300446262541	3	1	0	0	2
-2.76566646504300007	3	0	1	0	2
-0.00049992164773450	4	4	0	0	0
0.01185632908568632	4	3	1	0	0
-0.26507916096335610	4	2	2	0	0
3.18347656775321797	4	1	3	0	0
-1.57051219639993400	4	0	4	0	0
-0.06657152057516398	4	2	0	2	0
1.96862836209606695	4	1	1	2	0
12.56354680379386046	4	0	2	2	0
0.23401390702239130	4	0	0	4	0
0.09510111306920499	4	2	0	1	1
-1.36932949314169194	4	1	1	1	1
-104.90742272303660343	4	0	2	1	1
-3.99878853684919822	4	0	0	3	1
-0.00023330963539529	4	2	0	0	2
-0.58890563034511478	4	1	1	0	2
90.69830983286598780	4	0	2	0	2

(Continued on following page.)

Table A.4: (continued)

Coefficient $C(i,j,k,l)$	Order	Order in x_{fp} i	Order in y_{fp} j	Order in a_{fp} k	Order in b_{fp} l
28.44052766332890059	4	0	0	2	2
-97.53561658184661098	4	0	0	1	3
117.04797261446880441	4	0	0	0	4
0.00017912313839380	5	5	0	0	0
-0.00868836204410186	5	4	1	0	0
0.24379747116716280	5	3	2	0	0
-2.76422753013315914	5	2	3	0	0
8.24105389671724531	5	1	4	0	0
-51.27690608957126273	5	0	5	0	0
0.03701181687591169	5	3	0	2	0
-0.59617385830039293	5	2	1	2	0
-5.52639383708226184	5	1	2	2	0
-99.17320577685354976	5	0	3	2	0
0.86813565755674205	5	1	0	4	0
-55.77444847334260913	5	0	1	4	0
-0.03445449312059103	5	3	0	1	1
-1.98479954148953297	5	2	1	1	1
79.84336852905580884	5	1	2	1	1
334.70577696170801119	5	0	3	1	1
-6.64916536943847980	5	1	0	3	1
464.85413826853471164	5	0	1	3	1
-0.01510484828323259	5	3	0	0	2
2.15403771174295500	5	2	1	0	2
-50.87022717224800772	5	1	2	0	2
-742.59173168164466006	5	0	3	0	2
36.13068919395402645	5	1	0	2	2
-2457.36920694648188146	5	0	1	2	2
-99.08541282690426044	5	1	0	1	3
6527.31151302667967684	5	0	1	1	3
67.76925846223034000	5	1	0	0	4
-4581.29030199191038264	5	0	1	0	4

A.2 Missing Mass Calculation

The excitation energy of the target nuclei is reconstructed from the kinematics of the ^{3}He particle as a so-called "missing mass." The reconstructed ^{3}He energy is

$$E_{^3He} = E_{S800}\,(1 + \delta_{ta}) \;+\; E_{loss}, \tag{A.2}$$

where E_{S800} is the energy of the central ray of the S800 spectrometer as calculated with the LISE++ physical calculator [5] for the Bρ settings of the S800 dipole magnets and E_{loss} is the energy loss of the ^{3}He as it travels through approximately half of the target material. (Because the transverse location of the reaction is not known, the uncertainty in the energy loss in the target material introduces an uncertainty in the calculated excitation energy of the target recoil. Clearly, increasing the reaction count rate with increasing target thickness, and thus reducing statistical error, comes at the cost of energy resolution.)

The reconstructed angles of the ^{3}He as it leaves the target holds information as to the ^{3}He final momentum $\vec{p'}$. Together with the assumed initial triton momentum $\vec{p}$, the change in momentum of the target nucleus, p^2_{miss}, is then

$$p^2_{miss} = \Delta p_x^2 + \Delta p_y^2 + \Delta p_z^2, \tag{A.3}$$

where

$$\Delta p_i^2 = (p_i^{'} - p_i)^2. \tag{A.4}$$

By definition[44],

$$E^2_{missing} = m^2_{missing} \;+\; p^2_{missing}. \tag{A.5}$$

[44]Here, and throughout the text, $c = 1$.

Therefore, from energy and momentum conservation, the recoil carries off an excess of mass from the ground state mass of

$$m_{missing} = \sqrt{E^2_{missing} - p^2_{missing}} - m^{g.s.}_{target\ recoil}. \tag{A.6}$$

The target recoil ground state mass $m^{g.s.}_{target\ recoil}$ (e.g. ^{12}B in the case of the ^{12}C(t,^{3}He)^{12}B reaction) is taken from the CatKIN version 2.01 program, which uses 2000 atomic mass evaluations [20]. The mass $m_{missing}$ in excess of the recoil ground state mass is identified as the excitation energy of the outgoing target-like channel.

APPENDIX B

FOLD OUTPUT

Tables B.1, B.2 and B.3 are the output from FOLD (distorted wave Born approximation) of angular distributions of differential cross section ($d\sigma/d\Omega(\Theta_{scat})$) for the ΔL,J$^{\pi}$ transitions used in the Multipole Decomposition Analysis for each target in Chapter 4. Peak energies labelled in Tables B.2 and B.3 and the OBTD input to FOLD for the ^{24}Mg(t,^{3}He)^{24}Na reaction are those calculated for the UDSB interaction [13] using OXBASH [16].

Θ_{scat} [$deg.$]	dσ/dΩ [mb/sr] ΔL=0, ΔS=1	σ/dΩ [mb/sr] ΔL=2, ΔS=1
0.0	24.020	0.456
0.2	23.920	0.456
0.4	23.620	0.456
0.6	23.120	0.457
0.8	22.450	0.461
1.0	21.610	0.469
1.2	20.630	0.485
1.4	19.530	0.509
1.6	18.330	0.544
1.8	17.060	0.591
2.0	15.740	0.650
2.2	14.410	0.721
2.4	13.070	0.802
2.6	11.760	0.892
2.8	10.480	0.989
3.0	9.261	1.087
3.2	8.111	1.185
3.4	7.038	1.277
3.6	6.050	1.361
3.8	5.151	1.433
4.0	4.343	1.490
4.2	3.624	1.529
4.4	2.993	1.550
4.6	2.446	1.551
4.8	1.978	1.533
5.0	1.582	1.496
5.2	1.253	1.443
5.4	0.984	1.374
5.6	0.768	1.293
5.8	0.598	1.202
6.0	0.467	1.104

Table B.1: FOLD calculated $d\sigma/\mathrm{d}\Omega$ for ^{12}C(t,^{3}He)^{12}B$_{g.s.}(1^{+})$.

	Peak 1 E_x= 0.54 MeV $d\sigma/d\Omega$ [mb/sr]		Peak 2 E_x= 1.32 MeV $\sigma/d\Omega$ [mb/sr]		Peak 3 E_x= 3.34 MeV $d\sigma/d\Omega$ [mb/sr]	
Θ_{scat} [*deg.*]	ΔL=0 ΔS=0	ΔL=2 ΔS=1	ΔL=0 ΔS=0	ΔL=2 ΔS=1	ΔL=0 ΔS=0	ΔL=2 ΔS=1
0.0	2.765	0.017	18.720	0.330	13.280	0.602
0.2	2.750	0.017	18.610	0.328	13.190	0.599
0.4	2.707	0.017	18.270	0.320	12.920	0.588
0.6	2.636	0.016	17.730	0.310	12.490	0.573
0.8	2.539	0.016	17.000	0.297	11.900	0.558
1.0	2.420	0.015	16.100	0.286	11.190	0.546
1.2	2.281	0.014	15.070	0.278	10.380	0.542
1.4	2.126	0.014	13.920	0.276	9.489	0.551
1.6	1.959	0.014	12.700	0.283	8.556	0.575
1.8	1.783	0.014	11.440	0.299	7.608	0.618
2.0	1.604	0.015	10.170	0.326	6.671	0.679
2.2	1.425	0.016	8.920	0.364	5.768	0.757
2.4	1.250	0.018	7.716	0.412	4.918	0.849
2.6	1.081	0.021	6.581	0.467	4.136	0.950
2.8	0.921	0.023	5.531	0.527	3.432	1.055
3.0	0.773	0.026	4.579	0.590	2.812	1.159
3.2	0.638	0.029	3.733	0.651	2.277	1.254
3.4	0.518	0.032	2.997	0.707	1.827	1.335
3.6	0.413	0.035	2.369	0.755	1.456	1.397
3.8	0.322	0.038	1.847	0.793	1.157	1.437
4.0	0.247	0.040	1.423	0.818	0.923	1.451
4.2	0.186	0.041	1.090	0.830	0.744	1.440
4.4	0.138	0.042	0.836	0.826	0.612	1.403
4.6	0.102	0.042	0.653	0.809	0.517	1.344
4.8	0.076	0.041	0.528	0.778	0.451	1.264
5.0	0.060	0.040	0.451	0.735	0.407	1.168
5.2	0.051	0.038	0.411	0.683	0.379	1.060
5.4	0.048	0.036	0.398	0.623	0.362	0.945
5.6	0.050	0.033	0.406	0.559	0.350	0.827
5.8	0.055	0.031	0.426	0.492	0.342	0.710
6.0	0.062	0.027	0.451	0.425	0.333	0.597

Table B.2: FOLD calculated $d\sigma/d\Omega$ for the first three $J^{\pi}=1^{+}$ excited states in the ^{24}Mg(t,^{3}He)^{24}Na reaction, using one body transition densities from OXBASH with the USDB interaction.

	Peak 5 E_x= 0. MeV $d\sigma/d\Omega$ [mb/sr]		Peak 6 E_x= 0.0 MeV $\sigma/d\Omega$ [mb/sr]	
Θ_{scat}	ΔL=0	ΔL=2	ΔL=0	ΔL=2
$[deg.]$	ΔS=0	ΔS=1	ΔS=0	ΔS=1
0.0	0.813	0.028	0.899	0.099
0.2	0.810	0.027	0.892	0.098
0.4	0.799	0.027	0.870	0.097
0.6	0.781	0.026	0.834	0.095
0.8	0.756	0.026	0.787	0.094
1.0	0.725	0.025	0.730	0.093
1.2	0.689	0.024	0.666	0.094
1.4	0.649	0.024	0.598	0.097
1.6	0.605	0.024	0.527	0.103
1.8	0.558	0.025	0.458	0.111
2.0	0.510	0.027	0.391	0.122
2.2	0.461	0.029	0.329	0.135
2.4	0.412	0.032	0.273	0.149
2.6	0.365	0.036	0.223	0.165
2.8	0.319	0.040	0.181	0.180
3.0	0.275	0.045	0.146	0.194
3.2	0.234	0.050	0.118	0.207
3.4	0.197	0.055	0.096	0.216
3.6	0.163	0.060	0.079	0.222
3.8	0.133	0.064	0.067	0.224
4.0	0.106	0.067	0.058	0.222
4.2	0.084	0.070	0.051	0.215
4.4	0.065	0.072	0.047	0.206
4.6	0.049	0.072	0.044	0.193
4.8	0.037	0.071	0.041	0.178
5.0	0.028	0.069	0.039	0.161
5.2	0.021	0.066	0.037	0.143
5.4	0.017	0.062	0.035	0.125
5.6	0.015	0.057	0.032	0.107
5.8	0.014	0.052	0.030	0.090
6.0	0.014	0.046	0.027	0.074

Table B.3: FOLD calculated $d\sigma/d\Omega$ for the first three $J^{\pi}=1^{+}$ excited states in the ^{24}Mg(t,^{3}He)^{24}Na reaction, using one body transition densities from OXBASH with the USDB interaction.

APPENDIX C

GLOSSARY OF TERMS AND ACRONYMS

C.1 Acronyms

A1900 Magnetic fragment mass separator at the NSCL, between the coupled cyclotrons and the S800 spectrometer.

CEX Charge EXchange, generally referring to isospin flips.

CRDC Cathode Readout Drift Chamber, position measurement device in the S800 focal plane.

DWBA Distored Wave Born Approximation.

EC Electron (e^-) capture.

FFN Fuller, Fowler and Newman papers, Refs. [36, 37, 38, 39], first establishing the importance of weak interactions on nuclei up to mass $A = 60$ in SNe.

FOLD Double folding.

FP Focal Plane of the S800.

K500 The first cyclotron of the Coupled Cyclotron Facility at the NSCL.

K1200 The second cuclotron of the Coupled Cyclotron Facility at the NSCL.

MDA Multipole Decomposition Analysis.

NSCL National Superconducting Cyclotron Laboratory.

OMP Optical Model Potetentials or Parameters.

OXBASH A package of codes for carrying out shell-model calculations[16].
For a given hamiltonian or interaction and model space, OXBASH
can calculate quantities such as single particle energyes, two body matrix
elements, β-decay branching ratios and radial wave functions.

PID Particle Identification.

S800 Spectrograph at the NSCL.

SN, SNe Supernova (plural, supernovae).

TOF Time of Flight.

C.2 Terms

A (Mass number, number of nucleons in a nucleus.

alpha, α ^{4}He nucleus, consisting of two protons and two neutrons.

Bρ magnetic rigidity, in units of T·m.

$\sigma\tau$ Spin-isospin operator.

τ Isospin, a quantum number related to the strong intereaction.

J$^\pi$ total angular momentum J and partity π,
or the *transfer* of such quantities in a reaction.

kHz kilo-Hertz, $10^3 Hz$.

Δ**L** Change in orbital angular momentum L.

mb millibarnes, 10^{-24}cm^2, standard unit of nuclear cross section.

MeV Mega electron-Voltz, 10^6 eV.

nucleon either proton or neutron in an atomic nucleus.

Q The total charge of a particle, or the nuclear charge Z minus the number of bound electrons. $Q = Z$ for fully ionized nuclei.

Q-value Amount of energy released in a reaction, $E_{reactants} - E_{products}$.

straggling the loss of kinetic energy in a medium through discrete steps.

T·m Tesla·meters, unit of magnetic rigidity Bρ.

triton (t) hydrogen nuclear isotope/atom with mass number $A = 3$, consisting of one proton and two neutrons.

Z Nuclear charge, or the number of protons in a nuclide.

C.3 Coordinates

$\mathbf{a}_{fp}$ angle in the dispersive direction at the focal of the S800 spectrometer.

$\mathbf{a}_{ta}$ angle in the dispersive direction at the target of the S800.

$\mathbf{b}_{fp}$ angle in the non-dispersive direction at the focal of the S800 spectrometer.

$\mathbf{b}_{ta}$ angle in the non- dispersive direction at the target of the S800.

δ_{ta} relative deviation in energy from E_0 the S800 spectrometer optics central ray energy, or $(E - E_0)/E_0$.

$\mathbf{x}_{fp}$ position in the dispersive direction at the focal of the S800 spectrometer.

$\mathbf{x}_{ta}$ position in the dispersive direction at the target of the S800.

$\mathbf{y}_{fp}$ position in the non-dispersive direction at the focal plane of the S800 spectrometer.

$\mathbf{y}_{ta}$ position in the non-dispersive direction at the target.

BIBLIOGRAPHY

[1] Evaluated Nuclear Structure Data File by the National Nuclear Data Center, Brookhaven National Laboratory, on behalf of the international Nuclear Structure Decay Data Evaluators Network; http://www.nndc.bnl.gov.

[2] F. Ajzenberg-Selove, R.E. Brown, E.R. Flynn, and J.W. Sunier. *Phys. Rev. C* **32** 756 (1985).

[3] K. Amos, A. Faessler, and V. Rodin. "Charge-exchange reaction cross sections and the Gamow-Teller strength for double β decay. *Physical Review C* **76** 014604 (2007).

[4] B. D. Anderson *et al., Phys. Rev. C* **43** 50 (1991).

[5] D. Bazin *et al.,* "Lise." *Nucl. Instr. Meth.* **A482** 307-327 (2002).

[6] D. Bazin *et al.,* "The s800 spectrograph." *Nucl. Instr. Meth.* **B204** 629 (2003). EMIS-14 conference proceedings.

[7] M. Berz, K. Joh, J. A. Nolen, B. M. Sherrill, and A. F. Zeller. *Phys. Rev. C* **47** 537 (1993).

[8] M. Berz and K. Makino. *COSY INFINITY Version 8.1 User's Guide and Reference Manual.* Department of Physics, Michigan State University, (2002). MSUHEP-20704.

[9] H.A. Bethe. "Nuclear physics needed for the theory of supernovae." *Annu. Rev. Nucl. Part. Sci.* **38** 1-29 (1988).

[10] H.A. Bethe, G.E. Brown, J. Applegate, and J.M. Lattimer. *Nucl. Phys. A* **324** 487 (1979).

[11] A.C. Betker *et al., Nucl. Instr. and Meth. A* **283**(1), 67-71 (1989).

[12] B.A. Brown and W.A. Richter. "A New Interaction for the *sd*-Shell?" *Journal of Physics: Conference Series* **20** 145 (2005), and private communication.

[13] B.A. Brown and W.A. Richter. "New USD Hamiltonians for the *sd*-shell." *Phys. Rev. C* **74** 034315 (2006), and private communication.

[14] B.A. Brown and B. H. Wildenthal. *Atomic Data Nuclear Data Tables* **33** 347 (1985).

[15] B. A. Brown and B. H. Wildenthal. *Annu. Rev. Nucl. Part. Sci.* **38** 29 (1988).

[16] B. A. Brown *et al.,* NSCL report MSUCL-1289.

[17] D.V. Bugg and C. Wilkin. "Polarisation in the (d,2p) reaction at intermediate energies." *Nucl. Phys.* **A467** 575-620 (1987).

[18] A. Burrows, L. Dessart, C. Ott, and E. Levine. "Multi-dimensional explorations in Supernova theory." *Physics Reports* **442** 23-37 (2007), and references therein.

[19] J.A. Caggiano. *Spectroscopy of Exotic Nuclei with the S800 Spectrograph.* PhD thesis, Michigan State University, (1999), and references therein.

[20] W.N. Catford. Catkin, v.2.01 ©the relativistic kinematics program. Technical report (2004).

[21] R.R.C. Clement. *A New Method for Nuclear Structure Measurement of Neutron Deficient Nuclei.* PhD thesis, Michigan State University (2003). And references therein.

[22] S. Cohen and D. Kurath. "Spectroscopic factors for the 1p-shell." *Nuclear Physics A* **101** 1-16 (1967).

[23] A. L. Cole *et al.,* "Measurement of the Gamow-Teller strength distribution in ^{58}Co via the ^{58}Ni(t,^{3}He) reaction at 115 MeV/nucleon." *Phys. Rev. C* **74** 034333 (2006).

[24] J. Cook and J.A. Carr. computer program FOLD, Florida State University (unpublished), based on F. Petrovich and D. Stanley, Nucl. Phys. **A275** 487 (1977), modified as described in J. Cook *et al.,* Phys. Rev. C **30** 1538 (1984) and R. G. T. Zegers, S. Fracasso and G. Colò (2006), unpublished (1988).

[25] I. Daito *et al.,* "(t,^{3}He) reaction; new tool for studying spin-isospin excitations in neutron rich nuclei." *Nucl. Instrum. Methods Phys. Res. A* **397** 465-471 (1997).

[26] I. Daito *et al.,* "Gamow-Teller strengths from (t,^{3}He) charge-exchange reactions on light nuclei." *Phys. Lett. B* **418** 27-33 (1998).

[27] D.N.F Dunbar, R.E. Pixley, W.A. Wenzel and W. Whaling. "The 7.68 MeV state in ^{12}C." *Physical Review* **92** 649 (1953).

[28] S. El-Kateb, K. P. Jackson, W. P. Alford, R. Abegg, R. E. Azuma, B. A. Brown, A. Celler, D. Frekers, O. Häusser, R. Helmer, R. S. Henderson, K. H. Hicks, R. Jeppesen, J. D. King, G. G. Shute, B. M. Spicer, A. Trudel, K. Raywood, M. Vetterli, and S. Yen. "Spin-isospin strength distributions for fp-shell nuclei: Results for the ^{55}Mn(n,p), ^{56}Fe(n,p), and ^{58}Ni(n,p) reactions at 198 MeV." *Phys. Rev. C* **49**(6), 3128-3136 (1994).

[29] J. Ellis, B.D. Fields, and D.N. Schramm. "Geological isotope anamolies as signatures of nearby Supernovae." *The Astrophysical Journal* **470** 1227-1236 (1996).

[30] W. Elsasser. *J. Phys. Radium* (1933).

[31] R. B. Firestone. *Nucl. Data. Sheets* **108** 2319 (2007), and references therein.

[32] E. R. Flynn and J.D. Garret. *Phys. Rev. C* **9** 210 (1974).

[33] E.R. Flynn, J.W. Sunier, and F. Ajzenberg-Selove. *Phys. Rev. C* **15** 879 (1977).

[34] M. A. Franey and W. G. Love. *Phys. Rev. C* **31** 488 (1985).

[35] D. Frekers. "Facets of $(d,^2\mathrm{He})$ charge-exchange reactions at intermediate energies." *Nucl. Phys.* **A731** 76-93 (2004), and references therein.

[36] G. M. Fuller, W. A. Fowler, and M. J. Newman. "Steller weak-interaction rates for *sd*-shell nuclei. I. Nuclear matrix element systematics with application to ^{26}Al and selected nuclei of importance to the supernova problem." *Astrophys. J. Supp. Series* **42** 447 (1980).

[37] G. M. Fuller, W. A. Fowler, and M. J. Newman. "Steller weak-interaction rates for intermediate-mass nuclei. II. $A = 21$ to $A = 60$." *Astrophys. J.* **252** 715 (1982).

[38] G. M. Fuller, W. A. Fowler, and M. J. Newman. "Steller weak-interaction rates for intermediate mass nuclei. III. Rate tables for the free nucleons and nuclei with $A = 21$ to $A = 60$." *Astrophys. J. Supp. Series* **48**279 (1982).

[39] G. M. Fuller, W. A. Fowler, and M. J. Newman. "Steller weak-interaction rates for intermediate-mass nuclei. IV. Interpolation procedures for rapidly varying lepton capture rates using effective log (ft)-values." *Astrophys. J.* **293** 1 (1985).

[40] N.K. Glendenning. *Direct Nuclear Reactions.* Academic Press, Inc., New York, (1983).

[41] Maria Göppert Mayer. "The shell model." *Science* **145**(4), 999-1006 (1964).

[42] E.-W. Grew and C. Baumer. "Studies on the double-β decay nucleus ^{64}Zn using the $(d,^2\mathrm{He})$ reaction." **77** 064303 (2008).

[43] E. W. Grewe *et al.,* "Gamow-Teller transitions to ^{32}P studied through the ^{32}S(d,^{2}He) reaction at E_d=170 MeV." *Phys. Rev. C* **69** 064325 (2004).

[44] M. Hagemann *et al.,* "High-resolution determination of gt strength distributions relevant to the presupernova evolution using the (d,^{2}He) reaction." *Phys. Lett.* **B579** 251 (2004).

[45] M. N. Harakeh and A. van der Woude. *Giant Resonances: Fundamental High-Frequency Modes of Nuclear Excitations.* Oxford University Press, New York (2001).

[46] A. Heger, K. Langanke, G. Martínez-Pinedo, and S. E. Woosley. *Phys. Rev. Lett.* **86** 1678 (2001).

[47] A. Heger, S. E. Woosley, G. Martínez-Pinedo, and K. Langanke. "Presupernova Evolution with Improved Rates for Weak Interactions." *ApJ* **560** 307-325 (2001).

[48] A. Heger, S. E. Woosley, G. Martínez-Pinedo, and K. Langanke. "Presupernova evolution with improved rates for weak interactions." *Astro Phys. J.* **560** 307 (2001).

[49] G.W. Hitt. Private communication.

[50] G.W. Hitt *et al.,* "Development of a secondary triton beam from a primary ^{16,18}O beams for (t,^{3}He) experiments at intermediate energies." *NIMA* **566**(2), 264-269 (2006).

[51] W. R. Hix, O. E. Messer, A. Mezzacappa, M. Liebendörfer, J. Sampaio, K. Langanke, D. J. Dean, and G. Martínez-Pinedo. "Consequences of Nuclear Electron Capture in Core Collapse Supernovae" *Physical Review Letters* **91**(20), 201102 (2003).

[52] W. R. Hix, O. E. B. Messer, A. Mezzacappa, J. Sampaio, K. Langanke, G. Martínez-Pinedo, M. Liebendörfer, and D. J. Dean. "Nuclear electron capture in core collapse Supernovae" *Nuclear Physics A* **758** 31-34 (2005).

[53] M.E. Howard. "Instructions for creating S800 inverse maps." For more information, email Meredith Howard at howard@nscl.msu.edu.

[54] K. Iwamoto, F. Brachwitz, K. Nomoto, N. Kishimoto, H. Umeda, W. R. Hix, and F. K. Thielemann. "Nucleosynthesis in Chandrasekhar mass models for type Ia Supernovae and constraints on progenitor systems and burning-front propagation." *The Astrophysical Journal Supplement Series* **125** 439-462 (1999).

[55] K. P. Jackson *et al.,* "The (n,p) reaction as a probe of Gamow-Teller strength." *Phys. Lett.* **B201** 25 (1988).

[56] J. Kamiya *et al., Phys. Rev. C* **67** 064612 (2003).

[57] K. Langanke. "Weak-interaction processes in stars" *Nuclear Physics A* **718** 92-100, (2003).

[58] W. G. Love and M. A. Franey. *Phys. Rev. C* **24** 1073 (1981).

[59] G. Martínez-Pinedo A. Heger, S.E. Woosley and K. Langanke. "Presupernova evolution with improved rates for weak interactions. *ApJ* **560** 307-325 (2001).

[60] D. J. Morrissey, B. M. Sherrill, M. Steiner, A. Stolz, and I. Wiedenhoever. "Commissioning the A1900 projectile fragment separator." *Nucl. Instr. Methods Phys. Res. B* **204** 90-96 (2003).

[61] R. Munroe. xkcd. http://www.xkcd.com/, with permission under a Creative Commons Attribution-NonCommercial 2.5 License. So I can't sell this shit.

[62] T. Nuzeki *et al.,* "Spin-isospin excitation in *sd*-shell nuclei by the (d,^{2}He) reaction at E_d= 270 MeV." *Nuclear Physics* **A577** 37c-42c (1994).

[63] H. Okamura. "Three-body treatment of the (d,^{2}He) reaction on the basis of the adiabatic approximation." *Phys. Rev. C* **60** 064602 (1999).

[64] H. Okamura *et al.,* "Tensor analyzing power of the (d,^{2}He) reaction at 270 MeV." *Phys. Lett.* **B345** 1-5 (1995).

[65] F. Osterfeld. *Rev. Mod. Phys.* **64** 491 (1992).

[66] S. C. Pieper and R. B. Wiringa. *Annu. Rev. Nucl. Part. Sci.* **51** 53 (2001), and R.B. Wiringa, private communication (2005).

[67] G.M. Raisbeck, F. Yiou, D. Bourles, C. Lorius, J. Jouzel, and N.I. Barkov. "Evidence for two intervals of enhanced ^{10}Be deposition in antarctic ice during the last glacial period." *Nature* **326** 273-277 (1987).

[68] S. Rakers *et al.,* "Gamow-Teller matrix elements from the ^{12}C(d,^{2}He) and ^{24}Mg(d,^{2}He) reactions at 170 MeV." *Physical Review C* **65** 044232 (2002).

[69] S. Rakers *et al., Nucl. Instrum. Methods Phys. Res. A* **481** 253 (2002).

[70] J. Rapaport and E. Sugarbaker. "Isovector excitations in nuclei." *Annu. Rev. Nucl. Part. Sci.* **44** 109 (1994).

[71] D.A. Resler, M.B. Aufderheid, S.D. Bloom and G.J. Mathews. "Implications of the recent ^{59}Co$(n,p)^{59}$Fe experiment for stellar electronc capture rates. *Physical Review C* **47** 2961-2969 (1993).

[72] D.A. Resler, M.B. Aufderheid, S.D. Bloom and G.J. Mathews. "Shell-model calculations of Gamow-Teller strength in ^{51}V, ^{54}Fe, and ^{59}Co. *Physical Review C* **48** 1677-1685 (1993).

[73] R. Ronningen. Private communication.

[74] G.R. Satchler. *Direct Nuclear Reactions.* Oxford University Press, New York (1983).

[75] T. Schwab, H. Wollnik, H. Geissel, G. Münzenberg, C. Scheidenberger and N. Iwasa. "MOCADI, a universal Monte Carlo code for the transport of heavy ions through matter within ion-optical systems." *Nuclear Instruments and Methods in Physics Research B*, **126** 284-289 (1996).

[76] K. Summerer and B. Blank, B. "Modified emperical parameterization of fragmentation cross sections." *PRC* **61** 034607 (2000).

[77] K. Summerer *et al.,* "Target fragmentation of Au and Th by 2.6 GeV protons." *PRC* **42** 2546 (1999).

[78] T. D. Taddeucci, C. A. Goulding, T. A. Carey, R. C. Byrd, C. D. Goodman, C. Gaarde, J. Larsen, D. Horen, J. Rapaport, and E. Sugarbaker. "The (p, n) reaction as a probe of beta decay strength." *Nucl. Phys.* **A469** 125-172 (1987).

[79] O. Tarasov and D. Bazin. "Lise." *Nuclear Physics A* **746** 411 (2004).

[80] F.-K. Thielemann, D. Argast, F. Brachwitz, W. R. Hix, P. Höflich, M. Liebendörfer, G. Martinez-Pinedo, A. Mezzacappa, I. Panov, and T. Rauscher. "Nuclear cross sections, nuclear structure and stellar nucleosynthesis" *Nuclear Physics A* **718** 139-146 (2003).

[81] R. G. Thomas. *Phys. Rev.* **88** 1109 (1952); J.B. Erhman, Phys. Rev. **81** 412 (1951).

[82] S. Y. van der Werf, S. Brandenburg, P. Grasdijk, W. A. Sterrenburg, M. N. Harakeh, M. B. Greenfield, B. A. Brown, and M. Fujiwara. "The effective ^{3}He-nucleon force in a microscopic DWBA approach to the (^{3}He,t) charge-exchange reaction." *Nucl. Phys. A* **496** 305-332 (1989).

[83] B. H. Wildenthal. *Prog. Part. Nucl. Phys.* **11** 5 (1984).

[84] B. H. Wildenthal, M. S. Curtin, and B. A. Brown. *Phys. Rev. C* **28** 1343 (1983).

[85] S.E. Woosley and T. Janka. "The physics of core-collapse Supernovae." *Nature Physics* **1**(3), 147 (2005).

[86] H. M. Xu, C. A. Gagliardi, G. K. Ajupova, B. Kokenge, and Y. W. Lui. "Gamow-Teller strength of ^{26}Mg." *Phys. Rev. C* **54** 3266 (1996).

[87] T. Yamagata *et al.,* "Elastic scattering of ^{3}He particles at 450 MeV." *Nucl. Phys. A* **589** 425-434 (1995), and T. Yamagata and H. Akimune, private communication.

[88] W.-M. Yao *et al.,* "Review of Particle Physics". *Journal of Physics G* **33** 1 (2006). See section *2*7. Passage of particles through matter, and references therein.

[89] J. Yurkon *et al.,* "Focal plane detector for the S800 high-resolution spectrometer." *Nucl. Instr. Meth.* **A422** 291 (1999).

[90] R.G.T. Zegers. Private communication.

[91] R.G.T. Zegers *et al.,* arXiv:0803.3856 (2008) and accepted to be published in Phys. Rev. C.

[92] R. G. T. Zegers *et al.,* "The (t,^{3}He) and (^{3}He,t) reactions as probes of Gamow-Teller strength." *Phys. Rev. C* **74** 024309 (2006).

[93] R. G. T. Zegers *et al.,* "Extraction of weak transition strenths via the (^{3}He,t) reaction at 420 MeV." *Phys. Rev. Lett.* **99** 202501 (2007).